Otto-von-Guericke-University Magdeburg
Faculty of Electrical Engineering and Information Technology
Institute for Medical Engineering

Master of Science

A Novel Training System for Tracked Ultrasound Catheters Used in Interventional Cardiology

Author:
Kristjan Qarri

Date:
November 12, 2020

First examiner:
Prof. Dr. -Ing. Bernhard Preim

Second examiner:
Jun. Prof. Dr. Sandy Engelhardt

Third examiner:
M.Sc. Robert Kreher

Abstract

Purpose: Minimally invasive interventions are becoming a predominant procedure in operating room (OR). Cardiac catheterization is a common minimally invasive procedure. To reduce the complications and to increase performance a good spatial orientation of the surgeon and precise location of catheter is required. Intracardiac echocardiography recently has gained good use in heart catheterization. A simple training system is designed combining EM tracking and ICE technology.

Theory and Methods: Two 5-degree of freedom (DOF) sensors were attached to an ICE catheter. The sensors are calibrated temporally and spatially using freehand tracked ultrasound calibration application (fCal), part of public software library for ultrasound (PLUS). Spatial calibration maps the real-time position and orientation of the transducer to the real-time position and orientation of the US images. Additionally, a heart model is registered using fCal. The 3D-printed heart model is encased into a box and a 6-DOF sensor is rigidly fixed relative to the heart model. Thus, the US image can be visualised on real-time within the volume of the 3D-printed heart model. The location of the visualized echo image within the heart computer model will be realistic to the location of the ICE transducer within the 3D-printed heart model. The accuracy of the tracking system and tracked ultrasound images was evaluated. Additionally, 3D spatial compounding capability of the system using various ultrasound transducers was tested.

Results: Implementation of electromagnetic tracking for intracardiac echocardiography probes showed good registration accuracy, reported from fCal. The influence of ICE and TEE probes proved to be not significant on the tracking accuracy. This creates ambiguity with the poor results from the three dimensional volume reconstruction of the tracked ultrasound images. Electromagnetically tracked ICE catheter could be used to provide a visual feedback about the position and orientation of the ultrasound image.

Conclusion: The implementation electromagnetic tracking for ICE catheters was successful. A visual feedback about the ultrasound image was generated, which corresponded to the movement of the catheter. More extensive qualitative assessment about the accuracy of the position and orientation of the visualized ultrasound image is neccesary.

Task of the Thesis in the Original:

Declaration by the candidate

I hereby declare that this thesis is my own work and effort and that it has not been submitted anywhere for any award. Where other sources of information have been used, they have been marked.

The work has not been presented in the same or a similar form to any other testing authority and has not been made public.

Magdeburg, January 8, 2021

Contents

List of Acronyms

3D 3-dimensional

ac alternating current

A-mode amplitude mode

B-mode brightness mode

BT brachytherapy

CNR contrast-to-noise-ratio

CSV comma separated values

CT computed tomography

dc direct current

D-mode doppler mode

DOF degree of freedom

EM electromagnetic

EMT electromagnetic tracking

EMTS electromagnetic tracking system

EP electrophysiology

F french gauge

fCal freehand tracked ultrasound calibration application

FG field generator

FOV field of view

GPS global positioning system

HD high definition

ICE intracardiac echocardiography

ICTS interventional cardiology training system

IGS image guided surgeries

IGT image guided therapies

ISO international organization for standardization

IVUS intravascular ultrasound

M.D. doctor of medicine

MedTech medical technology

MHA file format

MHz megahertz

M-mode motion mode

MR magnetic resonance

MRI magnetic resonance imaging

MV mitral valve

NRRD nearly raw raster data

OpenIGTLink open network interface for image-Guided therapy

OR operating room

PET positron emission tomography

PLUS public software library for ultrasound

PortUsImageOrientation PLUS configuration file: The orientation of the image outputted by the device

RCS reference coordinate system

ROI region of interest

SHD structural heart disease

SM spatial mapping

SNR signal-to-noise-ratio

SONAR sound navigation and ranging

tech technology

TEE transesophageal echocardiography

TTE transthoracic echocardiography

US ultrasound

VideoDevice PLUS configuration file: An independent data acquisition or processing element. Each device has its own processing thread that runs in parallel with other devices and responsible for reading data from its inputs and providing data on its outputs.

VM virtual model

FLE fiducial localization error

FRE fiducial registration error

TRE target registration error

3DRA three-dimensional rotational angiography

1. Introduction

1.1. Motivation

Ultrasound imaging is a non-invasive, inexpensive, and radiation-free imaging modality that provides an excellent temporal resolution. It is the most widely used exam in the radiology. Interventional cardiology deals with issues in blood vessels and the heart. The procedures are non-surgical and make use of catheters to perform interventions. During the interventions the catheters are guided using fluoroscopy, transesophageal echocardiography (TEE), or intracardiac echocardiography (ICE). Fluoroscopy is the gold standard for catheter guidance while advancing towards the heart [1]; however, it does not provide sufficient anatomical information when it comes to the heart. A hybrid intervention consisting of fluoroscopy and ultrasound is applied for better navigation. Transesophageal echocardiography is often the choice as the second imaging modality, in addition to fluoroscopy.

Intracardiac echocardiography catheters are miniaturized ultrasound (US) probes integrated in the tip of the catheters, which enables to depict the anatomy of the heart. Intracardiac echocardiography is mainly used for instrument guidance during heart interventions [2]. Application of ICE could omit the necessity of using fluoroscopy and the cardiologist can maneuver the intracardiac echocardiography catheter during the procedure [2]. In order to use intracardiac echocardiography catheters properly, it is neccesary to have prior training. Spatial orientation of the interventionist is key factor to an efficient procedure. It happens often that the physician losses the sense of orientation, therefore he needs some time to regain the sense of the correct position and orientation of the tip of the catheter (probe).

Minimally invasive procedures, despite being advantageous compared to open surgeries for several reasons: such as quick recovery of the patient, less scarring, shorter hospitalization etc; they are complex and present novel challenges. The growing interest and application of minimally invasive interventions has created the demand for training systems. Conventional hands-on training methods involve practising on animals and cadavers, or training systems which employ thorax phantoms and real medical devices. Both methods have disadvantages, the former suffers ethical problems, whereas the latter from X-ray exposure and expensive devices for the setup. Computer based interventional cardiology training systems is an other growing field, which aims to address the problems of conventional training systems. They stimulate the devices, physic models of ICE catheters, blood hemodynamics, and organ animated models [3]. Both above-mentioned approaches suffer either from ethical issues or technical and health related burdens.

This thesis proposes an approach for a simple training system, which enables hands-on experience with manoeuvring ICE catheters on a 3D-printed heart model and visual feedback about the position and the orientation of the generated sonogram within the volume of the heart model.

1.2. Contribution

To address the issues mentioned above a simple setup is designed, with the aim to provide a visual aid for the position and orientation of the catheter tip and the ultrasound image during intracardiac interventions. For this purpose, a new approach of tracking ICE catheters is proposed, using EM tracking to obtain the position and orientation information of the probe. The aim of this work is to answer the fundamental research question related to electromagnetic tracking in medicine, in general, and combining EM tracking with US imaging as a tool to implement in an interventional cardiology training system specifically. The objectives to achieve are as below:

- Configure a system capable of tracking tools with attached markers electromagnetically.
- Adapt the tracking system for echocardiography probes.
- Register a 3D-printed heart model to a reference sensor as a necessary step towards a training system for intracardiac echocardiography interventions.
- Provide quantitative and qualitative assessment of the work.

The work around the first objective is presented in Sec. 4.1.3. The procedure involves attaching electromagnetic sensors to the objects we want to track (stylus, phantom, probe) and setting up the NDI's Aurora V2 tracking system. The tracking data is gathered from the electromagnetic tracking system. Due to inaccessibility of the raw image data from the ultrasound machine, image data were collected from the ultrasound machine screen via a frame grabber and the unnecessary content of the image was removed. Ultimately, the image data and tracking data are transmitted to PLUS toolkit for processing, visualization and storing.

Second objective is addressed in Sec. 4.2. Here is presented a method of tracking a 90 cm, 8-french gauge, phased array ICE steerable catheter (Acuson AcuNav ultrasound catheter, Siemens Medical Solutions, Mountain View, CA, USA) using NDI Aurora tracking system. Two 5-degree of freedom magnetic sensors (Aurora 5DOF Sensor, 0.5 x 8 mm) are rigidly attached at the tip of the catheter. The objective is to analyse the electromagnetic tracking feasibility of intracardiac echocardiography catheters for the purpose of building a simple training system for interventional cardiologists.

Third objective aims to make applicable objective 1. and objective 2. After having set up the tracking system, it is straightforward to register the heart model to the reference sensor and visualize the catheter while manoeuvring inside the heart.

Last objective is addressed in the Results and Discussion sections.

1.3. Structure of the thesis

This thesis work is organized according to the following structure:

- *Introduction* describes the motivation behind this thesis, the reasons why the research in this area is necessary, and what are the main objectives to achieve from this thesis.
- *Background* provides the fundamental knowledge about medical ultrasound, including intracardiac echocardiography, electromagnetic tracking, and the mathematical foundations to make the information in this thesis easier to grasp for audience.
- *State of the Art* chapter covers the related research to the field. It serves as research foundation for the proceeding of the work. It covers similar work to what it is presented, in terms of research articles and patents.
- *Methods* describes the process of configuring the electromagnetic tracking system, methods used, and the proposed implementation for the already configured system.
- *Experiments* describe in details the materials and procedure of the conducted experiments. They are prescribed as "Experiment 1", "Experiment 2", "Experiment 3", "Experiment 4", and "Experiment 5" in the table of contents, but in the document is shown only the title of the experiment.
- *Results* chapter constitutes the data visualization acquired from the calibration process of the tracking system and the experiments. The images will present mainly box plots and line graphs for evaluation of the data and comparison between data sets.
- *Discussion* about the results of this work will take place in Ch. 7. Most important results will be discussed separately and compared to similar existing literature.
- *Conclusion and Future Work* chapter will conclude this thesis report. It wraps up the discussed results and includes recommendations based on the findings of this work.

2. Background

Sound waves that exceed the frequency limit of audible range, roughly between 20 Hz and 20 kHz, are considered high frequency waves [4]. The term used to describe these waves is *ultrasound*. Ultrasound imaging is a widely used imaging modality, especially for Sonography of the abdomen and the heart. Its characteristics as being least harmful among other imaging modalities, low-cost, real-time, and fairly easy to access make US an advantageous approach for medical interventions guidance [5]. Over the recent years, tremendous research have been oriented towards Medical technology covering also medical imaging modalities, such as computed tomography (CT), magnetic resonance imaging (MRI), positron emission tomography (PET) and US. According to *GTAI (Germany trade & Invest)* [6] [7], Germany leads as the largest Europe's market for medical technology and third in global scale. This being said, the investment on medical technology (MedTech), particularly on research and development, is the highest in Europe. The information relating to US technology is mainly taken form *Szabo et al.* [8] and *Hoskins et al.* [9, 10].

2.1. Medical Ultrasound History

Lazzaro Spallanzani (1729 - 1799), an Italian priest and physiologist, was the first to observe bats for their capacity to navigate using acoustic waves. He observed that they could avoid objects and find their prey in absence of light, thus proving that bats could move around using echolocation [11]. This marked the foundations of US and its potential. Nevertheless, until the discovery of *piezoelectric* effect, from Pierre and Jacques Curie in 1880, not much was done in this direction. The sinking of *Titanic* and *World War 1* brought into use this technology once again. Paul Langevin and Constantin Chilowsky were the first to use this technology to locate a sank submarine, according to *Kane et al.* and *Van Tiggelen et al.* [4, 12]. Again, after the *World War 1* was over, the research for this technology was put on hold. *World War 2* once again emphasized the interest on the application of the piezoelectric effect for echolocation [12]. Sound navigation and ranging (sound navigation and ranging (SONAR)) was the first apparatus built for echolocation. The purpose was for ships to detect icebergs from a meaningful distance in order to avoid accidents like *Titanic* [4]. Having the SONAR technology provided, attempts were made to adapt it in medical applications. Karl Dussik (neurologist) was

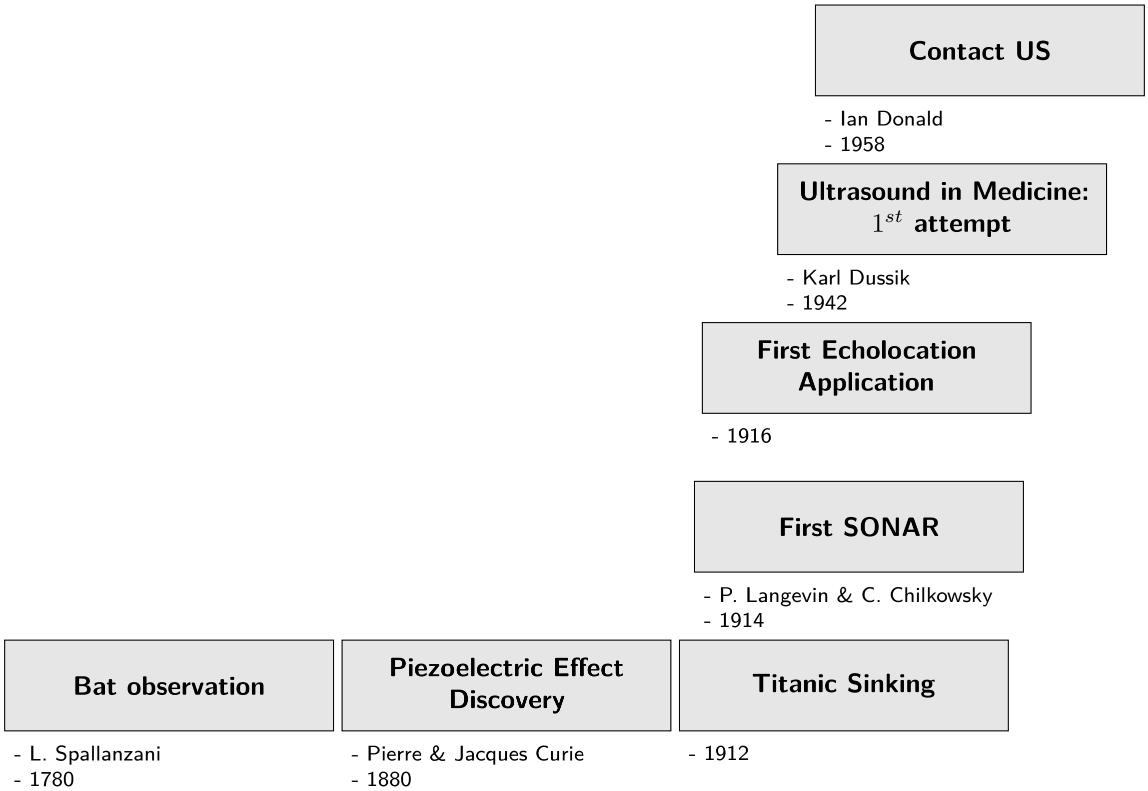

Figure 2.1.: Story-line of Ultrasound: A distribution of main events throughout the years

the first to mark medical application of US. According to *Van Tiggelen et al.* and *Kane et al.* [4, 12] Dussik attempt was made in 1942, and according to *Wagai*† [13] in 1949. Simultaneously but not synchronised with each other researchers around the word were working around applications of Ultrasound in medicine: Karl Dussik (Austria), John Julian Wild (United States of America), Ian Donald (United Kingdom) and Toshio Wagai (Japan). Donald (gynecologist) brought the application one step further when introducing contact ultrasound in 1958. Until then, US scanning was done by aquatic submergence. Donald used the viscous gel, which still continuous to be used [12]. Fig. 2.1 depicts main events happening throughout almost two centuries which brought us to modern diagnostic medical ultrasound.

2.2. Medical Ultrasound Fundamentals

When an acoustic wave carries energy above human hearing spectrum, in physics it is categorised as "ultrasound" acoustic wave. Diagnostic ultrasound scanners apply frequencies in the range of 2 to 18 megahertz (MHz) [14]. The principle of diagnostic sonographic imaging is echolocation. Mainly based on the distance measured for each echo received, a cross-sectional image is constructed. An US imaging system constitutes acoustic properties and signal processing. In this section the focus will be more into the processes happening rather than imaging system itself.

The signal processes can be analysed in time domain or frequency domain. Both forms can be alternated depending on the nature of information we seek to find. Using *Fourier Transform* signals in the time domain can be expressed as sum of elementary sines and cosines in the frequency domain. Given the fundamental frequency (f_0) and its harmonics for a certain signal, the processing and filtering becomes easier [8]. *Fourier* transform formula is shown in Eq. (2.1). This transform exploits the relation of the time-span of the signal with its frequency spectrum. As *Szabo* explains, *"A short time pulse has a wide extent in frequency, or a broad bandwidth. Similarly, a long pulse, such as a tone burst of n cycles, has a narrow band spectrum"* [8, p. 41]. Fig. 2.2 depicts the *Fourier* transformation of the *Gaussian pulse*. In the fig. 2.2a the pulse is represented on its time waveform and in the fig.2.2b as the complex spectrum in the frequency domain. As mentioned before, both forms are equivalent and describe the same signal.

$$H(f) = \mathscr{F}_{-i}[h(t)] = \int_{-\infty}^{\infty} h(t)e^{-i2\pi ft}dx \tag{2.1}$$

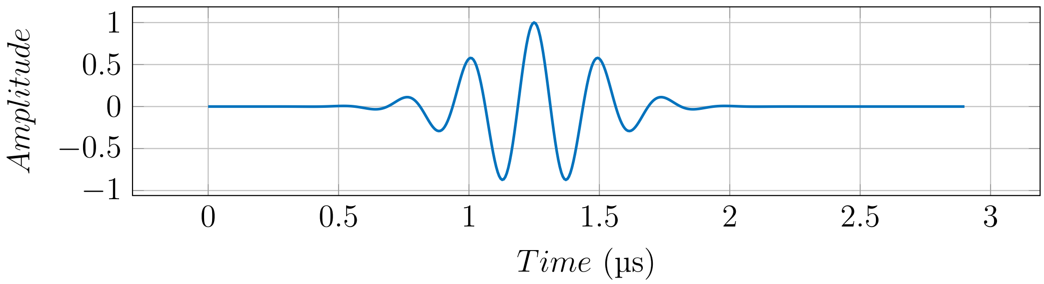

(a) Time domain, 5 MHz pulse

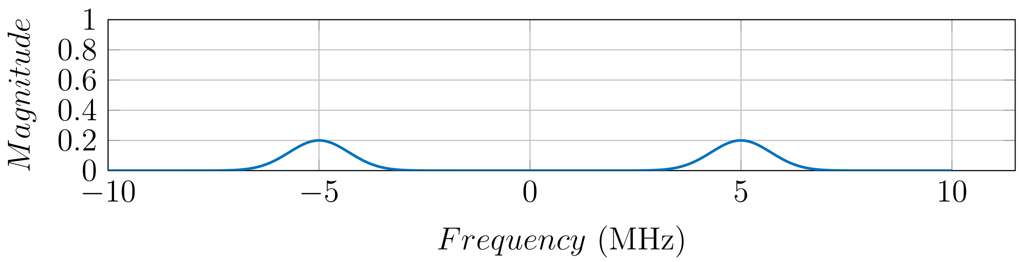

(b) Frequency domain, magnitude and phase

Figure 2.2.: Gaussian 5 MHz pulse in time domain and frequency domain [8]

Fourier transform is especially important to distinguish echo signals from one another. Different interface layers of the body anatomy will echo-back in certain time intervals. Therefore, knowing the extend of the signal in the time domain gives information about the position of the origin of the echo signal within the body cross-section [9]. In the end of the day a map of the locations of echos is build. Ultimately, mapping the brightness of the image to the magnitude of the amplitude of the echos produces an image with dark and bright regions. This technique is known as brightness mode (B-mode), see 2.2.3) [15].

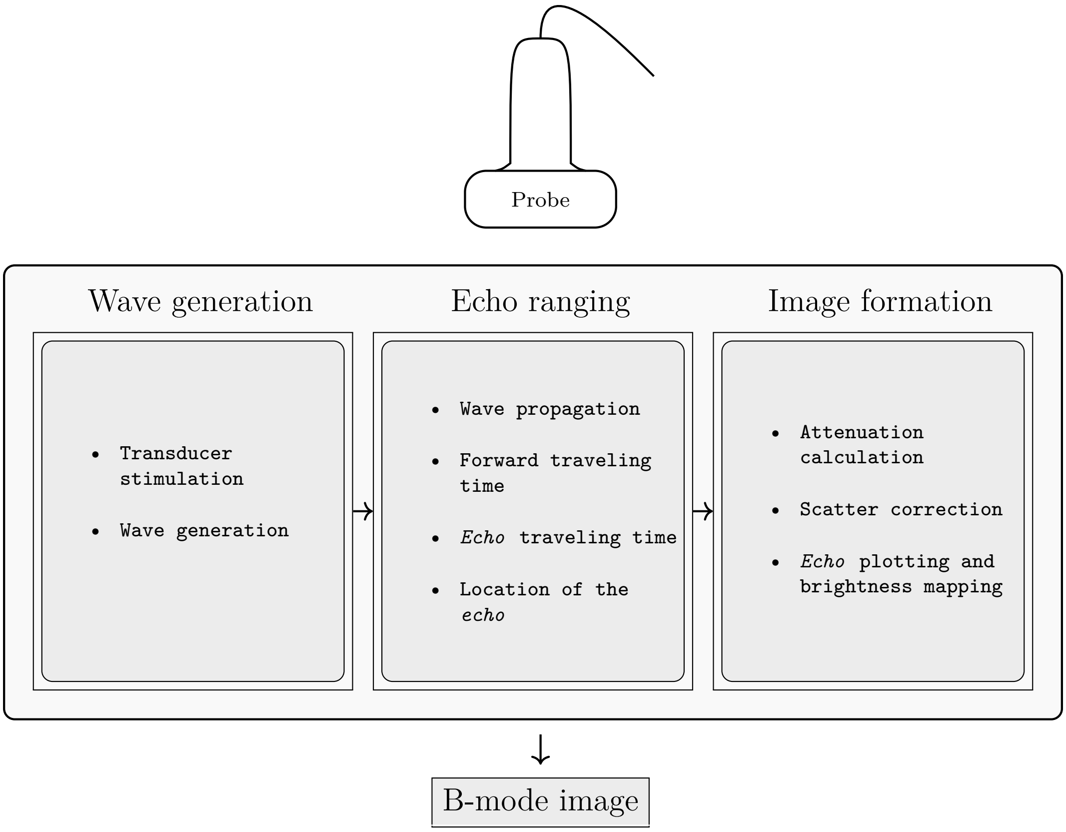

Figure 2.3.: The process of building a B-mode ultrasound image

There are three main ultrasound imaging techniques, in addition to B-mode:

- amplitude mode (A-mode): First and simplest mode of ultrasound. It involves a single transducer. The echos are plotted on a screen as a function of depth. It is used in therapeutic ultrasound [14].
- brightness mode (B-mode): Unlike A-mode, B-mode involves multiple transducers stimulated with pulse signals, scanning simultaneously a cross-section plane of the body . The echo signals are represented in different shades of gray, thus forming a two-dimensional image on the screen. B-mode is the most widely used mode and remains the primary scanning modality in clinical medical imaging.
- motion mode (M-mode): It consists on stacking a sequence of B-mode images and sort them in fourth dimension (time). It is useful to distinguish tissue boundaries and check the range of motion for moving organs.
- doppler mode (D-mode): It is mainly used for visualising blood flow. It has extensive application in medical diagnostic imaging. Can be applied to analyse perfusion of body parts or certain structural heart disease (SHD).

Regardless the mode used, the process of building the image facilitates the same devices and technology. As depicted in Fig. 2.3, to form an image a few steps are required. The B-mode image is the result of many processes (B-mode will be used as a reference as it is the most used in medical diagnosis). The steps are performed as it follows:

1. The examiner sweeps the ultrasound probe on the surface of the skin/ organ.
2. The transducer is stimulated with electric pulses sent from the machine, according to the frequency required.
3. An ultrasound wave is generated and propagates through the medium.
4. As the wave propagates parts of it attenuate (lost as heat), parts of it are scattered and parts of it are reflected on the boundaries of the organs as echo.
5. After the echo is received from the transducer, the algorithm calculates the origin of the echo considering the *travel* time.
6. B-mode image is constructed by mapping the magnitude of the amplitude of each echo to a brightness level (grey scale), within the field of view (FOV).

All steps are completed in a fraction of second, excluding step one. The process can be broken down into electrical signals related and acoustic/electroacoustic related events. Fig. 2.3 elaborates these events in a schematic fashion.

2.2.1. Wave generation

It is not in the scope of this work to provide extensive information related to waves and transducers, however some basics will be presented. The basic and most important element of an ultrasound probe is the transducer and the main component the piezoelectric plate. The transducer is made up of an array of elements. The shape of the array varies: linear array, trapezoidal array, curvilinear array, sector and radial array. Each type of array provides specific FOV and imaging *depth*. A simple sketch of a transducer element within an array is depicted in Fig. 2.4. Element number four in the Fig. 2.4, the piezoelectric plate, is the component where the wave originates from and echos are detected. The plate is a dielectric material sandwiched between two electrodes. A difference of electrical potential is applied between two electrodes. Due to acoustic properties of the piezoelectric material, the plate will either expand or contract (expand for positive voltage, contract for negative voltage). During this process ultrasonic waves are produced. Conversely, when the plate is exposed to an ultrasonic wave it will produce a difference in potential between two electrodes, consequently electric current. Afterwards, the location where each echo is generated is computed and the information will be used later on to build the B-mode image (explained in paragraph 2.2.3).

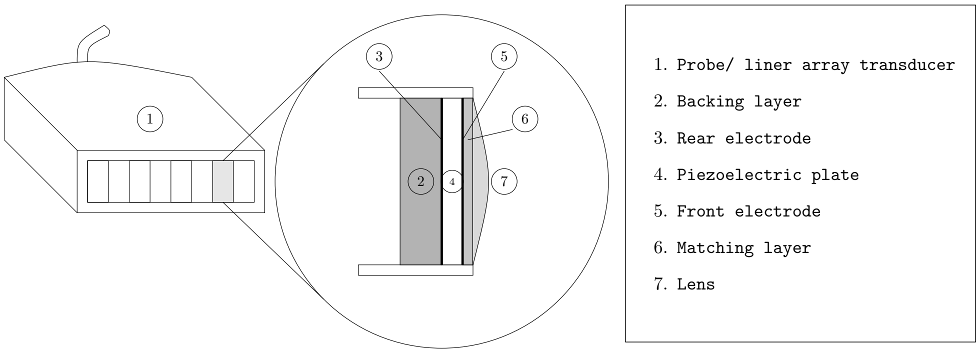

(a) (b)

Figure 2.4.: Basic components of a transducer [10]

2.2.2. Echo ranging

Mechanical waves have the tendency to refract, diffract, and reflect, when propagating through a medium. Typically, mechanical waves reflect when a sudden change in the density of the matter occurs. This is the property exploited in medical ultrasound imaging. As mentioned in paragraph 2.1, the property of US was first used for the location of submarines. The concept of location lies on measuring the time that the wave needs to travel back and forth, thus finding the site of reflection. Similarly, the range of the target from the transducer is calculated. An echo location method used on ships for measuring the depth of the water is depicted in Fig. 2.5. The ultrasound transducer emits a pulse of US wave. The wave travels through the water and it is reflected when it reaches the seabed. The reflected wave (echo) travels back to the origin (transducer). The goal of this echo-range principle is to find the origin of the echo.

In order to find the origin, the back and forth traveling time should be calculated. If the depth of the water is denoted with d, speed of sound in water with c (1540 ms^{-1} for human tissue) and the forward traveling time with t, based on the equation of the kinematics $t = d/c$, the wave will travel the same distance to reach the transducer, i.e. d.

Finally, the time required for the wave to travel back and forth could be calculated as: $t = 2d/c$. Since the distance is the variable of interest, the equation would give $d = ct/2$. Imagine this process repeated for a burst of ultrasound pulses. The transducer will change form sending (a pulse) to listening (for an echo) several times per second. After all echos are received for every single pulse sent the next transducer element repeats the same process, until the whole body cross-section is scanned. This echo ranging principle is applied in the same fashion in medical ultrasound. Multiple echo locations are used to form B-mode image, as explained in paragraph 2.2.3.

Figure 2.5.: Measuring the depth of the water using echo ranging. From *Hoskins et al.* [9, p. 2].

2.2.3. B-mode image formation

The B-mode image described below will refer to a liner transducer array. Typically, a linear transducer array consists of 128 transducer elements (Fig. 2.4). Depending on the application, some transducer configurations might have as much as 256 elements, according to *Hoskins et al.* [10]. Each element is responsible for emitting and receiving a sequence of pulses/ echos. Each pulse lasts about 2 µs [16]. After all echos are successfully received, a line is formed in the image, say line zero (0), as depicted in Fig. 2.6. The nearby transducer element is exited to form line one (1). The process is concluded with the last transducer successfully receiving the echo sequence, thus building the last line in the image (Fig. 2.6c). Knowing that the arrival time of the echo is proportionally related to the depth, the brightness of the image along each line is mapped to the magnitude of the amplitude of the echo at the origin, see Fig. 2.7b. A complete sweep of the beam across the transducer array takes 1/30 of a second, thus the ultrasound machine provides a frame rate of approximately 30fps.

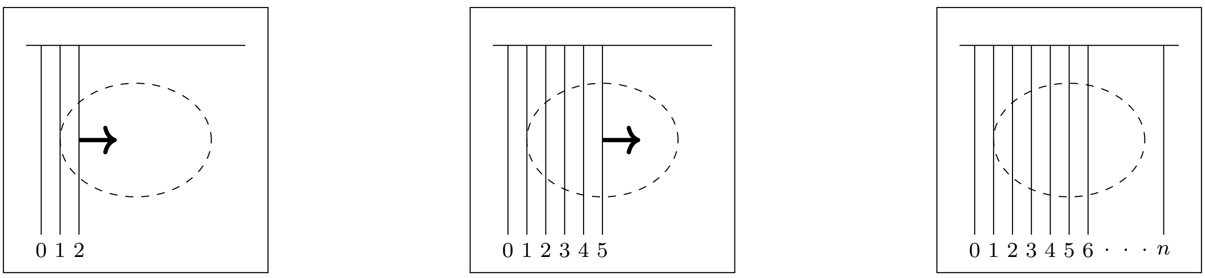

(b) **(c)**

Figure 2.6.: Image formation of B-mode image. Line-by-line scan, from [10]

2.3. Echocardiography

Echocardiography is the application ultrasound for the purpose of taking US images of the heart. The position of the heart within the rib cage makes it challenging. This dictates a sector shape of the scanning beam, allowing heart screening form the spaces between the ribs. There are four known transthoracic cardiac examination windows for an TTE exam [17]. Fig 2.7a depicts a pictorial of the probe positioning *(this is not a medical approved sketch. It is just for the purpose of this work)*:

- Position A (*Parasternal window*): The right ventricle is the most prominent part of the image. Could be challenging to find the right positioning of the probe and the position to get an optimal view of the heart.
- Position B (*Subcostal window*): The liver will serve as an acoustic window. The first chamber accounted in the US image is the right ventricle.
- Position C (*Apical window*): It provides a complete transthoracic cross section view of the heart; two-chamber, three-chamber and four-chamber views [17].
- Position D (*Suprasternal window*): The transducer is placed in the base of the neck. It provides a good long-axis image of the heart [17].

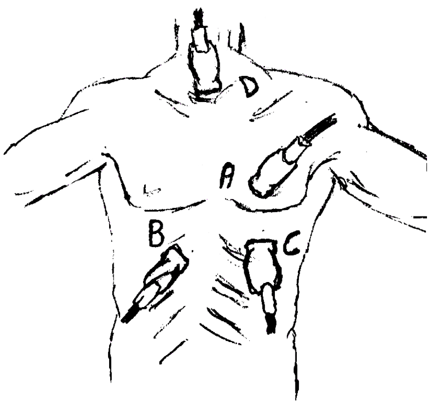

(a)

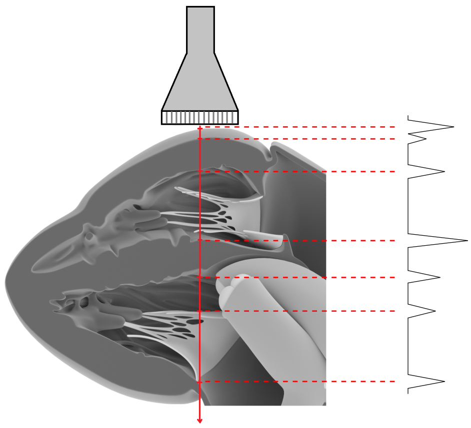

(b)

Figure 2.7.: **(a)** Cardiac examination windows. **(b)** Reflected US as echoes from tissue interfaces (left), sequence of electrical signals corresponding the amplitude of the returning echoes (right) [16, 18].

Finding the right angle and position is crucial to get a good image. However, continuous motion makes heart a tricky organ to image. In paragraph 2.2.3 it was mentioned that it is achievable to have a frame rate of 30 images per second. Image frame rate lies in the range of 6 fps up to 150 fps. Nevertheless, 30 fps is a trade-off between parameters such as *image depth* (affects the number of echos received per second), *sector angle* (affects the number of lines required per sector scan) and *image line density* (number of lines required per angle unit). Considering a sector angle of 90° and image depth 15 cm, the US image will constitute 200 scan lines and it will take 40 ms for a full beam sweep [16].

Along with brightness mode (B-mode), motion mode (M-mode) imaging continues to have a relevant application in heart imaging. It is fairly difficult to understand for a non-specialist, but given the high temporal resolution it remains superior to 2 dimensional US imaging. Temporal resolution is especially important for heart imaging to compensate for heart motion. There are many aspects of the heart to check during an imaging procedure. Most common ones are related to functionality of the heart such as valve movement, shape and size of the chambers, shape and size of the heart, and myocardium contractions. Using *Doppler* ultrasound it is possible to analyse the blood flow between the chambers, through the valves, and possible complications with aorta.

Transesophageal echocardiography

Transesophageal echocardiography is a type of echocardiography. It consists of a flexible tube with an US probe at the tip. The probe is guided down the throat into the esophagus. TEE is considered as a supplementary cardiac imaging technique. When it is not possible to get a good view of the heart using TTE, it is feasible applying TEE since the heart is close to esophagus. Additionally, TEE is used to guide cardiac catheterising. Primary applications of TEE are related to [19]:

- Cardiac source of embolism
- Infectious endocarditis
- Suspected prosthetic valve dysfunction
- Suspected aortic dissection, aortic aneurysm
- Mitral regurgitation

Transesophageal echocardiography usually is not the first choice for cardiac examination and does not lead to serious complications in general, however, the manoeuvring of the catheter is performed by a specialized cardiologist for this type of catheter to avoid possible complications which could lead to esophageal perforation and massive gastrointestinal bleeding. Transesophageal echo views are listed as below [19]:

- Low esophageal view
- Mid esophageal
- High esophageal view
- In the transgastric subcardiac view
- In the transgastric five-chamber view

- Aortic projections

In comparison to TTE, which enables four main examination windows (2.7a), TEE provides six examination windows.

Intracardiac echocardiography

Transthoracic echocardiography (TEE) is the gold standard for heart imaging. With the necessary knowledge and probe handling skills a complete heart scan can be accomplished. Thanks to its low cost, availability, radiation free, portability and the ability to evaluate both anatomy and the function of the heart, TTE serves as the workhorse of clinical cardiology imaging tools [17]. However, in some instances, TTE is limited from the health condition of the patient (obesity, pulmonary disease) or devices/ bandages attached on the chest wall of the patient as postoperative conditions. In such cases, the introduction of intravascular ultrasound (IVUS) in the late 1980s, to image the heart from inside out comes to great aid [20]. The miniaturised US probe (*IVUS probe*) is located at the tip of the catheter. This proximity of the probe with the object of interest contributes in increasing of *spatial resolution* (the ability of the system to discriminate between small adjacent objects) and *contrast resolution* (the ability to distinguish between different grey scale values) [20]. If we take IVUS a step further, introducing the transducer inside the heart chambers, the procedure takes a whole new approach. Intracardiac echocardiography (ICE) involves taking US images of the heart from inside out using a catheterised transducer. There are a few routinely exploited applications of ICE in interventional cardiology, such as tissue ablation, electrophysiological mapping, cardiac devices handling, and biopsies. In Tab. 2.1 are summarised a few characteristics of ICE technology. *Vitulano et al.* describes it as widely used intraoperative real-time imaging tool during invasive cardiac procedures [2].

Application of ICE in OR emerges from the necessity of cardiac interventions guid-

Table 2.1.: Feasibility analysis of intracardiac echocardiography (ICE) in clinical practice [1] [21].

Advantages	Related effects
No general anesthesia required	Increased safety for the patient
Reduced radiation dose	Reduced postoperative complications
Reduced hospitalization time	Reduced costs
No additional sonographer required	Less personnel required
Disadvantages	**Related effects**
High catheter maneuvering skills	Specific training required
Lack of re-usability	High costs
Lack of training systems	Lack of trained specialists
Lack of advanced 3D imaging capabilities	Limitation on MV interventions

ance. Considering the upsides (Tab. 2.1), intracardiac echocardiography has gained wide applications. Most widely performed interventional procedures using ICE are [2, p.3]:

- Transseptal puncture and interatrial defect closure
- Percutaneous valvular implantation and valvuloplasty
- Ablation of arythmias
- Lead extraction and device-related endocarditis
- Endomyocardial biopsy

Alkhouli et al. [22] and *Enriquez et al.* [21] provide extensive information on the applications of ICE in structural heart disease (SHD). Both articles provide a detailed guide of catheter maneuvering and probe positioning in order to get optimal views of different structures of the heart. More detailed analysis and information on the applications [2, 17, 20, 23].

2.4. Electromagnetic Tracking

Tool tracking in medicine is a common practice. It is stretched from its application on instrument localization/ counting in OR, to continuous tracking of medical devices within human body. Optical tracking systems are more reliable and provide better accuracy, however, electromagnetic (EM) tracking does not have the line-of-sight restriction [24]. Therefore, optical tracking systems are not suitable for tracking medical instruments, i.e. catheters, within the human body. This grants EM tracking a great potential for computer-assisted interventions guidance, navigation, and catheter tracking. The basic components for a tracking system are the field generator (Fig. 4.3a) and the magnetic sensor. Multiple sensors can be tracked, connected to the sensor interface (Fig. 4.3c). electromagnetic (EM) tracking is prone to errors. Essentially, the error is the deviation of the measured value from the true value. Typical errors of EM are classified as *static*, when the sensor remains in an unchanged position, and *dynamic*, which is associated to moving sensors.

Table 2.2.: Relative position error. The mean results from all possible distances of 50, 150, and 300 mm that can be calculated from the mean jitter positions. s.d. signifies standard deviation, from [24].

		Error (mm)			
EMTS	Distance (mm)	Mean	s.d.	Minimum	Maximum
NDI Aurora	50	0.96	0.68	-0.06	2.2
	150	2.72	1.79	0.50	6.04
	300	5.35	3.42	1.27	10.42

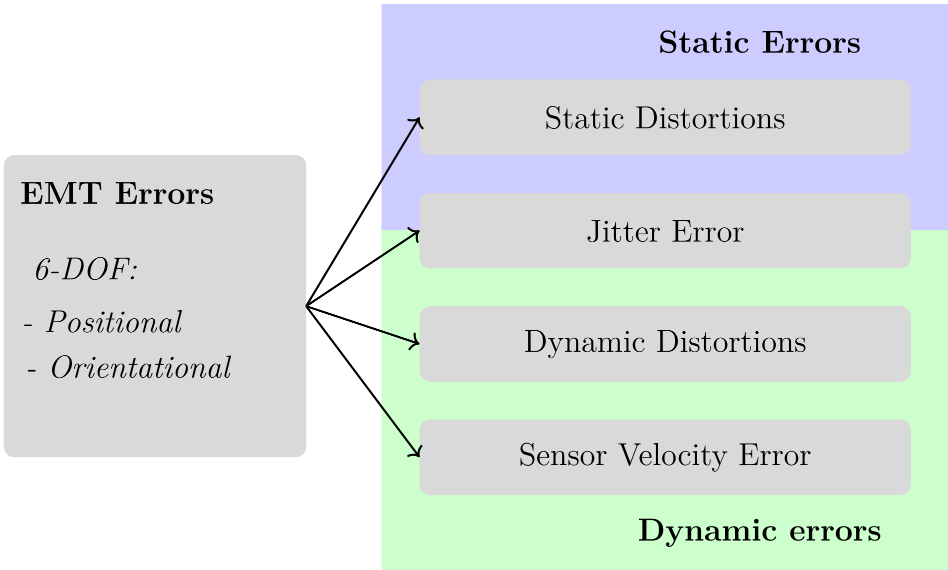

Figure 2.8.: Classification of EM tracking errors [25]

Static errors are subdivided into *static distortions*, i.e. systematic errors introduced into the system continuously and at a relatively known value, and *jitter error*, i.e. error introduced by random noise where the value of the error can not be predicted. Dynamic errors are subdivided into *dynamic distortions* and *sensor velocity error*. For EM tracking systems it is important to distinguish between *dynamic errors* and *static errors*. *Dynamic errors* can be minimized using filtering, while *static errors* can be handled using calibration [25]. Fig. 2.8 depicts a summary for the above mentioned errors in EMT technology.

There has been conducted much research for the accuracy assessment of EMT. *Hummel et al.* proposes a standardized protocol for accuracy assessment of tracking systems [24]. The accuracy of the *Aurora tracker*, according to *Hummel et al.*, is affected only by ferromagnetic materials. Their study shows that metallic distortions are more prominent close to the emitter. The measurement error Δr is proportional to the inverse of the third power of the emitter-metal distance d, i.e. $\Delta \mathrm{r} = 1/d^3$, [24, p.2377]. Tab. 2.2 shows the relative position error of the NDI aurora tracking system.

2.5. Mathematical Foundations

Electromagnetic Tracking

Electromagnetic tracking systems (EMTS) operate either with alternating current (ac) or with direct current (dc). EMTS operating with ac are more prone to error due to continuously inducing eddy currents in nearby metallic or ferromagnetic objects. EMTS operating with dc do not suffer from rapidly changing electromagnetic field, thus, dc trackers can drastically reduce metallic distortions [26]. The error in the position of the sensor, Δr, has the following relationship with the distances to the metallic or ferromagnetic materials [26]:

$$\Delta r \propto \frac{d_{tr}^4}{d_{tm}^3 \cdot d_{mr}^3} \tag{2.2}$$

where: d_{tr}^4 - distance from transmitter to sensor, d_{tm}^3 - distance from transmitter to metal object, d_{mr}^3 - distance from metal object to sensor.

Statistical Calculations

Quantitative evaluation is realized using Microsoft Excel. The measures used include mean value, standard deviation, minimum value, maximum value, first quartile (Q1), second quartile (median), third quartile (Q3), inter quartile range, lower whisker, upper whisker and 95% confidence interval. As a measure of accuracy it was used the population standard deviation, shown in Eq.2.3.

$$\text{Standard Deviation} = \sqrt{\frac{\sum(x_i - \mu^2)}{N}} \tag{2.3}$$

x_i : sample value, $\quad \mu -$ mean value, $\quad N -$ number of samples.

Freehand Ultrasound Calibration

In PLUS each coordinate system has a unique name. Let $FrameA$ be the coordinate system with the known values. Let $FrameB$ be the coordinate system with unknown values. The transformation matrix which correlates the point set of $FrameA$ to the point set of $FrameA$ will be named $FrameA\text{To}FrameB$, Eq. 2.4. This ensures an unambiguous name for any transformation between two random coordinate systems. The units of the values could be mm or pixel, depending on the coordinate frame we are referring to (see Tab. A.2).

$$FrameAToFrameB = \begin{bmatrix} R_{xx} & R_{xy} & R_{xz} & T_x \\ R_{yx} & R_{yy} & R_{yz} & T_y \\ R_{zx} & R_{zy} & R_{zz} & T_z \\ 0 & 0 & 0 & 1 \end{bmatrix} \tag{2.4}$$

For a given point in a reference frame, $FrameA$, and transform matrix $FrameA\text{To}FrameB$, the coordinate values of the point in $FrameB$ will be:

$$\begin{bmatrix} FrameB_x \\ FrameB_y \\ FrameB_z \\ 1 \end{bmatrix} = \begin{bmatrix} R_{xx} & R_{xy} & R_{xz} & T_x \\ R_{yx} & R_{yy} & R_{yz} & T_y \\ R_{zx} & R_{zy} & R_{zz} & T_z \\ 0 & 0 & 0 & 1 \end{bmatrix} \times \begin{bmatrix} FrameA_x \\ FrameA_y \\ FrameA_z \\ 1 \end{bmatrix} \tag{2.5}$$

The unit of T will be the same as the unit of $Frame\_B$, as T_x, T_y, and T_z are multiplied by one and the result is a position in $Frame\_B$. While, the unit of R is the unit of $Frame\_B$ divided by the unit of the $Frame\_A$, shown in Eq.2.6.

$$\begin{aligned} FrameB_x &= R_{xx}FrameA_x + R_{xy}FrameA_y + R_{xz}FrameB_z + T_x \\ FrameB_y &= R_{yx}FrameA_x + R_{yy}FrameA_y + R_{yz}FrameB_z + T_y \\ FrameB_z &= R_{zx}FrameA_x + R_{zy}FrameA_y + R_{zz}FrameB_z + T_z \end{aligned} \tag{2.6}$$

The matrix $FrameA\text{To}FrameB$ represents a rigid-body transformation, i.e affine transformation. This transformation is e composition of a series of transformations, including translation (Eq. 2.7) and rotations about x-axis(Eq. 2.8), y-axis(Eq. 2.9), and z-axis(Eq. 2.10).

$$T = \begin{bmatrix} 1 & 0 & 0 & T_x \\ 0 & 1 & 0 & T_y \\ 0 & 0 & 1 & T_z \\ 0 & 0 & 0 & 1 \end{bmatrix} \tag{2.7}$$

$$R_x(\Theta) = \begin{bmatrix} 1 & 0 & 0 & 0 \\ 0 & cos(\Theta) & sin(\theta) & 0 \\ 0 & -sin(\Theta) & cos(\Theta) & 0 \\ 0 & 0 & 0 & 1 \end{bmatrix} \tag{2.8}$$

$$R_y(\Phi) = \begin{bmatrix} cos(\Phi) & 0 & sin(\Phi) & 0 \\ 0 & 1 & 0 & 0 \\ -sin(\Phi) & 0 & cos(\Phi) & 0 \\ 0 & 0 & 0 & 1 \end{bmatrix} \tag{2.9}$$

$$R_z(\Psi) = \begin{bmatrix} cos(\Psi) & sin(\Psi) & 0 & 0 \\ -sin(\Psi) & cos(\Psi) & 0 & 0 \\ 0 & 0 & 1 & 0 \\ 0 & 0 & 0 & 1 \end{bmatrix} \tag{2.10}$$

Fig. 2.9 shows in a schematic fashion the steps of the transformation of the coordinates,

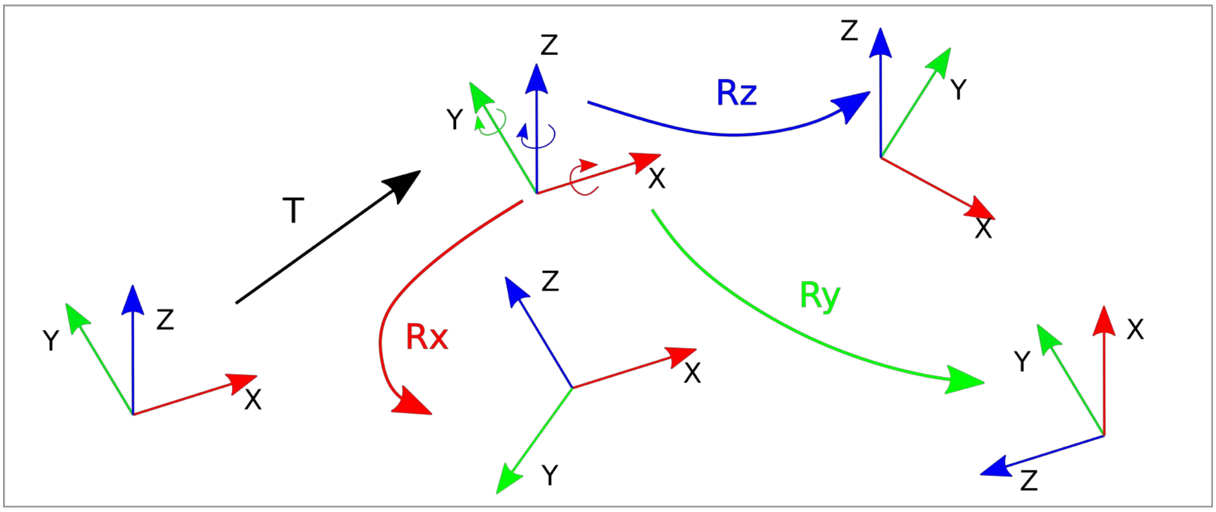

Figure 2.9.: Schematic of the process of the transformation of coordinates.

including translation (T), and rotation about X, Y, and Z axis (Rx, Ry, and Rz).

3. State of the Art

This thesis covers a wide range of topics, starting with electromagnetic tracking and navigation, instrument tracking, freehand tracked ultrasound, and three-dimensional ultrasound image compounding, image registration, etc. A combined knowledge about these areas of research was necessary to develop and run our system. In this chapter the relevant literature will be reviewed, analysed, and grouped accordingly.

3.1. Electromagnetic Tracking of Ultrasound Probes

Electromagnetic tracking is used to find the position and orientation of ultrasound images obtained from an ultrasound probe for navigation of interventional procedures or image compounding. Electromagnetic tracking is used in addition to multiple tracking methods, such as optical and acoustic tracking [27].

J. Wood et al. [28] used preprocedural images (CT, MR, PET) to guide wires, catheters, and needles using electromagnetic tracking in phantom models and animal studies. Previously acquired images were used and reconstructed based on the position and orientation of the tracked object. The images were acquired with fiducial markers attached to the skin or anatomical landmarks, which were later used for registration of the stack of images to the tracking system. The preoperative images are superimposed to the tracking information, which allows functional and/ or morphological information displayed during angiography, biopsy, and ablation procedures [29]. This three-dimensional information is especially important when performing ablation of complex structures, such as atrial fibrillation. For such interventions the real-time position and orientation of the catheter is displayed, within the pre-recorded 3D-CT scans [30] [31].

Lambert et al. [32] showed that electromagnetic tracking can be used to reduce X-ray exposure time and the amount of contrast media for endovascular aneurysm repair. Using path-based registration they registered the preprocedural 3D-CT data to the electromagnetic intraprocedural data. They used a plastic and a silicon based aortic phantom. The accuracy of the registration for the plastic phantom was tested using four reference landmarks, and for the silicon phantom by the ability of three surgeons to catheterise a renal artery using only the software for navigation.. A modified electromagnetic catheter was used to obtain the three dimensional position within the phantom's aortic lumen.

Franz et al. [33] attached a miniature field generator to an external ultrasound probe to combine EM tracking and US imaging in one handheld device. Their research prototype showed positional tracking accuracy and precision error below 1.0 mm and 0.1 mm respectively, and rotational error of $0.4 \pm 0.9°$.

3.2. Catheter Tracking

Generally, catheters are tracked electromagnetically via magnetic sensing elements either embodied within the ICE housing [35], or via attaching on the outer surface of the distal tip [36]. The application of traced catheters ranges from simultaneously tracking catheters and guidewires for arterial cannulation [37], combination of EP and EM tracking of the catheters [38] [39], catheter ablation of atrial fibrillation and atrial flutter [40] [41, 42], peripherally inserted central catheters [38] [43], etc.

Condino et al. [36]: Radiation dose during endovascular surgeries is high, e.g. 13.4±8.6 mSv for endovascular aneurysm repair, also injected contrast medium poses nephrotoxic effects. To reduce radiation dose and the contrast medium injection, an electromagnetic navigating system was developed to guide endovascular procedures. They presented two approaches for sensorized catheters: 1) attaching two 5-DOF sensors on the external surface of a traditional catheter (using biocompatible thin-walled heat shrink tubing), aligning their axis with catheter's axes. One sensor was positioned at the tip, and the other a few centimeters below. The coupling of the two 5-DOF sensors will provide 6-DOF and the curvature of the catheter's distal part can be acquired. 2) For the steerable catheters the sensors were inserted inside the catheter's lumen and the channels were sealed with silicone glue. The positioning of the sensors was similar as per first approach. The calibration was realized using a custom-made, 3D-printed phantom with radio opaque fiducials. The phantom was scanned with a 3DRA to determine the positions of the markers in the in the 3DRA reference coordinate system (RCS). Then the markers were localized with the tracking system to acquire the coordinates of the markers in the the Aurora RCS. The registration between two point clouds was accomplished using a least-squares error minimization algorithm. Results showed an accuracy of 1.2 ± 0.3 mm and positive feedback from the surgeons [44] [45].

Loschak et.al. [46] used a different approach for tracking ICE catheters electromagnetically. In addition to adding electromagnetic sensors at the tip, a kinematic model was created to describe the relationship between catheter tip location, catheter controls, and imaging plane orientation. The final goal was to create e robotic system for manoeuvring the catheter, based on the information of the location of the tip provided by EMTS. Their research focuses more into kinematic models, therefore not much information is provided on how they archived the correct visualization of the US image position and orientation within the working volume. In a later publication, additional to the robotic ICE steering system, their work extends to 3D mosaicing and automatic panoramic US imaging. The reconstructed volume is facilitated due to 3D spatial compounding, based on beforehand spatial calibration. Robotic-controlled steerable catheters reduce X-ray exposure of the surgeons and the staff, minimize the contrast medium injection, increase accuracy and precision of the procedures, and provide for telecontrolled interventions [47] [48, 49] [50].

Skowronek et al. [26]: Brachytherapy (BT) is the procedure that involves delivering radioactive material to specific areas inside the body for cancer treatment purposes. It provides concentrated and targeted radiation to the tumorous tissue over a short period of time, and consequently, lowering the incidence of radiation-related cancer occurrence. For temporary BT, catheters are used to deliver the radioactive source in place.

Zhou et al. [51] conducted a performance study for real-time catheter tracking using an EM tracking device for high-dose-rate prostate brachytherapy. Their study showed a submillimeter accuracy range (< 2 mm) with interfering objects present in OR. Also, they concluded that catheter reconstruction using EMT is faster, image-artifact independent, and more accurate in comparison to conventional methods. Electromagnetic tracking for catheter path reconstruction in US-guided and high-dose-rate brachytherapy interventions is widely researched [52] [53] [54, 55].

3.3. Freehand 3D Ultrasound Calibration

Freehand three dimensional ultrasound is a method that consists on continuously tracking and recording the trajectory of a 2D ultrasound probe while acquiring US data from a 3D volume.

Hsu et al. [56] provides comprehensive a review of freehand US probe calibration (they refer to external conventional US probes in general, not to a particular type of probe). Among others, they analyse multiple existing calibrations techniques and they compare them based on ease of use, speed of calibration, and reliability. Cambridge Phantom [57] and Cone Phantom [58] showed the best accuracy among other techniques. The analysed calibration techniques according to its principles are:

- Point phantom
  1. Point phantom without a stylus
     a) Point phantom formed by a pair of cross-wires: *Detmer et al.* [59], *Barry et al.* [60], *Huang et al.* [61], *Krupa* [62]
     b) Spherical bead-like object: *State et al.* [63], *Barrat et al.* [64]
  2. Point phantom with a stylus: *Péria et al.* [65], *Hartov et al.* [66], *Amin et al.* [67], *Viwanathan et al.* [68].
- Stylus: *Muratore and Galloway Jr.* [69].

- Three-wire Phantom: *Carr* [70].
- Plane Phantom: *Prager et al.* [57], *Langø* [71], *Varandas et al.* [72], *Ali and Logeswaran* [73].
- Two-plane Phantom: *Boctor et al.* [74]
- Two-dimensional Alignment Phantom: *Sato et al.* [75]
  1. Z-phantom: *Comeau et al.* [76,77], *Pagoulatos et al.* [78], *Lindseth et al.* [79,80], *Hsu et al.* [81], *Kreher et al.* [82].
  2. Mechanical Instrument: *Gee et al.* [83]
- Image registration: *Blackall et al.* [84]
- 3D probe calibration: *Hsu et al.* [56, p. 16]

3.4. Point set registration

Point-based registration aligns two or more data sets, i.e cloud points, using a certain number of corresponding points between the sets [85]. Among other types, rigid-body point-based registration is appropriate for rigid bodies, where the correlation between points within the same set remains unchanged [86, 87]. One of the data sets serves as correspondence while the other with be aligned according to it, based on a set of transformations (e.g. affine transformations) [88]. Essentially, the alignment between two given data sets is archived by finding the rigid-body transformations between homologous fiducial points and by minimizing fiducial registration error (FRE). The inaccuracy on finding the fiducial point during the registration process is known as fiducial localization error (FLE) [85] [89]. Fiducial registration error (FRE) is defined as the root mean square distance between the corresponding markers after registration. Another representative measure of registration accuracy is target registration error (TRE), which represents the distance between corresponding points, while FRE the distance between the fiducial centroids [86] [89].

Maurer et al. [89] presented a multimodal image-to-image, point-based registration of head volume images using implantable fiducial markers. They used four external markers, visible in CT and MR images. For the registration of the head images from the same patient they assumed rigid-body transformations. They were the first to suggested three measures of error for analysis of the accuracy of point-based registration methods: 1) FLE as the error for locating the fiducial markers (They specify the fiducial localization error in the images as FLE_I, and the fiducial localization error in physical space as FLE_P.), 2) FRE as measure of the registration accuracy, which is the distance between corresponding fiducials after registration and transformation, 3) TRE a more objective measure of the registration accuracy, as the distance between corresponding points other than the fiducial points after registration. An extensive review on point set registration is presented by *Zhu et al.* [90].

3.5. Three-Dimensional Ultrasound Image Compounding

Three-dimensional image compounding is widely used to improve the quality of echo images by superimposing multiple views of the object. The overlapping area exhibits a better image quality by reducing speckle noise, improving signal-to-noise-ratio (SNR) and contrast-to-noise-ratio (CNR) [91]. Three-dimensional image compounding is not the main purpose this thesis; however, few compounding methods will be presented.

Leotta and Martin. [92] implemented the early 3D compounding method based on mean overlapping intensities. This method seems to work good on improving SNR, but decreases CNR. The "mean method" produces a blurred image when the overlapping regions differ due to angle-view or artefacts, other than random noise alone. Additional to "mean method" they implemented the "maximum method". This method picks the highest intensity value for the final image. Choosing high intensity values reduces the low-intensity artefacts; however, high-intensity values due to noise will be passed also. Therefore, the "maximum method" increases CNR but decreases SNR.

Soler et al. [93] developed the "multi-view deconvolution" method. Their versatile method can switch between minimum, mean, and maximum values.

Rajpoot et al. [94] propose the wavelet method. They used wavelet transform to distinguish and partition the image into low-frequency and high-frequency bands.

Yao et al. [95] propose a new compounding method with the aim of improving SNR, CNR, reducing artefacts, and extending field of view. They used phased-based image registration, based on *Grau et al.* [96]. In their publication they explain in details the image registration algorithm, compounding method, and validation process. Their method includes a set of 10 images for the compounding process, and showed significant improvement in image quality compared to minimum, maximum, and mean methods in terms of SNR and contrast.

Much research is conducted about multi-view 3D echocardiography, including TTE, TEE probes, and other types of external ultrasound transducers [97] [98, 99] [100, 101]. However, 3D compounding using ICE catheters remains a challenging and not much researched area.

3.6. Related Work Summary

Electromagnetic tracking showed to have an extensive use in medicine, and especially for tracking ultrasound probes. In Sec. 3.1 it was shown the application of EM to track guidewires, catheters, and external ultrasound probes (probes used in contact with the skin). It was shown that the navigation through EM tracking is beneficial to improve the efficacy of the interventions, reduce the intervention time, or reduce the X-ray radiation dose. Additionally, catheter tracking showed to be beneficial for BT and for aneurysm repair procedures. Moreover, in Sec. 3.2 the EM tracking of ICE catheters was presented. Nevertheless, majority of the literature makes use of the localization of catheters for visualization of the position of the tip and the trajectory. Electromagnetic tracking of ICE catheters is done mainly for improving the maneuvering the catheter itself through a robotic system. So far, the related work does not facilitate from tracking ICE catheters electromagnetically for the purpose of visualizing the US image on real-time within the volume of the heart. This work will contribute on filling this gap, by tracking ICE catheters electromagnetically in order to evaluate and visualize the position and the orientation of the US image in three dimensional space.

4. Own Methods

In this chapter will be explained the methods that are used within the work of this thesis. In Sec. 4.1 will be explained the process of calibrating the system that will be used to track US images. This will be followed by the proposed implementation of the tracked ultrasound system, Sec. 4.2.

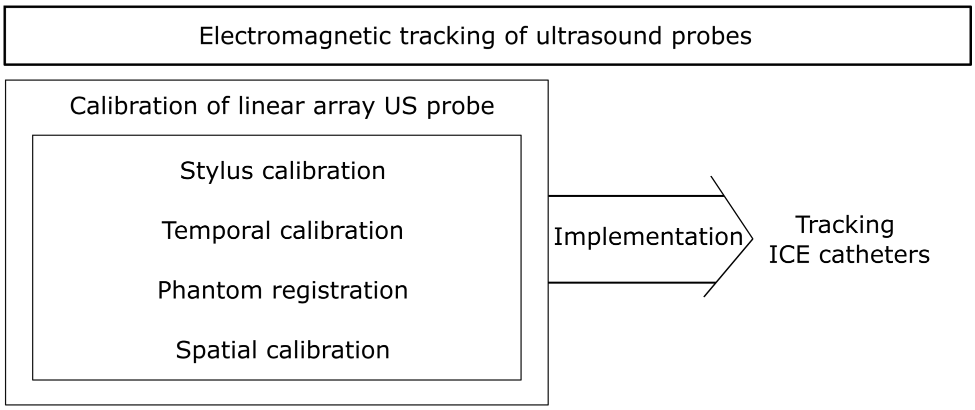

Figure 4.1.: Schematic of the methods used in this work.

This chapter will start with setting up a system for calibrating a linear array probe, as it is easier to start with. As shown in the Fig. 4.1, initially the calibration of the ultrasound probe will go through four calibration steps. Once the system is successfully calibrated, it is possible to adapt the setup for the ICE catheter, which will be covered in Sec. 4.2.

The setup for the initial calibration setup looks like in Fig. 4.2. All sensors attached to the objects, such as stylus, phantom, and probe should remain within the working volume of the FG. Moreover, the sensors are connected to the SIU (sensor interface unit). The sensor data from the SIU and data from the FG are fed to the SCU (system control unit). Ultimately, the computer collects the tracking data from the SCU and image data from US machine (via a frame grabber because the machine is not open for raw data). When this setup is functional it is possible to perform the calibration of the probe.

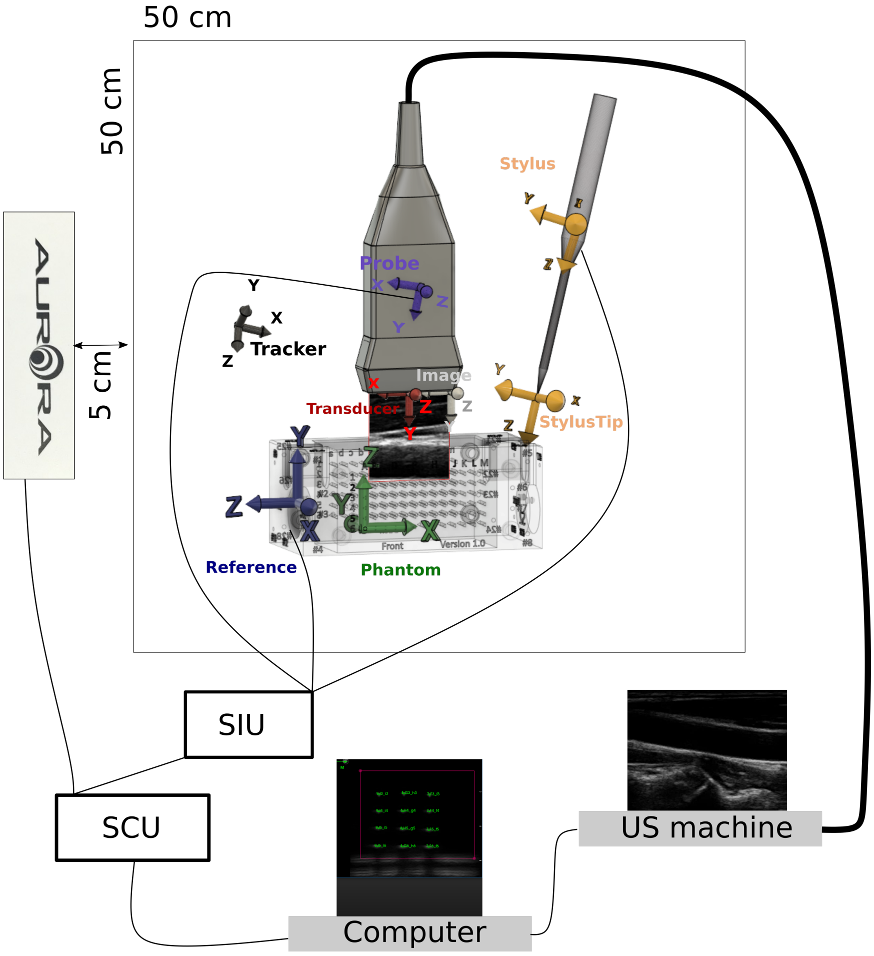

Figure 4.2.: schematic of the tools and methods that will be used throughput this work.

4.1. Tracked Ultrasound System Calibration

Calibration is done to couple electromagnetic (EM) with ultrasound (US). The process is realized using freehand tracked ultrasound calibration application (fCal), part of open-source PLUS library. PLUS application can be downloaded from the official website of PLUS [5]. NDI Aurora tracking system (Northern Digital Inc., Waterloo, Ontario, Canada) V2 along with planar field generator (FG) was used. The calibration process starts with stylus calibration, followed by phantom registration, temporal calibration, and finally spatial calibration. The algorithm calculates the transformation between a phantom's landmark and the reference marker by point matching. Sec. 4.1.3 describes in details the calibration of the system.

4.1.1. Tracking System

NDI's Aurora tracking system was used, which offers a sub-millimetric and sub-degree tracking accuracy. For Aurora 2, which has same accuracy characteristics as our system, the accuracy for 3D location lies in the range of 0.3 mm and 2.2 mm for a measurement range of 100 mm to 700 mm. The orientation error ranges from 0.1 to 0.35 degree [102]. The field generator that was used, shown in Fig. 4.3a, has a limited measurement volume. It covers a 500 mm cubic or dome measurement volume, projected outwards from the FG's front face. The measurements volume has an offset of 50 mm from the surface of the FG.

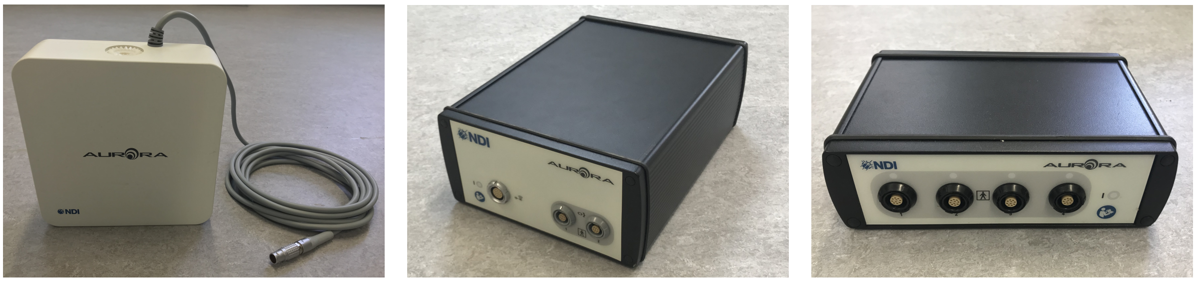

(a) (b) (c)

Figure 4.3.: NDI Auroa *(Northern Digital, Waterloo, Canada)* tracking system: **(a)** NDI Aurora planar field generator. **(b)** NDI Aurora System Control Unit (SCU). **(c)** NDI Aurora Sensor Interface Unit (SIU).

4.1.2. Data Collection and Transmission

The image data originate from different devices. It is not possible to have access to the image data directly from the ultrasound machine, therefore a workaround is necessary. The image data are collected from the screen of the US machine using a frame grabber ,*USB Capture HDMI Magewell*. Tracking data are collected from the NDI Aurora tracking system V3 *(Northern Digital Inc., Waterloo, Ontario, Canada* with planar field generator (FG).

Image Data

The frame grabber is connected to the US machine via a HDMI port and to the computer via a USB 3.0 port. It comes with an application where it is possible to adjust the settings as required. It is possible to crop, i.e. *clipping* in PLUS, the original image directly from the accompanying application, however, it is more feasible to crop the image in PLUS. Clipping in PLUS is pixel based, therefore its is neccesary to adapt the clipping region for each machine and US probe. A VideoDevice is to be added in the configuration file of PLUS for the collection of image data, see Sec. 4.1.3.

Tracking Data

The tracking data is provided from the Aurora tracking system. Similarly as for image data, a *"TrackerDevice"* for collecting the tracking data should be added in the configuration file of PLUS. Adding a third device, *"TrackedVideoDevice"*, the tracking data and image data will be merged into a single file, thus providing tracked images, given the completed calibration. More into calibration in Sec. 4.1.3.

OpenIGTLink

OpenIGTLink is an open-source network communication interface, specifically designed for image-guided interventions [103]. It is possible to transfer the tracked image data through OpenIGTLink. It supports certain types of data, e.g. image data, and/ or transform data. Data recorded in PLUS could be transferred through OpenIGTLink to 3D Slicer for real-time visualisation. With the latest developments it is also possible to conclude the calibration process in 3D Slicer alone [104].

4.1.3. Freehand Tracked Ultrasound Calibration

According to ISO, "calibration is the process of establishing the relationship between the values of a quantity indicated by a measuring instrument and the corresponding values indicated by a reference instrument" [105]. A sensorized catheter will be tracked on real-time within the volume of the field generator and calibrated, using Plus toolkit. To achieve this it is necessary to calibrate temporally and spatially the 5-DOF sensors attached to the catheter. As mentioned in paragraph 2.3, two 5-DOF sensors are required to provide both position and orientation information of the catheter. Since the US image is related to the transducer body, consequently to the catheter tip itself, the orientation of the image will remain unchanged and fixed, relative to the catheter tip. Having this in mind, tracking the catheter will be translated into tracking the US image. To get to spatial calibration of the probe it is necessary to go through few prior calibration steps. The final goal of the calibration process is to determine the transformation between the coordinate system of an object, e.g. Stylus, Phantom or Probe, and the coordinate system of a marker sensor rigidly attached to the object. The calibration process is undertaken according to the guide provided from *Lasso et al.* [5] (online).

Configuration File

PLUS comes with a set of configuration files, for different hardware, and models ready-to-use. It is neccesary to adjust, add, or remove certain sections. Each section has dedicated

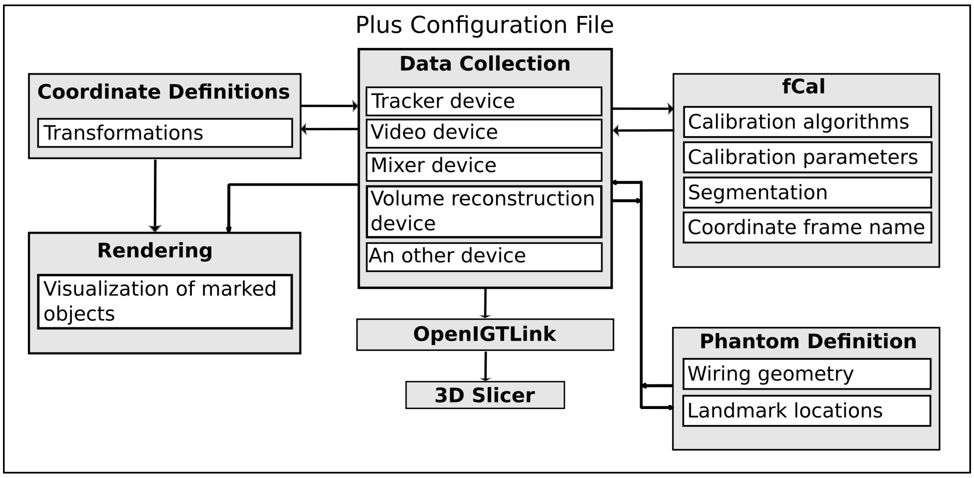

Figure 4.4.: Organisation of sections in the configuration file. Arrows point the direction of information flow [5].

functionalities. Fig. 4.4 comprises the contents and basic functionalities of each section. Settings for each device can be adjusted and saved in the XML file format. It is possible to transmit data through OpenIGTLinkServer, for instance to 3D Slicer [106]. The XML files can be easily edited with a simple text editor application from the fCal application window.

Stylus calibration

(c)

Figure 4.5.: Stylus calibration using fCal: **(a)** Coordinate definitions used by fCal for stylus calibration. **(b)** *Aurora 6DOF Probe, Straight Tip, Standard* (online). **(c)** Completed calibration of the stylus.

Aurora 6DOF Probe, Straight Tip, Standard (online)(Fig. 4.5b) is used. The stylus is provided calibrated from the vendor, however, for reproducibility of the process the calibration step is undertaken. For setting up the EMTS, *Aurora ToolBox* and *NDI Architect* software are used (online). Within the "fCal.exe" directory, some basic configuration files are ready-to-use for certain device sets. Occasionally it is neccesary to make some adjustments. A marker sensor is attached to the stylus body. The marker has its own coordinate system, denoted as "Stylus" in PLUS, depicted in Fig. 4.5a. Interesting to find is the location of the tip of the stylus, therefore, "StylusTip" represents the coordinate system of the tip. After the calibration process, PLUS will make necessary transformations between the two coordinate systems. During the calibration the tip of the stylus is maintained fixed at a chosen point within the FG's working volume. One of the landmarks of the calibration phantom was used. Preferably, the tip should remain in an unchanged position, and the distal part is moved around on a circle or ellipsoid trajectory. This continues until the number of calibration points is achieved. The number of calibration points acquired is defined prior in the configuration file under the "fCal" parameter named "NumberOfStylusCalibrationPointsToAcquire". As a rule of thumb, 200 calibration points to acquire are required. Fig. 4.5a depicts the marker's coordinate system named "Stylus", and "StylusTip" represents the origin of the coordinate system, which is located at the tip of the stylus. Fig. 4.5c depicts the end of the calibration process. The blue dots in the figure demonstrate the calibration points acquired along the trajectory the sensor is moved. As we mentioned, the stylus is already calibrated, therefore the dots are located at the tip. A good calibration accuracy is with an error smaller than one millimeter (pivot calibration error < 1 mm) [5].

Phantom registration

A new calibration phantom is designed, depicted in Fig. 4.6a [82]. The new design brings new features such as: 1) Channel to be suitable for catheter calibration, 2) new method for attaching 6-DOF reference sensor with predefined coordinates, 3) Multiple landmarks for registrations, 4) triangular holes for grid of fiducial wires. Triangular shape offers a better stability of the fiducials than circular one offered by Plus itself.

Materials used for phantom registration are: (a) already calibrated stylus depicted in Fig. 4.5b, (b) calibration phantom with a rigidly attached 6DOF sensor (*Aurora 6DOF Reference, 25 mm Disc, Standard Introduction*) on the side of the phantom, depicted in Fig. 4.6b. In the configuration file, under the section "PhantomDefinition", the landmarks used for phantom registration are defined according to their coordinates within the phantom coordinate system, depicted in Fig. A.5. The origin of the 3D coordinate system of the phantom corresponds with the inner side of hole A6, see Fig. 4.6a. In our trial, ten landmark points are used. They are named respective to the number in the phantom body. The phantom registration algorithm computes the transformation between the phantom coordinate system, named "Phantom", and the coordinate system of the marker attached to the phantom body, named "Reference", as shown in Fig. 4.6a. The registration process starts with the tip of the stylus at the first landmark. The algorithm should

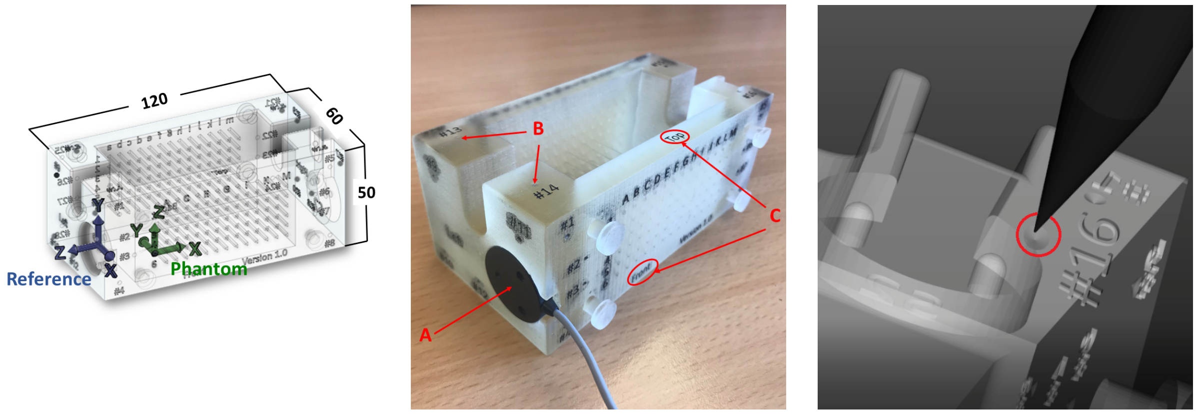

(a) (b) (c)

Figure 4.6.: **(a)** Novel calibration phantom design (dimensions in mm) [82]. **(b)** A - Reference sensor, B - registration landmarks, C - Markings for the orientation of the phantom. **(c)** Stylus pointing landmark 16.

automatically recognise and register each landmark, otherwise it can be manually recorded with the "record landmark" command in fCal application. As the process continues with the remaining landmarks to be recorded, the 3D model of the phantom will appear in the screen. Already recorded landmarks will turn green, while the next landmark to be recorded will appear in orange color. When the process is completed it is possible to continue with temporal calibration, or save the results as a new XML file. Results can be saved after each step. The registration error should be in two millimeter range (2 mm $\pm$ 0.3 mm). For testing purposes, landmark #16 is pointed with the tip of the stylus, Fig. 4.6c. The tip should be in the center of the circular landmark shape. The calibration error is optimal when the stylus tip is within the landmark circle (radius of the landmark circle = 1 mm). When the registration process is completed, a transformation matrix will be generated in the configuration file, which translates the position of the "Phantom" relative to the position of the "Reference".

Temporal calibration

Temporal calibration as a concept consists on synchronising multiple data sources. It is crucial to have an accurate temporal aligning of the data collected from different hardware. Each hardware has its own internal clock, based on which the data originating are temporally sorted. When dealing with several devices, each hardware provides data with timestamps according to their own internal clock [5].

Some other devices do not provide timestamps at all. In this scenario, the data collector computer attaches as a timestamp the acquisition time. In principle, temporal calibration correlates timestamps between different data sources. *Lasso et al.* explains in details temporal calibration between two or more devices [5] (online).

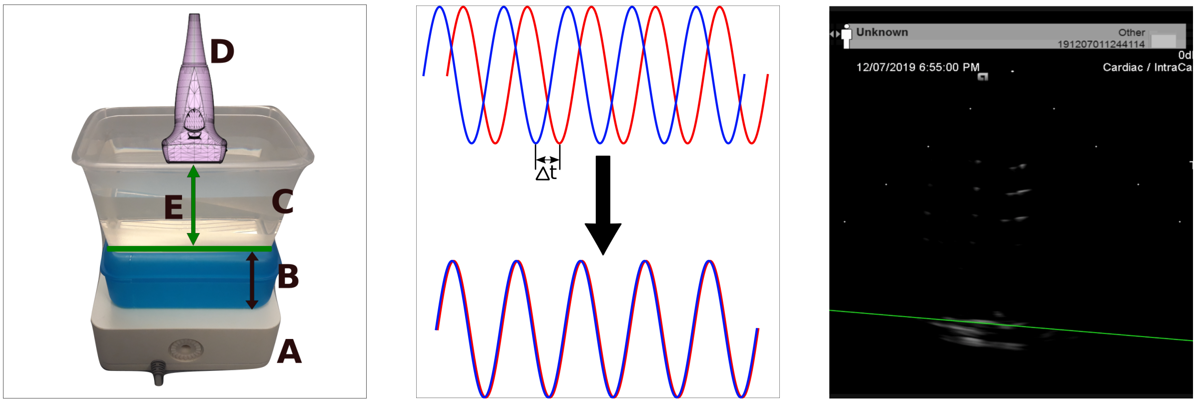

(a) (b) (c)

Figure 4.7.: **(a)** A - FG, B - distance from FG at least 5 cm, C - water tank, Solution consists of boiled water and alcohol (ratio 9:1), D - ultrasound probe, E - maximum distance acceptable for the bottom of the tank (green line) to be visible in the US image. **(b)** Schematic of temporal aligning of video and tracking data. Δt symbolises the time-offset between the data streams. **(c)** Green line shows the bottom of the tank in fCal application.

The goal of the temporal calibration is to find the time offset between the tracking data and the image data. For the procedure its is required a tank of about 3.5 litres volume and 20 cm depth, depicted in Fig 4.7a. Calibration data are collected from the algorithm while performing linear quasi-periodic motion of the tracked US probe. The motion consists on repeated up and down movements of the probe. The probe should always remain submerged in water during the calibration process. The algorithm detects the bottom of the tank and uses it as a point of reference in the ultrasound image. A green line, as depicted in Fig 4.7c, shows the bottom of the tank as the calibration continues. It is necessary to complete at least five quasi-periods of movement. A high number of periods is not recommended as the segmentation algorithm might introduce errors due to lagging.

After the temporal calibration, the time-offset between the tracker data stream and ultrasound images (denoted as *videostream* in PLUS) is calculated, depicted in Fig. 4.7b. The offset must be in the range of milliseconds. In our trials it remained between 100 ms and 300 ms. Calibration correlates the signals in the time domain based on the offset value. The sine waveform corresponds to quasi-periodic movement of the tracked US probe. In the graphs it is possible to count eight full quasi-periods, Fig. A.1 A.2.

Spatial calibration

Stylus calibration, phantom registration, and temporal calibration are the prerequisites for proceeding with spatial calibration. The goal is to find the image-to-probe transformation, Fig. 4.10a. A pattern of wiring using fishing line is constructed. The geometry of the wiring pattern should be defined in the configuration file along with the position of the

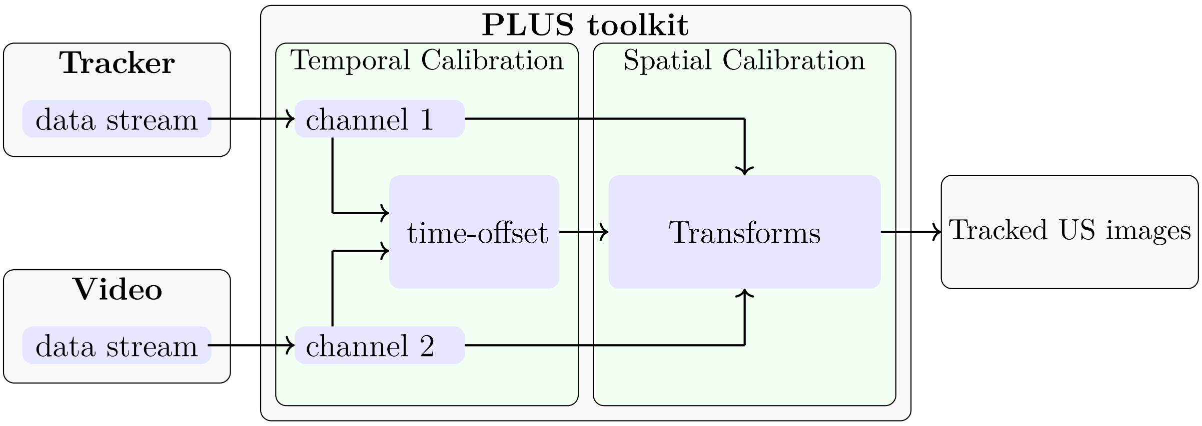

Figure 4.8.: Schematic of temporal and spatial calibration of data streams.

landmarks. The coordinates are defined according to the *Phantom Coordinate System*. The wiring of the phantom is depicted in Fig. A.3 and Fig. 4.9. The design is open-source and can be downloaded for free [82]. The calibration process is performed with the calibration phantom submerged in the water tank, depicted in Fig. 4.7a. The tank contains degassed water to avoid introduction of noise in the ultrasound images due to particles in the solution. In this work a solution containing nine parts water and one part alcohol (above 70%) is used. The aim is to achieve a mixture with a speed of sound similar to that of soft tissue, 1540 m/s.

The calibration process starts with the calibration phantom submerged in the solution. The probe is oriented with the marked side towards the A1 fiducial opening of the phantom, Fig. 4.10b. The wires in the phantom should appear as small light gray blobs, otherwise *gain* and *depth* are to be adjusted accordingly in the ultrasound machine. The transducer should remain submerged in the mixture all along the process. Green dots appear in the screen according to the pattern of the fiducial wires, Fig. 4.10c. The probe should be moved in up-down and front-back directions, and held orthogonal to the wires direction, as shown in Fig. 4.10b. Tilting or rotating the probe might loose track of the pattern of the wires. Scanning movement is slow and the echo image should cover all fiducial wires. Depending on the imaging depth that is interesting for us, the distance of the probe to the wires should be adjusted accordingly, e.g. for an accuracy at the depth of about 4 cm

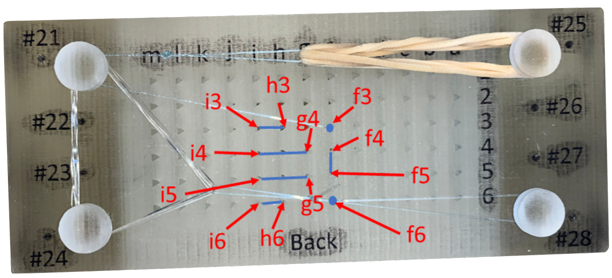

Figure 4.9.: Back side of the calibration phantom. Fishing wire is used for fiducial lines. Rubber band is used to keep the lines stretched.

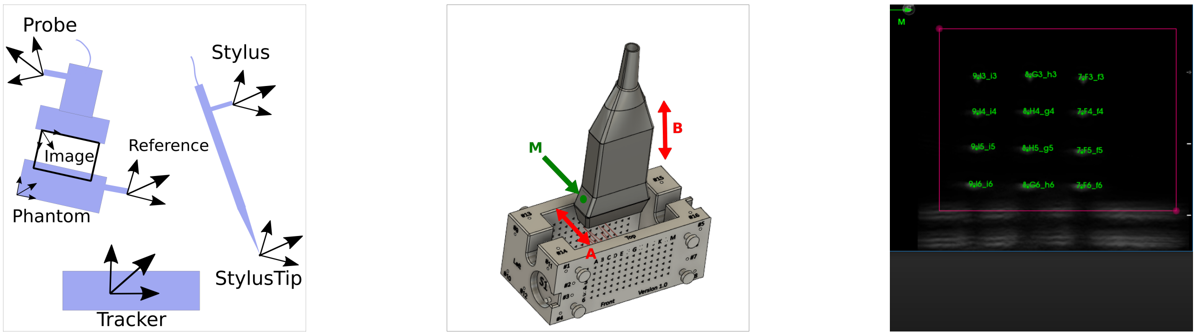

(a) **(b)** **(c)**

Figure 4.10.: Spatial calibration using fCal: **(a)** Coordinate definitions used by fCal during calibration. **(b)** A - linear movement of probe front-back, B - linear movement of the probe up-down, M - Marked side of the probe pointing A1. **(c)** Fiducial lines appear as green dots in fCal.

the motion range of up-down movement could be 2, 4 and 6 cm. These actions ensure an optimal calibration accuracy. Fig. 4.12 summarizes the most crucial conditions to be fulfilled for a successful spatial calibration.

Another aspect to consider is the image orientation. The calibration correlates one particular image orientation to a certain setup. It is important to distinguish the image orientation defined by the manufacturer of the US probe and the image orientation defined in PLUS. *SonoScape L742* linear array and *Siemens AcuNav ICE catheter* ultrasound transduces were used, as depicted in Fig.4.11. The orientation of the ultrasound transducer axes is defined and can not be changed. According to these definitions there are four possible image orientations for the 2D B-mode images:

1. **MF**: Image X - axis = M & Image y - axis = F
2. **MN**: Image X - axis = M & Image Y - axis = N
3. **UF**: Image X - axis = U & Image Y - axis = F
4. **UN**: Image X - axis = U & Image Y axis = F

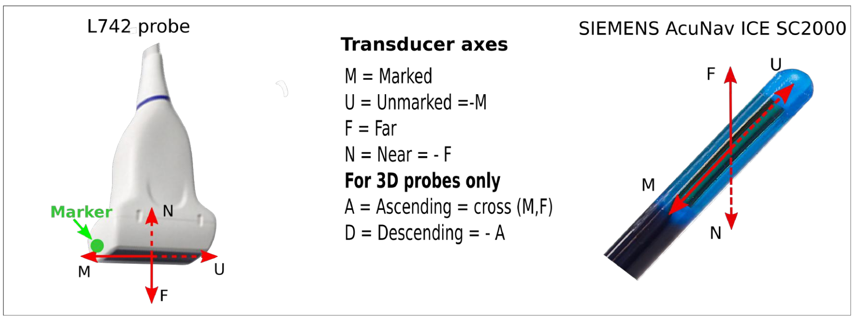

Figure 4.11.: Image orientations for L742 probe and SIEMENS SC2000 (2D application) [5] [107].

PLUS uses by default MF as image orientation. However, it is possible to perform any required flipping operation of the image between Marked - Unmarked, Far - Near, and Ascending - Descending. Flipping is an operation defined by PortUsImageOrientation, attribute of the VideoDevice. To make sure that the orientation of the image is correct, the marked side of the transducer is pointed with the finger and the movement is screened in the upper-right corner of the screen in fCal, close to marked side. The transducer surface appears on the top of the image. An example of image orientation in PLUS is shown in Fig. 4.13b. The x - axis points towards the increase of x in the image and the same direction as M (marked side of the transducer). The y - axis in the image points towards the increase of y and the same direction as F (far axis of transducer). However, this particular image orientation might not hold true for other experimental setups. Adjustments should be done accordingly, considering the specific setup of the markers and US machines. In the paragraph below the coordinate definitions used by PLUS and by fCal will be explained.

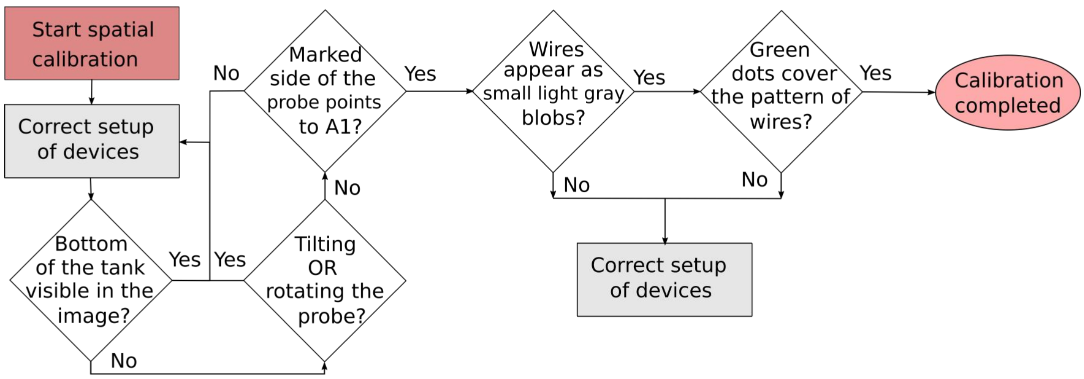

Figure 4.12.: Flowchart of steps for spatial calibration.

Coordinate System Definitions and Transformations

The goal of spatial calibration is to find the transformation between the object and its belonging marker sensor. The pose data, i.e. position and orientation, are acquired from the tracking system and the image data from the frame grabber. The pose of image slices, stylus, phantom and probe are defined by a 3D Cartesian coordinate system and the respective transformations. In PLUS, each coordinate system is named specifically according to the identification name, i.e. *"ImageCoordinateFrame = Image"* stands for the coordinate system of the image slice. Tab. A.2 elaborates the definitions for all coordinate frame names used in fCal. Transformations are carried on as *FrameAToFrameB*, where *FrameA* and *FrameB* refer to a specific coordinate system. In our setup we are tracking three objects, namely the stylus, the probe, and the phantom. Fig. 4.13a depicts all coordinate definitions used by fCal for each object, including image slices and tracker.

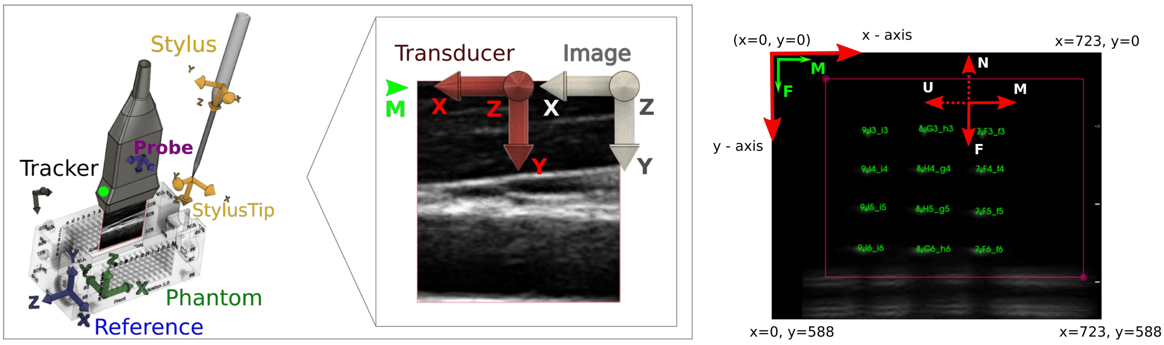

(a) (b)

Figure 4.13.: **(a)** Coordinate system definitions used by fCal for pose estimation and rendering. **(b)** Example of image orientation in PLUS (green arrows). Red arrows show direction of transducer axes relative to the image.

Essentially, the transformation maps the points of the coordinate system *FrameA* to the coordinate system of the *FrameB*, according to Eq. 2.5.

Such spatial transformations are called affine transformations. For each point (x_A, y_A, z_A) in a coordinate system, a mapping can be defined into the coordinates of an other coordinate system (x_B, y_B, z_B) [108]. This mapping can be expressed through a simple matrix multiplication:

$$FrameB = M * FrameA \tag{4.1}$$

where FrameA is the vector of the coordinates of the old coordinate system, and FrameB is the vector of the transformed coordinates, as described in Eq. 2.5. Typically, matrix M describes three translations (shifts), one for each axis, and three rotations about the cartesian coordinate axes.

$$M = T * R_x * R_y * R_z \tag{4.2}$$

Eq. 2.7 describes the matrix T, for the implementation of a rigid translation, and Eq. 2.8, 2.9, and 2.10 carry out rotations about X, Y, and Z axes (Θ, Φ and Ψ in radians) [108].

Visualization of Models

Within fCal it is possible to visualise objects upon selection. Once the objects, i.e. models, images, axes are spatially oriented according to the *WorldCoordinateFrame* (the coordinate system used as the reference from all displayable objects). Using *Rendering* component in the configuration file all objects included will be visualised according to the position relative to *WorldCoordinateFrame*. Transformations included in rendering do not affect the actual spatial orientation of the objects. *TransducerCoodinateFrame*, *TransducerOriginCoodinateFrame*, and *TransducerOriginPixelCoodinateFrame* in PLUS are used only for visualization purposes, as described in Tab. A.2.

4.2. Proposed Implementation of Tracked Ultrasound

After explaining the fundamentals of EM tracking and its applicability to track US images, this section will shed light on the proposed application of tracked ultrasound with the purpose of creating a visual aid for catheter manoeuvring in the heart.The implementation of tracked ultrasound images in "CardiTrain" simulator includes three major steps. First, tracking the ICE catheter by attaching sensors at the tip. Second, building the setups for the 3D-printed heart model. Last, registering the actual model of the heart to the 6-DOF sensor attached on the side of the box, explained in Sec. 4.2.2.

4.2.1. Tracking Intracardiac Echocardiography Catheter

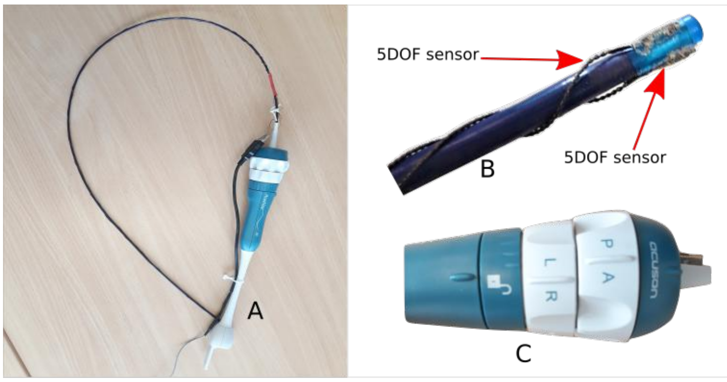

Figure 4.14.: **A** - SIEMENS AcuNav ICE catheter, **B** - Tip of the catheter with attached sensors, **C** - handle of the catheter; left-right, posterior-anterior, brake.

Two 5-DOF sensors are rigidly attached at the tip of the SIEMENS AcuNav ICE catheter, as depicted in Fig.4.14. Both 5-DOF sensors are required to get full 6-DOF, position and orientation. The sensors do not obstruct the FOV of the transducer, which consists on a sector shape of transducer elements with a 90°angle. First, the purpose of tracking the catheter is to test the accuracy of tracking the position and orientation of the US image generated from the ICE probe. Second, its application on visualizing the position and orientation of real-time US image within a 3D-printed heart model. In Sec: 6, the accuracy of the tracked ultrasound images using ICE catheter will be tested and compared with the accuracy of SonoScape L742-linear-array and Siemens TEE probe.

4.2.2. Setup for Heart Model Registration

In order to be able to register the heart it is necessary to fix the printed model rigidly, relative to a reference sensor. For this purpose a box is designed and 3D-printed. The box contains six faces filled with holes, as depicted in Fig. 4.15a. The holes serve to allow a laminar flow of the water inside the box later on for the experimental procedure, and possibly for insertion of the stylus tip during the registration process. A 6-DOF sensor will be attached on the side of the box. Notice that Fig. 4.15b shows a clipper used for attaching the whole calibration phantom to the side of the box, for flexibility of the experiment setups. Fig. 4.15c depicts the real-life setup of the encased 3D-printed heart model. Only plastic screws are used for the fixation of the heart and the phantom to avoid any possible disturbance in the electromagnetic field.

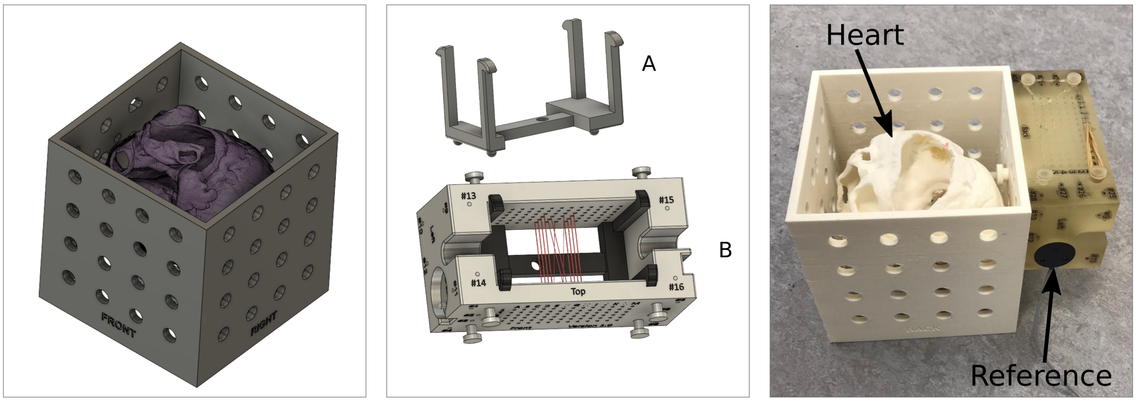

(a) (c)

Figure 4.15.: **(a)** Virtual model of the heart encased in the box. **(b)** A - Phantom clipper, B - Clipper inserted from underneath of the phantom. **(c)** Encased real-life model with attached reference sensor on the side.

Registration of the Heart Model

Now that the setup for the heart model registration is build, it is necessary to define the landmarks for the registration process. Since the heart is an unknown geometry, it is not possible to have predefined landmarks as it was for the calibration phantom [82]. The registration will be carried on using fCal application as part of Plus toolkit.

Registration via fCal will follow the same approach as per calibration phantom. The coordinates of the landmarks of the heart will be inserted in the configuration file. The landmarks will be pointed with the stylus in the predefined order. The calibration error is reported by fCal after the registration is completed and it should not exceed 2.3 mm.

Registration using ICP algorithm.

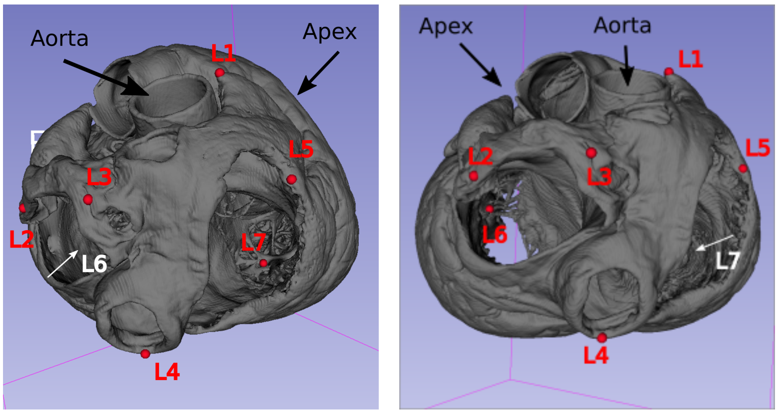

(a) (b)

Figure 4.16.: Seven heart landmarks points: **(a)** landmark six (L6) is not visible, **(b)** landmark seven (L7) is not visible.

Landmarks of Heart Model

Seven landmarks are randomly chosen for heart registration, depicted in Fig. 4.16. The landmarks are easy distinguishable and reachable with the stylus. In the 3D-printed model the landmarks are painted in permanent red color, insoluble in water. To find the coordinates of the landmarks two techniques are used:

1. Virtual model
    - 3D Slicer [106]
    - Autodesk Fusion 360
2. Aurora Tracking System
    - Using the tracker as reference system
    - Using the 6-DOF sensor as reference system

After yielding the sets of the coordinates from both techniques, a quantitative assessment will be carried on for the distances between landmark pairs. The distances will be compared, because the absolute coordinates of the landmarks vary between setups. The results according to each setup will be shown in Sec. 6. The origin of the heart virtual model (VM) is approximately in the center of the model. However, it is not relevant to this process since PLUS handles the coordinate transformation process, as discussed in Sec. 4.1.3.

4.2.3. Ultrasound Image Position and Orientation

The goal of this thesis it to accurately visualize the position and orientation of the US image generated from ICE catheter while being manoeuvred inside the heart. The visualization can be achieved using fCal. As discussed in Sec. 4.1.3, using rendering option, the heart model can be visualized relative to the position of the *Reference*. To obtain such orientation the *PhantomToReference* transformation matrix is required, which will be generated after registration process. Nevertheless, in order to achieve an accurate US image positioning and orientation of the image within the heart model it is crucial that spatial calibration is done correctly.

Image Position

ImageToProbe transformation will define the correct location of the US image within the FG measurement volume. The position of the images is tested using *CrateSliceModels*, part of PLUS. It creates a surface model of the tracked frame positions and gives an idea of the slice location within the scanned volume.

Image Orientation

Image orientation describes the relation between the visualized image content and the actual content of the US image, e.g. the marked side of the transducer on the US machine should match to the marked side denoted in fCal (see Fig. 4.13). The orientation of the image does not effect the position of the US echo image, only the contents of the slice. The orientation should be correct in case of a 3D spatial compounding of ultrasound images. To test the image orientation a straight object is scanned. The images are acquired moving the probe in a straight-line-single-sweep, making a slight abrupt shift of the probe (left or right). If the image orientation is correct the reconstructed volume will be smooth and without breaks in the surface. *VolumeReconstruction* tool, also part of PLUS, generates the reconstructed volume from the tracked US frames.

5. Experiments

This chapter presents five experiments conducted during the work of this thesis. Experiment one is an extent of the previous chapter, Sec. 4.1.3. Experiment two deals with testing the tracked echocardiography catheters and EMTS, Sec. 5.2. In Experiment three the system was used to record the landmark positions of the heart model, a.k.a object of unknown geometry. Additionally, the heart will be scanned with ICE and TEE probes, Sec. 5.3. Experiment four is conducted to test the influence of echocardiography probes on tracking accuracy of the EMTS, Sec. 5.4. Finally, in Sec. 5.5 experiment five is described for the registration of the 3D-printed heart model.

5.1. Freehand Tracked Ultrasound System Calibration

After explaining the setup for the calibration of the system, the initial calibration with L746 linear array probe will be carried on. The setup of this experiment was extensively explained in the previous chapter, therefore not much details will be given here. In the results chapter (Ch. 6) will be shown the quantitative evaluation of the calibration process.

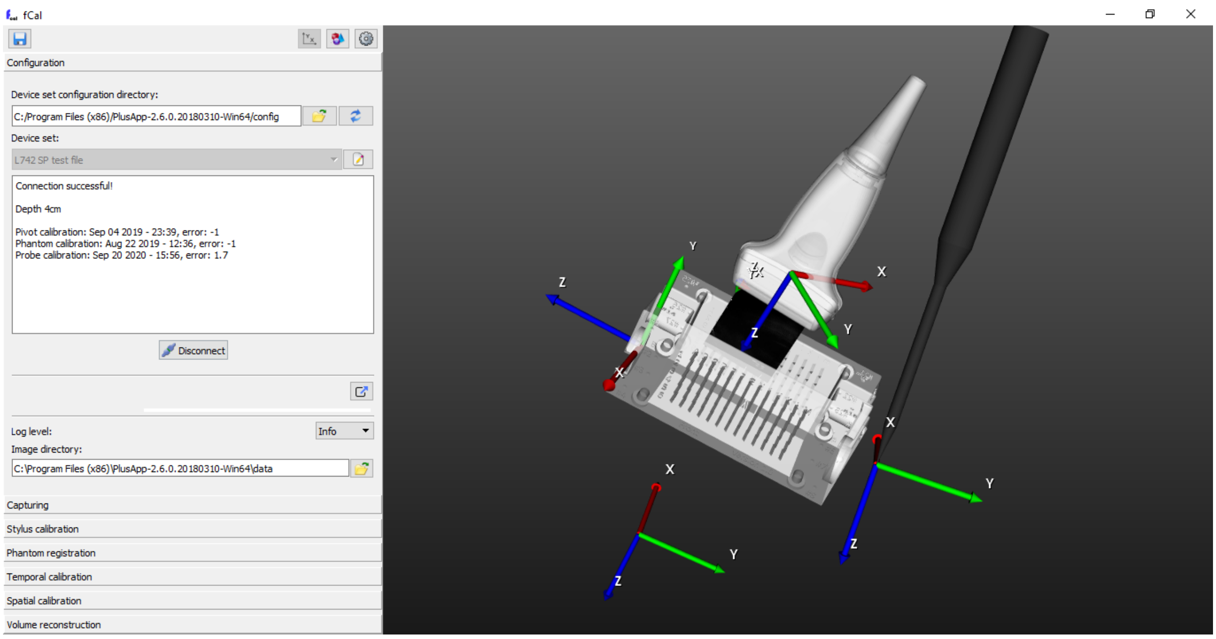

Figure 5.1.: fCal screenshot. Calibrated tools with the respective reference coordinate system axes, including the coordinate system of the tracker.

5.2. Scanning an Object of Known Geometry

The calibration process explained in Sec. 4.1.3 ensures that the reported location from the system relates to the movements of the tracked objects. To test the calibrated system a simple object of known geometry will be used. A 3D-printed test phantom is designed as the known geometry object, depicted in Fig. 5.2. The location of eight corners of the cubes, i.e.landmarks, will be recorded. The 6-DOF sensor and the tracker will used as reference coordinate system (RCS), two setups for each method. For each setup the recordings of the coordinates will be repeated five times, therefore, in the end of the day there will by four data sets with the coordinates of eight landmarks. Each data set contains five measurements for each point (landmark). The goal is to compare the results between data sets and define which whether tracker or a sensor is more suitable to serve as RCS. Additionally, the phantom will be scanned with ICE-2D and TEE-3D ultrasound probes.

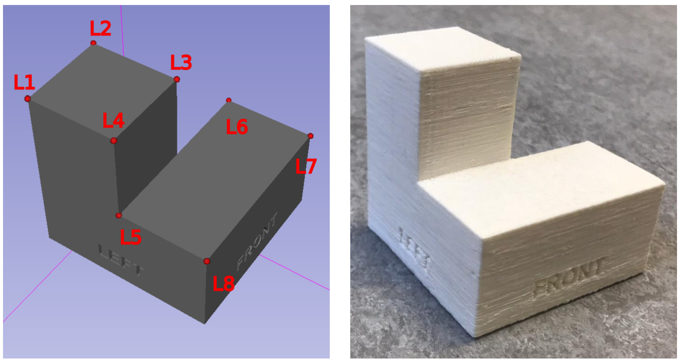

(a) (b)

Figure 5.2.: Known geometry object: four identical cubes, 25 mm edge. **(a)** Landmark annotations on the virtual model. **(b)** 3D-printed model.

5.2.1. Electromagnetic Tracking System

The purpose of these experiments is to quantitatively assess the error of the EMTS when using the tracker as RCS and when using the 6-DOF sensor as RCS. The error will be calculated in terms of standard deviation over five measurement for each landmark.

Tracker as Reference

In one of the setups the tracker sensor was used as RCS. The test phantom was attached rigidly to a cone-beam CT angiography laboratory table, and the FG was attached under the table by a distance of 100 mm from the test phantom. The recordings are done with metallic and ferromagnetic disturbance-free to the EMTS. The coordinates of the landmarks were recorded by pointing the tip of the calibrated stylus at each landmark.

They were recorded starting from landmark nr. 1 to the landmark nr. 8 in increasing order. The process was repeated five times.

6-DOF as Reference

In the second setup the 6-DOF sensor was used as RCS. Contrary to the setup where the tracker is used as RCS, here the coordinates of the landmarks will be recorded relative to the 6-DOF sensor. The sensor is attached rigidly to the table where the cubic phantom is taped. The recording of the landmarks is repeated in the same way as for the tracker.

5.2.2. Tracking Echocardiography Probes

TEE Probe

A Z6M TEE probe (Siemens Healthineers GmbH, Erlangen, Germany) was equiped with a 6-DOF sensor, Fig. 5.3a. The calibration process was repeated 10 times using fCal, PLUS toolkit. After calibration, the test phantom was scanned laterally performing slow and linear movement while scanning, depicted in Fig. 5.3b. The results of the calibration process are shown in Sec. 6.1.

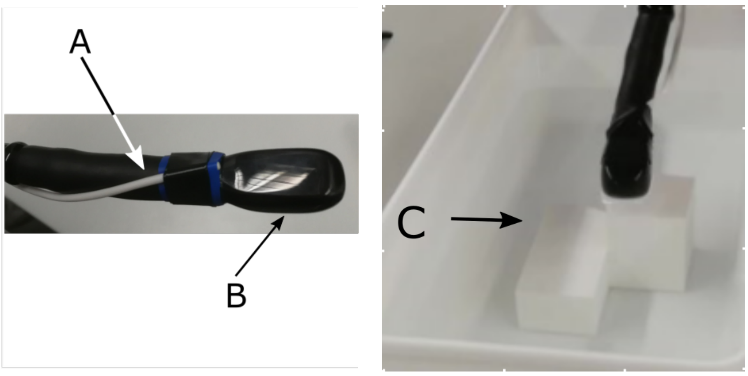

(a) (b)

Figure 5.3.: Z6M TEE probe: **A** - 6DOF sensor, **B** - head of the TEE probe, **C** - test phantom.

ICE Probe

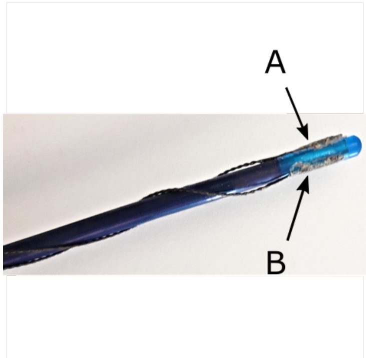

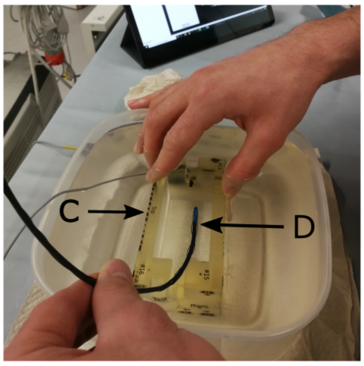

(a) **(b)**

Figure 5.4.: Siemens AcuNav ICE catheter calibration: **A** and **B** - 5DOF sensors, **C** - novel calibration phantom, **D** - ICE catheter.

Additionally to TEE probe, intracardiac echocardiography (ICE) transducer was calibrated. Two 5-DOF sensors were attached at the tip of the catheter. The sensors are configured to provide full 6-DOF, depicted in Fig. 5.4a. In the same fashion as per TEE, the novel calibration phantom is used for the calibration process [82]. Ten calibrations were performed with the calibration phantom and the ultrasound transducer submerged in water tank, see Fig 5.4b. For the experiments it was used degassed water.

5.3. Scanning an Object of Unknown Geometry

In the experiment three an object of unknown geometry is used, i.e. the 3D-printed heart model. As part of this experiment the procedure is similar as for experiment one.

1. The landmark positions of the heart are recorded using the EMTS by pointing the tip of the stylus at each landmark. The process is repeated five times.
    - Using the tracer as RCS (the setup is similar as in experiment one, Sec. 5.2).
    - Using the 6-DOF sensor as RCS (the setup is similar as in experiment one, Sec. 5.2).
2. The heart phantom is scanned from the outside laterally.
    - Scanning with tracked ICE probe, Fig. 5.5b.
    - Scanning with tracked TEE probe, Fig. 5.5c.

The heart phantom, depicted in Fig. 5.5a, was fixed in the water tank and the 6-DOF sensor was fixed with tape on the outer side of the box.

(a) (b) (c)

Figure 5.5.: **(a)** VM of the heart, **(b)** scanning the outer side of the heart with tracked ICE probe, **(c)** scanning the outer side of the heart with tracked TEE probe.

5.4. Effect of Intracardiac Echocardiography Transducers on the Accuracy of EMTS

Experiment three is designed to evaluate the influence of the ICE and TEE ultrasound probes on the accuracy of the EMTS. For this purpose a board is designed to test the accuracy of the tracking system in presence and proximity of the transducer. As reference for the design is used *Hummel et al.* [24]. A detailed protocol for this experiment is described in Appendix C.

Relative positional accuracy

The plate has 110x110 mm dimensions and 5 mm thickness. It is designed using Autodesk Fusion 360 and 3D-printed. The position of the sensor attached to the ICE catheter will be recorded for each hole, while the ICE probe is ON. The distances for the recorded positions

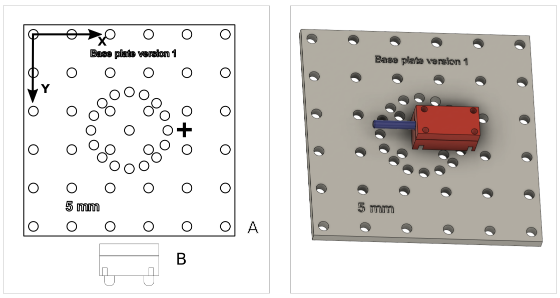

(a) (b)

Figure 5.6.: Base plate and sensor mount for tracking accuracy: **(a)** A - Base plate with a pattern of thirty-six equally distanced holes. Circular pattern of sixteen holes with a radius of 20 mm and angular difference of 22.5°. B - Sensor mount for ICE catheter. **(b)** Sensor mount serves to hold the ICE catheter fixed. Two pins fit in the holes.

will be calculated and compared with the distances of the base-plate. It is not possible to determine the exact position of the sensor attached to the catheter tip, therefore distances will be calculated. That will produce the differential tracking error. The recording of the coordinates for the rectangular pattern starts at the origin of the cartesian coordinate system and continues along positive direction of x-axis, as depicted in Fig. 5.6a. The process is repeated along the positive direction of the y-axis.

Relative angular accuracy

For the circular pattern the process starts at the hole near the "+" sign and proceeds counterclockwise. The ICE catheter is kept rigidly fixed in the sensor mount, as shown if Fig. 5.6b. In order to evaluate the differential angular tracking error the recordings for the circular pattern will be repeated for each axis of the tracker coordinate system. The FG will be moves in three different positions according to each axis, as depicted in Fig. 5.7.

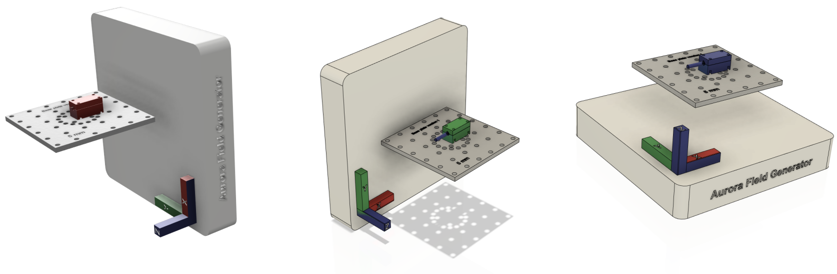

(a) (b) (c)

Figure 5.7.: Position of the FG for defining angular tacking error: **(a)** Rotating around z-axis. **(b)** Rotating around y-axis. **(c)** Rotating around z-axis.

5.5. Registering 3D-Printed Heart Model

The registration process involves transforming the coordinate system of one data set, i.e. source data set, into the the coordinate system of an other data set, i.e. target set. For heart registration two methods will be used. First, registration using fCal application, part of PLUS. Second, registration using ICP algorithm.

5.5.1. Registration via fCal

The registration is carried on through linear transformations. The algorithm takes a set of points from the source, recorded via registration process by pointing the tip of the stylus at defined landmarks, and matched with the target data set. The landmarks for

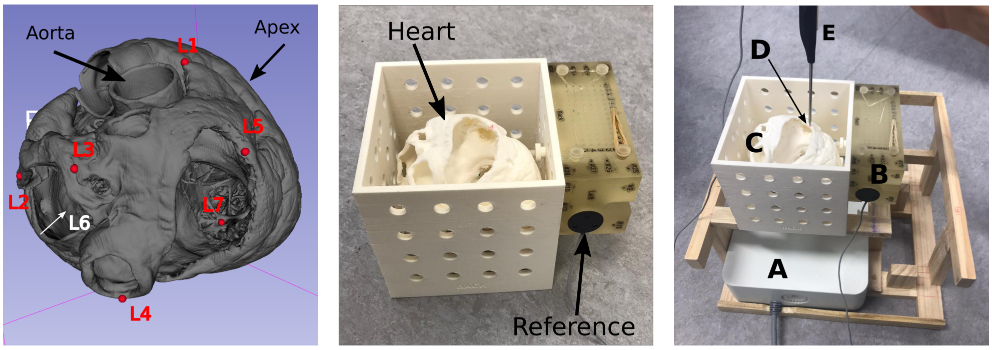

(a) (b) (c)

Figure 5.8.: **(a)** Location of the landmarks used for registration. **(b)** encased heart with attached 6-DOF sensor, **(c)** Registration process with the stylus: A - FG, B - calibration phantom with the reference sensor, C - heart phantom, D - landmark (L5), E - stylus.

the target data set are manually entered into the configuration file. The coordinates of the landmarks for the heart phantom were acquired in experiment two. However, the coordinates of the landmarks used for the configuration file are obtained from the VM of the heart. It is necessary to use the coordinates from the VM because they should be relative to the origin of the model. While the coordinates acquired from experiment two are relative to either the tracker RCS or 6-DOF sensor RCS. The configuration of the heart phantom landmarks is shown in Fig. 5.8a.

The heart phantom in fixed inside the box. For flexibility of the procedure the sensor is not removed from the calibration phantom, instead the whole phantom is attached on the side of the box, depicted in Fig. 5.8b. The landmarks are painted in red color and are clearly visible. The tip of the stylus is pointed at each landmark, starting with L1 and finishing with L7, as shown in Fig. 5.8c. For each landmark the "record landmark" is pressed on the fCal application window. When the registration process is completed the model of the heart appears on the screen and the registration error is calculated from the program. Given the calibrated probe, the system can visualize the position and orientation of the US image within the heart model.

6. Results

The results of measurements and experiments conducted are presented in this chapter. In Sec. 6.1 will be shown the results for the initial calibration of the tracking system. This is followed by the results of the heart registration process, in Sec. 6.3. . Finally, in Sec. 6.4 will be shown the results of the experiments for the accuracy of the tracking system.

6.1. Experiment 1: Freehand Tracked Ultrasound System Calibration

The calibration of the tracking system was carried on with ten-trial rule. In this section the calibration results will be shown for each step and explanatory graphics will be presented to make the data easier to grasp.

6.1.1. Stylus Calibration

Calibration experiments for the stylus are conducted for two reference frames, namely 6-DOF sensor and Tracker. Mean error of 0.33 mm, 0.65 mm and standard deviation of 0.05 mm, 0.11 mm respectively for the 6-DOF sensor and tracker as reference coordinate system was found, see Tab. 6.1. Standard deviation is calculated according to the formula in Eq. 2.3. For both methods the accuracy of the calibration is acceptable, in the sub-millimeter range. The results show a narrower distribution of the error for the 6-DOF sensor as reference coordinate system. A graphical representation of the error distribution of the stylus calibration is depicted in Fig. 6.1a.

Table 6.1.: Error of the stylus calibration for ten trials (Trial error), mean value (Mean), standard deviation (s.d.), minimum (Min.), and maximum (Max.) values.

	Trial Error (mm)													
ReferenceFrame	1	2	3	4	5	6	7	8	9	10	Mean (mm)	s.d. (mm)	Min. (mm)	Max. (mm)
6-DOF	0.3	0.36	0.31	0.30	0.29	0.33	0.26	0.44	0.33	0.38	0.33	0.05	0.26	0.44
Tracker	0.4	0.73	0.67	0.53	0.77	0.59	0.73	0.75	0.68	0.71	0.65	0.11	0.40	0.77

The corresponding values for the box plot are; lower whisker 0.22 and 0.42, Q1 (first quartile) 0.30 and 0.61, median 0.32 and 0.69, Q3 (third quartile) 0.35 and 0.73, upper whisker 0.43 and 0.92, $IQR(Q3 - Q1)$ 0.05 and 0.12 for 6-DOF and tracker respectively. Lower whisker is calculated as $Q1 - 1.5IQR$ and upper whiscker $Q3 + 1.5IQR$. Values 0.44 and 0.40 are outliers for 6-DOF and tracker respectively, see Fig. 6.1a.

6.1.2. Phantom Registration

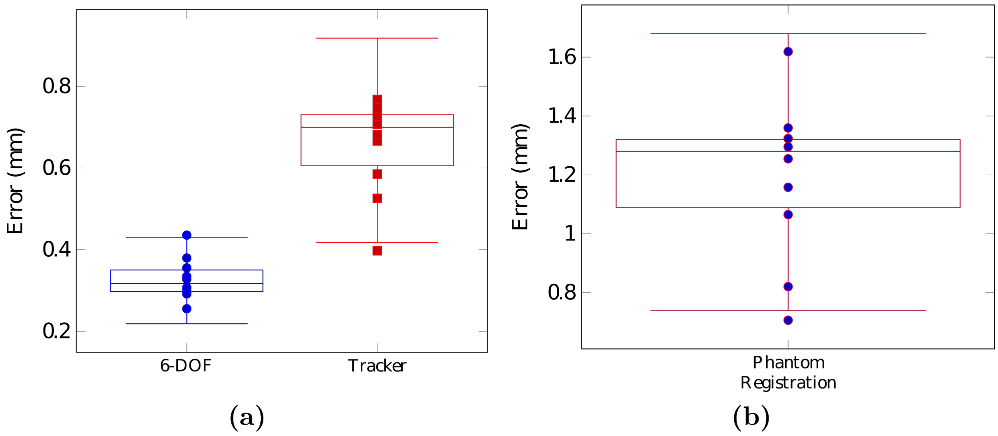

Figure 6.1.: Calibration results: **(a)** Stylus calibration based on Tab. 6.1 data. 6-DOF (6-DOF sensor used as RCS), Tracker (Tracker used as RCS). **(b)** Phantom registration error for ten trials.

In contrast to stylus calibration, for phantom registration is only possible to use the 6-DOF sensor as reference coordinate system (RCS). However, ten-trial rule is applied to analyse the behaviour of the calibration setup. Fig. 6.1b depicts the error distribution as a box plot. Mean error was 1.19 mm and standard deviation 0.26 mm. The corresponding values for the box plot are; lower whisker 0.74, Q1 (first quartile) 1.09, median 1.28, Q3 (third quartile) 1.32, upper whisker 1.68, $IQR(Q3 - Q1)$ 0.24. Lower whisker is calculated as $Q1 - 1.5IQR$ and upper whiscker $Q3 + 1.5IQR$. The value 0.71 is a lower outlier, while from the remaining three of them falling in the 50% IQR, with two remaining values in the lower 25% range and four in the upper 25% range. The registration error remains within the acceptable range 2 ± 0.3 mm. All values are in millimeters.

Table 6.2.: Error of the phantom registration for ten trials (Trial error), mean value (Mean), standard deviation (s.d.), minimum (Min.), and maximum (Max.) values.

	Trial Error (mm)													
ReferenceFrame	1	2	3	4	5	6	7	8	9	10	Mean (mm)	s.d. (mm)	Min. (mm)	Max. (mm)
6-DOF	1.62	1.32	1.36	1.32	1.25	1.16	1.30	0.71	0.82	1.07	1.19	0.26	0.71	1.62

6.1.3. Temporal Calibration

Results of the experiments using SonoScape US machine and L742 linear array transducer show differences in time-offset for different imaging depths.

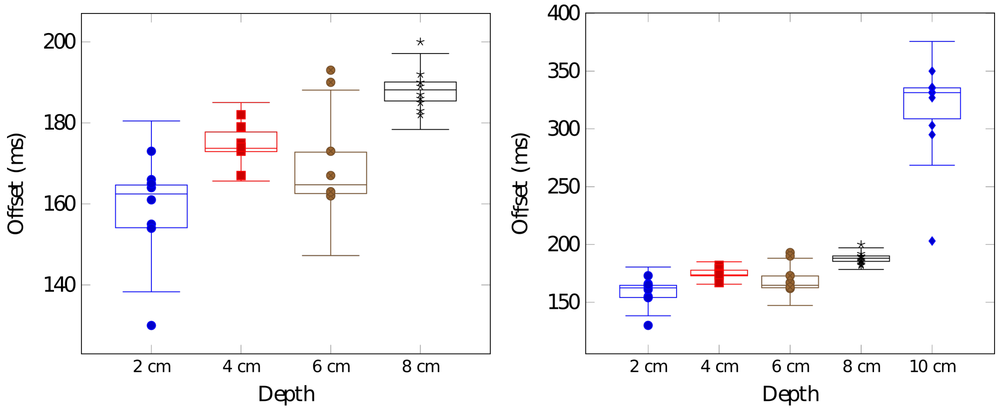

(a) (b)

Figure 6.2.: Box plot of the time-offset at five imaging depths over ten trials for L742 linear array probe: **(a)** Depth two, four, six, eight mm. **(b)** Depth ten mm added from sub-figure a.

The distribution of time-offset for 2, 4, 6, 8, and 10 cm imaging depths is depicted in Fig.6.2. For each depth ten trial experiments are conducted. Fig. 6.2a shows depths 2, 4, 6, 8 cm, while in the Fig. 6.2b the plot for 10 cm values is added. This separation is done for better visualisation. The data shows that there is a relative increase of time-offset value as the imaging depth is increased. For the depths 4 and 8 cm there is a narrower data distribution and a standard deviation of 4.45 and 4.88 ms respectively. The system has a similar behaviour with a lower outlier at 130 ms and two upper outliers at 190 and 193 ms for depths 2 and 6 cm respectively. The statistical calculations data for plots in Fig. 6.2 are shown in Tab. 6.3. The time-offset values for each trial are shown in Tab. A.1.

Table 6.3.: Temporal calibration for L742 linear array probe SonoScape at five different imaging depth values. Mean value over 10 trials (Mean), population standard deviation (s.d.), minimum value (min), maximum value (max), first quartile (Q1), second quartile (Median), third quartile (Q3), Interquartile range (IQR), lower whisker (Low), upper whisker (Up).

Depth (cm)	Mean (ms)	s.d. (ms)	Min. (ms)	Max. (ms)	Q1 (ms)	Median (ms)	Q3 (ms)	IQR (ms)	Low (ms)	Up (ms)
2	159	11	130	173	154	162	165	11	138	180
4	174	5	167	182	173	174	178	5	166	185
6	171	11	162	193	163	165	173	10	147	188
8	189	5	182	200	185	188	190	5	178	197
10	315	40	203	350	309	331	336	27	269	376

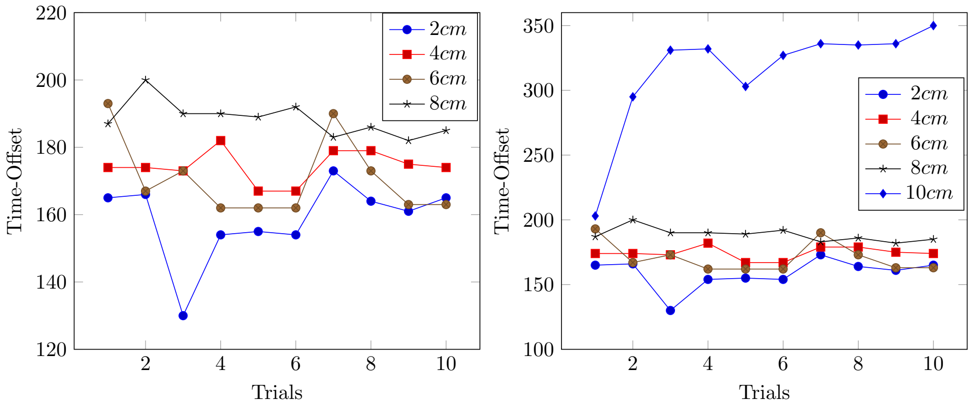

Figure 6.3.: Line graph of the time-offset at five imaging depths over ten trials for L742 linear array probe: **(a)** Depth two, four, six, eight mm. **(b)** Depth ten mm added from sub-figure a.

For the imaging depth of 10 cm the system has a mean time-offset of 315 ms and standard deviation of 40 ms. That shows the highest offset and the highest standard deviation among other imaging depths. Temporal calibration seems to work with a relatively similar behaviour for 2, 4, 6, and 8 cm depth. As depicted in Fig. 6.3, the distribution of the time-offset amoung ten trials is similar for all imaging depths, except for 10 cm.

6.1.4. Spatial Calibration

Spatial calibration results for three ultrasound transducers will be shown. Additionally, results for various imaging depths will be compared. Fig. 6.4 depicts the calibration error for TEE, SIEMENS ACUSON AcuNav, and SonoScape L742-linear-array probes. The data corresponds to ten calibration trials for each transducer. The calibration for TEE probe was cumbersome. The dimensions of the probe made it difficult to manoeuvre; therefore, the mean calibration error is higher and has a higher standard deviation.

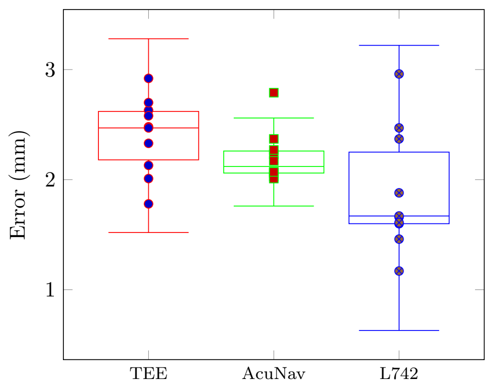

Figure 6.4.: Spatial calibration for TEE, AcuNav (ICE), and L742 linear array transducer.

The calibration of the L742 transducer produced the lowest mean error, i.e. 1.88±0.52 mm, but the highest standard deviation. On the other hand, the error for L742 probe has the widest distribution among all three transducers. For the evaluation of the standard deviation it is constantly used the formula in the Eq.2.3. With 95% confidence, the calibration error will fall in the range of 2.40±0.20 mm, 2.20±0.14 mm, and 1.88±0.32 mm for TEE, AcuNav (ICE), and L742 linear array transducers respectively. The distribution of the error has a similar pattern between the calibration results for TEE and L742 transducers. However, the mean and median value remain the lowest for L742 probe.

Table 6.4.: Spatial calibration error statistics for TEE, AcuNav, and L742 SonoScape-linear-array transducers over ten trials. Mean value (Mean), population standard deviation (s.d.), minimum value (Min.), maximum value (Max.), first quartile (Q1), second quartile (Median), third quartile (Q3), interquartile range (IQR), lower whisker (Low), upper whisker (Up), and 95% confidence interval (95% CI).

Transducer	Mean (mm)	s.d. (mm)	Min. (mm)	Max. (mm)	Q1 (mm)	Median (mm)	Q3 (mm)	IQR (mm)	Low (mm)	Up (mm)	95% CI (mm)
TEE	2.40	0.33	1.78	2.92	2.18	2.47	2.62	0.44	1.52	3.28	0.20
AcuNav	2.20	0.22	2.01	2.79	2.06	2.12	2.26	0.20	1.76	2.56	0.14
L742	1.88	0.52	1.17	2.96	1.60	1.67	2.26	0.65	0.63	3.22	0.32

6.2. Experiment 2: Known Geometry Object

In this section the results from first experiment will be presented. First, the results for the accuracy of the distances between landmarks in Sec. 6.2.1. Then, the results for the three dimensional volume compounding will be presented in Sec. 6.2.2.

6.2.1. Landmark Distances

Measurement precision

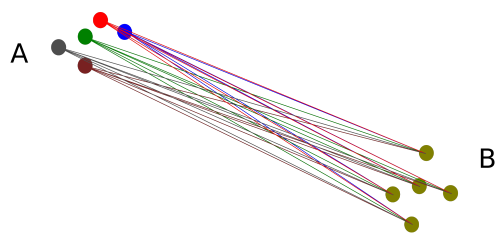

Figure 6.5.: Given five measurements for point A and point B, there can be calculated 25 different distances.

For two given points only a true euclidean distance exists. Given the absolute coordinates on a 3-dimensional domain, it is straightforward to find the distance. However, when the absolute coordinates are not known, consequently, the absolute distance can not be calculated. Given point A and point B in a 3-dimensional domain, and five measurements for each point, it is possible to calculate 25 sample distances between A and B, as depicted in Fig. 6.5. With this method the variability of the accuracy for between different landmark distances can be evaluated, therefore, the precision of the measurement.

For comparison purposes three techniques were used to find the coordinates of the landmarks: tracker as reference system, a 6-DOF sensor as reference system, and the coordinates from the virtual model (VM). The coordinates vary from one setup/ technique to an other, therefore a comparison between the coordinates obtained from different techniques is not appropriate. Instead, the measurement precision of the landmark distances different techniques will be computed. The positions of the seven landmark within the body of the heart model are shown in the Fig. 4.16. By definition, the technique represents multiple setups where the RCS remains the same, e.g. tracker as RCS is one technique, and 6-DOF sensor as RCS represents an other technique.

Tracker as RCS

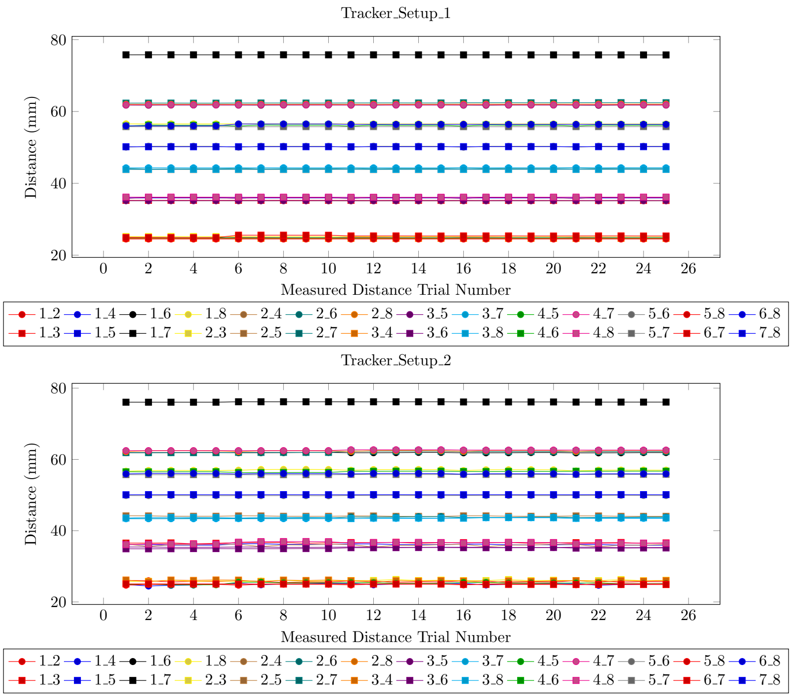

Figure 6.6.: Twenty five measured landmark pair-distances for the tracker as RCS. Measurement of precision (see Fig: 6.5).

The measured distances between eight landmarks of the test phantom are shown in Fig. 6.6. For eight landmarks there are twenty eight distinct landmark distances. Given five measurements for each landmark, twenty five measured distances are shown for each landmark pair. In the figure are shown two setups where the tracker is used as RCS. A mean standard deviation of 0.04 mm & 0.12 mm, and range of the error of 0.24 mm & 0.25 mm for first and second setup respectively. A straight line depicts a low variability, therefore a high precision. Both setups exhibit a high measurement precision.

6-DOF sensor as RCS

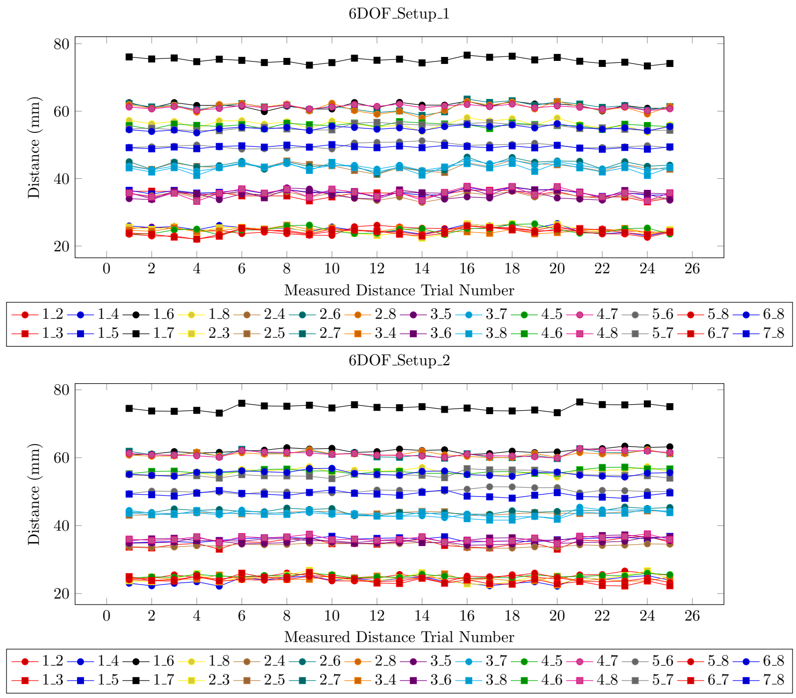

Figure 6.7.: Twenty five measured landmark pair-distances for the 6-DOF sensor as RCS. Measurement of precision (see Fig: 6.5).

In addition to the tracker a 6-DOF sensor was used as RCS. Thus, the location of the landmarks is reported relative to the position of the sensor. The test object and the sensor should be rigidly coupled together, otherwise it could produce large random errors. Fig. 6.7 depicts the results of two setups where the sensor is used as RCS. In both setups there is considerable variation on the measured distances. A mean standard deviation of 0.90 mm & 0.70 mm, and range of the error of 0.89 mm & 0.72 mm for first and second setup respectively.

Table 6.5.: Test phantom: statistical metrics of the error for measured distances, based on the principle described in sec. 6.2.1.

RCS	$Mean_E$ (mm)	$s.d._E$ (mm)	Min_E (mm)	Max_E (mm)	$Q1_E$ (mm)	$Median_E$ (mm)	$Q3_E$ (mm)	IQR_E (mm)	Low_E (mm)	Up_E (mm)	$95\%CI_E$ (mm)
Tracker_1	0.04	0.06	0.00	0.24	0.01	0.01	0.04	0.04	-0.04	0.10	0.01
Tracker_2	0.12	0.07	0.01	0.26	0.07	0.11	0.16	0.10	-0.08	0.31	0.02
6-DOF_1	0.90	0.21	0.37	1.27	0.76	0.91	1.04	0.28	0.34	1.46	0.05
6-DOF_2	0.72	0.17	0.39	1.12	0.60	070	0.82	0.21	0.28	1.14	0.04

Accuracy comparison between techniques

The error of the measured distances was calculated for each landmark pair [e.g. for landmark pair 1_2 we measure 25 distances (see Fig. 6.5), therefore one measure of standard deviation for landmark pair 1_2], that gives us 28 error values for one setup. Then, as a measure of accuracy for each setup the distribution of the error was evaluated. The results for all techniques, i.e. tracker as RCS, 6-DOF sensor as RCS, and the results from VM are shown in Tab. 6.5. Tracker as reference shows the best precision and the lowest variability of the error. The highest value of the error, 1.27 mm, is found in the setup where the sensor is used as RCS. Overall, a distribution of the error for each setup shows that when using the tracker as RCS the precision is higher, depicted in Fig. 6.8.

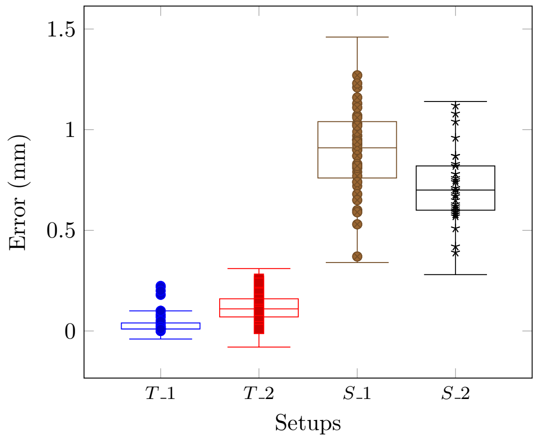

Figure 6.8.: Test Phantom: distribution of the error for the measured landmark distances for each setup: T_1 & T_2 (Tracker as RCS), S_1 & S_2 (6-DOF sensor as RCS).

6.2.2. 3D-Compounding Accuracy

Volume compounding of the tracked US images for ICE and TEE probes, using reconstruction algorithms, was carried on and the results were published in *Kreher et al.* [82]. The results show that EM tracking is able to report the distances in sub-millimetre range. The volume reconstruction with the tracked ICE catheter showed poor results, with six corners out of eight could be identified, and five distances out of nine could be calculated.

6.3. Experiment 3: Unknown Geometry Object

As an unknown geometry object is used the 3D-printed heart. In experiment one the distances are well known and can be easily measured. In contrary, the results here will be shown as a measure of precision more than than measure of accuracy.

Tracker as RCS

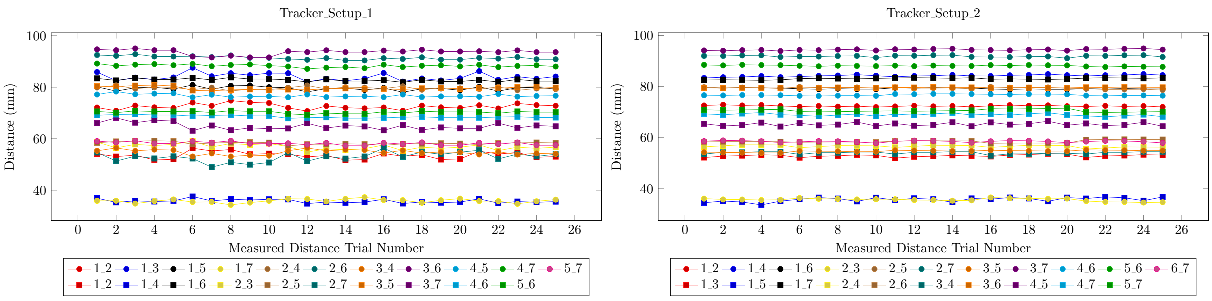

Figure 6.9.: Twenty five measured landmark pair-distances for the tracker as RCS. Measurement of precision (see Fig: 6.5).

There are two setups where the tracker is used as RCS. While recording, the phantom is rigidly fixed to the FG. The landmarks were pointed with the stylus from first to seventh in increasing order and the coordinates are recorded from the Aurora tracking system. The process was repeated five times. The average over five runs was calculated, and finally distances between all landmarks were obtained. A Python code was used for the calculations in order to avoid human error. Tab. B.1 comprises the distances between all landmarks using the mean over the five runs for each landmark. From the above figure we can see that setup_2 offers a lower variability of the measured distances for all pairs of landmarks. A straight line means a low variability on measured distances (high precision), and an oscillating line means a high variability (low precision). Thus, setup_2 offers e better precision in comparison to setup_1.

6-DOF sensor as RCS

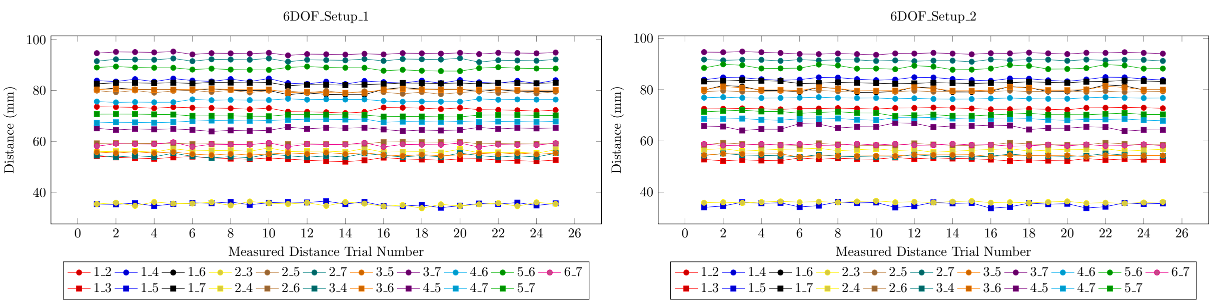

Figure 6.10.: Twenty five measured landmark pair-distances for the 6-DOF sensor as RCS. Measurement of precision (see Fig: 6.5).

In contrast to the technique where the tracker serves as RCS, now that the 6-DOF sensor servers as RCS the coordinates of the landmarks are reported relative to the sensor. Since the sensor is attached rigidly to the box where the heart model is fixed (see Fig. 4.15), the random error is expected to be reduced. Two experiments are conducted with the 6-DOF sensor as RCS, depicted in Fig. 6.10. From the graphs we can see that the behaviour is relatively similar with no big difference in the variability of the measured distances between landmark pairs.

Virtual Model

Measurements from the virtual model were taken also. Following the same pattern as per other setups, sets of five measurements for each landmark were taken. As expected, there is a low variability on the measured distances, which means high precision. Landmark pair-distances 2_3 and 2_5 show the highest variability.

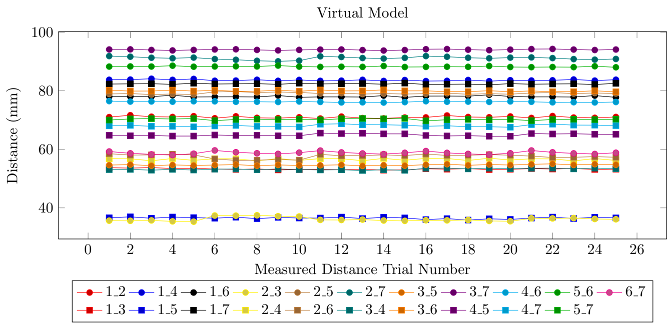

Figure 6.11.: Twenty five measured landmark pair-distances for the VM. Measurement of precision (see Fig: 6.5).

Accuracy comparison between techniques

Moreover, for each distance between landmarks we found the error (standard deviation), that gives us 21 error values (one for each landmark distance) for one setup. Then, as a measure of accuracy for each setup the error of the error was evaluated. The results for all techniques, i.e. tracker as RCS, 6-DOF sensor as RCS, and the results from VM are shown in Tab. 6.6. Tracker as reference shows the poorest precision and the highest instability. The highest value and the lowest value of the error is found in the setups where tracker is used as RCS, respectively 1.74 mm and 0.09 mm. However, a distribution of the

Table 6.6.: Mean error, standard deviation, minimum error , maximum error, first quartile, second quartile, third quartile, interquartile range , lower whisker, upper whisker, 95% confidence interval.

RCS	$Mean_E$ (mm)	$s.d._E$ (mm)	Min_E (mm)	Max_E (mm)	$Q1_E$ (mm)	$Median_E$ (mm)	$Q3_E$ (mm)	IQR_E (mm)	Low_E (mm)	Up_E (mm)	$95\%CI_E$ (mm)
Tracker_1	0.82	0.34	0.41	1.74	0.53	0.69	1.02	0.49	-0.21	1.76	0.10
Tracker_2	0.38	0.15	0.09	0.80	0.29	0.35	0.47	0.18	0.01	0.75	0.04
6-DOF_1	0.50	0.13	0.30	0.79	0.44	0.49	0.57	0.13	0.24	0.76	0.04
6-DOF_2	0.45	0.22	0.16	0.92	0.29	0.38	0.57	0.28	-0.14	1.00	0.06
VM	0.31	0.16	0.14	0.76	0.19	0.27	0.35	0.16	-0.04	0.58	0.04

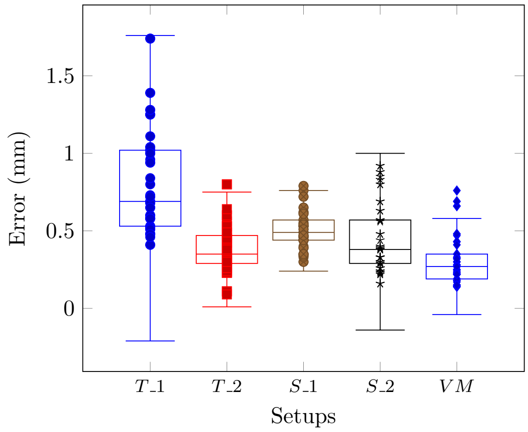

Figure 6.12.: Distribution of the error of the heart measured landmark distances for each setup: T_1 & T_2 (Tracker as RCS), S_1 & S_2 (6-DOF sensor as RCS), virtual model (VM) (distances measured manually from the virtual model).

error for each setup shows that when using 6-DOF as reference the precision is higher and closer to the VM measurement, depicted in Fig. 6.5.

6.4. Experiment 4: Effect of Intracardiac Echocardiography Transducers on the Accuracy of EMTS

The results described on this section do not belong to the description of the "Experiment 4" in 5.4. The planned experiment could not take place, however, results according to the effect of the ultrasound transducers on th accuracy of electromagnetic sensors were published in *Kreher et al.* [82]. The conducted experiment consist on testing TEE and ICE probes for the influence on the tracking accuracy of 5-DOF and 6-DOF sensors. The results show a difference on the location of the sensor of 0.045 ± 0.024 mm for the 6-DOF sensor and 0.041 ± 0.111 for the 5-DOF sensor, when TEE probe is active. For ICE probe the error was 0.045 ± 0.031 and 0.018 ± 0.026 for the 6-DOF and 5-DOF sensors respectively.

6.5. Experiment 5: Heart Model Registration

Registration via fCal

The registration process of the heart is similar to the calibration process of the calibration phantom, see Sec. 4.1.3. The coordinates of the landmarks are obtained from the virtual model of the heart, which showed to have the best precision among other setups.

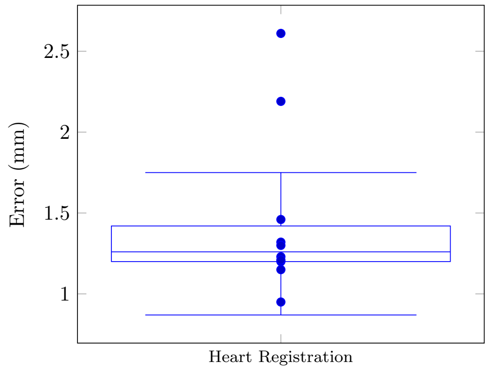

Figure 6.13.: Heart registration error reported from fCal.

The registration process is achieved with a mean error of 1.46 mm and standard deviation of the error 0.49 mm. That shows a good calibration process, compared to the mean calibration error value for calibration phantom of 1.19 mm. Fig. 6.13 depicts the distribution of the registration error as a box plot. Except two outliers, 2.19 mm and 2.61 mm, all registration errors for ten trials remain lower than 1.75 mm. The corresponding values for the box plot are; lower whisker 0.87 mm, Q1 (first quartile) 1.20 mm, median 1.26 mm, Q3 (third quartile) 1.42 mm, upper whisker 1.75 mm, and $IQR(Q3 - Q1)$ 0.22 mm. Lower whisker is calculated as $Q1 - 1.5IQR$ and upper whisker $Q3 + 1.5IQR$.

Table 6.7.: Error of the heart registration for ten trials (Trial error), mean value (Mean), standard deviation (s.d.), minimum (Min.), and maximum (Max.) values.

	Trial Error (mm)													
ReferenceFrame	1	2	3	4	5	6	7	8	9	10	Mean (mm)	s.d. (mm)	Min. (mm)	Max. (mm)
6-DOF	2.19	1.15	2.61	0.95	1.32	1.20	1.46	1.23	1.30	1.21	1.46	0.49	0.95	2.61

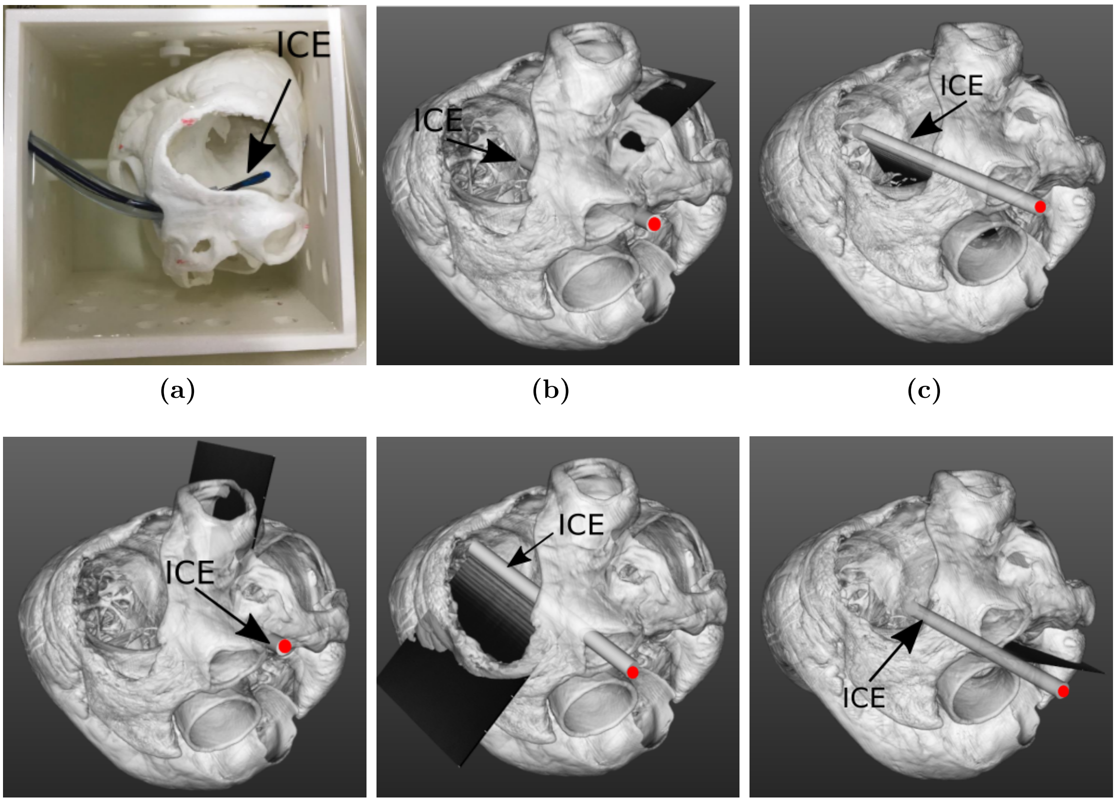

(a) (b) (c)

(d) (e) (f)

Figure 6.14.: US image and tip of the catheter visualization within the volume of the heart in different angles in fCal. **(a)** Real life scenario, catheter inserted inside the heart through superior vena cava.

Ultrasound image visualization

The visualization of the US image and the ICE catheter is depicted in Fig. 6.14. The content of the US image is not representative, because it was not possible to attach the AcuNav catheter to the US machine which was available. However, the orientation of the image gives e realistic feeling of the location and the orientation of the ICE catheter. While manoeuvring the catheter, the visual aid proved to be helpful for choosing the desired spatial orientation of the ICE catheter within the volume of the heart. Nevertheless, it was noticeable that the location of the catheter's shaft was not always realistic to the location on the real-life setup.

7. Discussion

The goal of this thesis was to implement and evaluate electromagnetic tracking for intracardiac echocardiography probes using PLUS toolkit; additionally, to incorporate the tracked ultrasound images into the publicly available software for the live visualization of the position and orientation of the US slice in 3D space. Moreover, the accuracy of the 2X5DOF coupled sensors for ICE catheter tracking should be investigated further, together with the accuracy of the visualized US image in 3D space. The results in the previous chapter (Ch. 6) have shown that the calibration of the system can be achieved with a relatively low error. The position and orientation of tracked tools, i.e. stylus, calibration phantom, probe, can be visualized on real-time. The toolkit supports instant transfer of the acquired data through OpenIGTLink, or alternatively to save them in a file (MHA, NRRD) for a later use. The tracked images can be reconstructed to create a volume out of the tracked slices.

The discussion of the results is given related to the calibration of the system, followed by a discussion of the results about tracking echocardiography probes, and concluded by a discussion about the visualized ultrasound image.

7.1. Calibration of Electromagnetic Tracking System

This work was started with the calibration of the system. The stylus is offered by the manufacturer with a calibrated tip, however, we conducted the stylus calibration for reproducibility of the work. A novel calibration was designed with additional features: a defined position of the reference sensor in the phantom body, triangular holes for better positioning of the fiducial wires, and support for calibration of the tubular probes like ICE catheters [82]. Phantom registration was achieved with a mean error of 1.19 mm over ten trials, which remains within the range suggested from PLUS toolkit specifications (0.8 - 1.5mm).

Temporal calibration indicated that it produces large errors for increasing imaging depth. For imaging depths of 2, 4, 6, and 8 cm the time offset remains in the range of 130 - 200 ms, while for 10 cm imaging depth the offset ranges from 154 to 350 ms. For higher imaging depth it was not possible to conclude the calibration. That suits to the imaging proprieties of ICE catheter.

Probe calibration proved to be most challenging. We realized that tracking the probe with a single 5-DOF sensor does not provide sufficient accuracy, due to lacking angular information along one of the axes. The 6-DOF sensor proved to be significantly better in terms of tracking information, however, there was an angular offset in the z-axis direction between the visualized image and the position of the transducer. It is not clear if that is due to calibration inaccuracies or wrong rendering of the image. The calibration process was conducted with L742 linear array, ICE, and TEE probes. We were expecting linear array probe to perform better in comparison to the other two. The results indicate a similar behaviour between TEE ICE probes; with the latter having a lower standard deviation.

7.2. Electromagnetic Tracking of Echocardiography Probes

Additionally to ICE catheter we tracked a Z6M TEE probe. We investigated the behaviour between using the tracker and a 6-DOF sensor as RCS. Furthermore, the influence of the probe in the accuracy of the electromagnetic tracking system was evaluated, and how well the tracked US images suit to 3D compounding.

Reference coordinate system

We used two methods; tracker as RCS, and a 6-DOF as RCS. In Sec. 6.2 and Sec.6.3 are shown results for test (cubic) phantom and printed heart (heart phantom) respectively. Fig. 7.1 depicts the error distribution as box plot for cube and heart phantom. When using the tracker as RCS; results indicate a lower mean error value for the cube phantom setup ($mean_{TC1} = 0.04$, $mean_{TC2} = 0.12$), and higher mean error value for heart phantom setup ($mean_{TH1}$=0.82, $mean_{TH2}$=0.38). When using the sensor as RCS the behaviour is the opposite; a lower mean error value for the heart setup ($mean_{SH3} = 0.50$, $mean_{SH4} = 0.45$), and higher mean error value for the cube phantom setup ($mean_{SC3} = 0.90$, $mean_{SC4} = 0.72$). That looks contradictory at first, nevertheless, there is a simple reason behind; the tracker behaved better for the cube phantom because it was easier to fix the cube phantom rigidly relative to the FG. Furthermore, when using the sensor as RCS the 6-DOF sensor was fixed rigidly on the side of the box, as depicted in Fig. 5.8b.

Influence of ICE probe on the accuracy of electromagnetic tracking

The published results from *Kreher et al.* showed a non-significant decrease in accuracy of the electromagnetic sensors in proximity to TEE and ICE probes. However, the distortions to the electromagnetic sensors coming from ultrasound probes vary greatly from electromagnetic technology, probe technology, and proby type (2D/ 3D) [34].

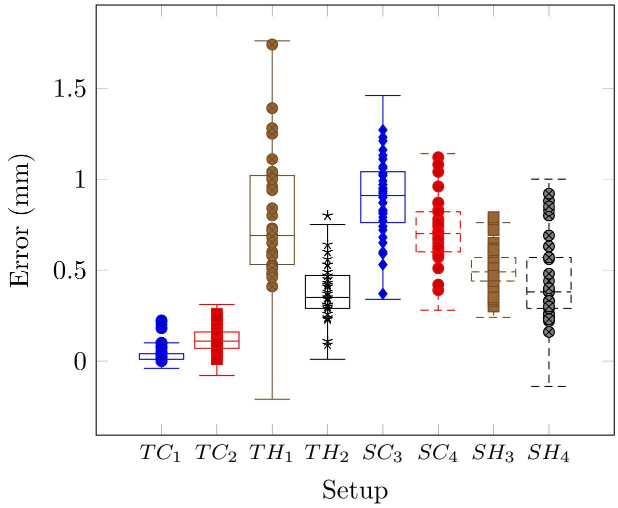

Figure 7.1.: Box plot for the measured landmark distances error: TC_1, TC_2, SC_3, SC_4; tracker (two setups) and sensor (two setups) as RCS for the cube phantom. TH_1, TH_2, SH_3, SH_4; tracker (two setups) and sensor (two setups) as RCS for the heart phantom.

Three dimensional compounding

Three dimensional compounding outputted not satisfactory results. TEE performed slightly better than ICE probe, which could be due to the 6-DOF sensor used to track TEE (ICE was tracked with 2X5-DOF sensors). An other reason could be the type of sweeping during the scan. This area need to be investigated further whether Plus toolkit is adequate for volume reconstruction of data produced from echocardiography probes, in terms of image quality and field of view. The publication from *Kreher et al.* provides more information about volume reconstruction with tracked echocardiography probes [82].

7.3. Visualization of Live Ultrasound Image

Visualization of the live US image is the ultimate goal of this work. It was possible to visualize the position and orientation of the probe and US image on real-time, depicted on Fig. 7.2. The visualization looks realistic and corresponds to the real life scenario. 7.2a shows the floating ultrasound image within the test phantom volume, and 7.2b.

With the current configuration it is not possible to test the position and orientation of the US image. Especially for the irregular geometry (heart phantom) its it becomes even more difficult to evaluate if the visualization is accurate. From the above figure it can be seen that the position and orientation of the US image for the linear array probe is relatively accurate, and it gives a lot of information about the origin of the US image:

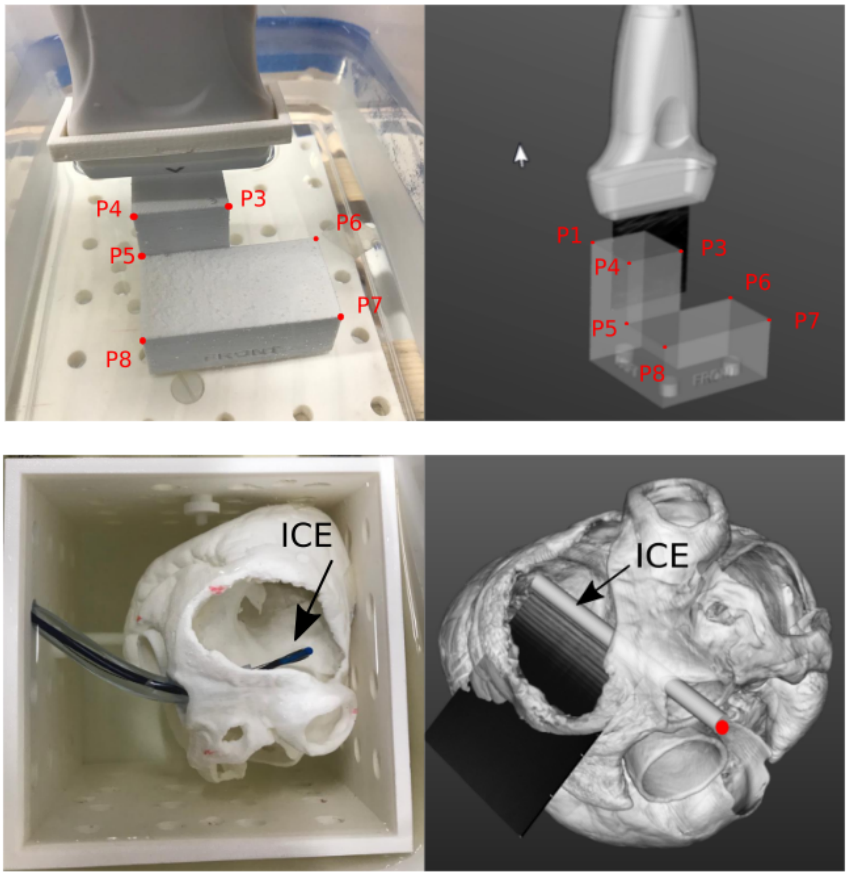

Figure 7.2.: **(a)** left - L742 linear array probe scanning test phantom, right - the visualisation scene from fCal, **(b)** left - ICE catheter advanced into the heart through superior vena cave, right - visualization in fCal.

8. Conclusion and Future Work

It can be concluded that implementation of tracking intracardiac echocardiography transducers for visualizing the position and orientation of the US image was successful. The configuration of the tracking system and the evaluation of the tracking accuracy of the EMTS in presence and proximity of echocardiography probes enables a foundation for future research of the topic.

The calibration of the tracking system was achieved with relatively good accuracy. The calibration of the linear array probe was successful and with good accuracy. Intracardiac echocardiography probe showed promising results regarding the calibration accuracy, however, the spatial relation of the transducer's tip with the center of coordinate system of the attached sensors remains to be improved.

Three dimensional compounding with the ICE probe proved to be insufficiently accurate for volume reconstruction. That could also be attributed to poorly defined of the spatial relation between ICE transducer and the center of the sensor's coordinate system.

There was not significant influence on the tracking accuracy of the electromagnetic sensors from ICE and TEE/ 2D probes. However, considering the poor three dimensional compounding of the tracked ultrasound images, this should be treated carefully and analysed further.

Bibliography

[1] M R M Jongbloed, M J Schalij, K Zeppenfeld, P V Oemrawsingh, E E van der Wall, and J J Bax. Clinical applications of intracardiac echocardiography in interventional procedures. *Heart*, 91(7):981–990, 2005.

[2] Maria L Narducci, Nicola Vitulano, Vincenzo Pazzano, and Gemma Pelargonio. Technology update: intracardiac echocardiography - a review of the literature. *Medical Devices: Evidence and Research*, page 231, may 2015.

[3] Stéphane Cotin, S Dawson, D Meglan, David Shaffer, M Ferrell, Ryan Bardsley, F Morgan, T Nagano, J Nikom, P Sherman, M Walterman, and Jeffrey Wendlandt. Icts, an interventional cardiology training system. *Studies in health technology and informatics*, 70:59–65, 02 2000.

[4] D. Kane, W. Grassi, R. Sturrock, and P. V. Balint. A brief history of musculoskeletal ultrasound: 'From bats and ships to babies and hips'. *Rheumatology*, 43(7):931–933, Jun 2004.

[5] Andras Lasso, Tamas Heffter, Adam Rankin, Csaba Pinter, Tamas Ungi, and Gabor Fichtinger. PLUS: Open-source toolkit for ultrasound-guided intervention systems. *IEEE Transactions on Biomedical Engineering*, 61(10):2527–2537, oct 2014.

[6] GTAI: *Germany Trade and Invest*. Medical technology, October 2019. `https://www.gtai.de/gtai-en/invest/industries/life-sciences/medical-technology`.

[7] Gabriel Flemming. Medical technology clusters in germany. *GTAI*, 2020.

[8] Thomas L. Szabo. *Diagnostic Ultrasound Imaging: Inside Out*. Elsevier, Boston, MA, USA, 2 edition, 2014.

[9] Peter R. Hoskins, Kevin Martin, and Abigail Thrush, editors. *Diagnostic Ultrasound: Physics and Equipment*. Cambridge University Press, 2 edition, 2010.

[10] Peter R Hoskins, Kevin Martin, and Abigail Thrush, editors. *Diagnostic Ultrasound: Physics and Equipment*. CRC Press, 3 edition, apr 2019.

[11] K. Kirk Shung. *Diagnostic Ultrasound*. CRC Press, sep 2006.

[12] R. Van Tiggelen and E. Pouders. Ultrasound and computed tomography: Spin-offs of the world wars. *JBR–BTR*, 83, 2003.

[13] Toshio Wagai†. Studies on the foundation and development of diagnostic ultrasound.

Proceedings of the Japan Academy, Series B, 83(8):256–265, 2007.

[14] Aladin Carovac, Fahrudin Smajlovic, and Dzelaludin Junuzovic. Application of ultrasound in medicine. *Acta Informatica Medica*, 19(3):168–171, 2011.

[15] Peter R. Hoskins, Kevin Martin, and Abigail Thrush. *Diagnostic Ultrasound: Physics and Equipment*, page 1–3. Cambridge University Press, 2 edition, 2010.

[16] Petros Nihoyannopoulos and Joseph Kisslo, editors. *Echocardiography*. Springer International Publishing, 2018.

[17] Sachin B. Malik, Natalie Chen, Rex A. Parker III, and Joe Y. Hsu. Transthoracic echocardiography: Pitfalls and limitations as delineated at cardiac ct and mr imaging. *RadioGraphics*, 37(2):383–406, feb 2017.

[18] Luk Cox and Idoya Lahortiga. somersault18:24, February 2020. `https://www.somersault1824.com/science-illustrations/`.

[19] Douglas C. Shook. Transesophageal echocardiography. pages 62–65. J Ultrason, 2019.

[20] Pooja D. Thakrar, Bryan D. Petersen, and John A. Kaufman. Intravascular ultrasound for transvenous interventions. *Techniques in Vascular and Interventional Radiology*, 16(3):161–167, sep 2013.

[21] Andres Enriquez, Luis C. Saenz, Raphael Rosso, Frank E. Silvestry, David Callans, Francis E. Marchlinski, and Fermin Garcia. Use of intracardiac echocardiography in interventional cardiology. *Circulation*, 137(21):2278–2294, may 2018.

[22] Mohamad Alkhouli, Ziyad M. Hijazi, David R. Holmes, Charanjit S. Rihal, and Susan E. Wiegers. Intracardiac echocardiography in structural heart disease interventions. *JACC: Cardiovascular Interventions*, 11(21):2133–2147, nov 2018.

[23] Ziyad M. Hijazi and Hussam Suradi. Intracardiac echocardiography-guided interventions. *JACC: Cardiovascular Interventions*, 7(9):1045–1047, 2014.

[24] Johann B Hummel, Michael R. Bax, Michael L. Figl, Yan Kang, Calvin Maurer, Wolfgang W. Birkfellner, Helmar Bergmann, and Ramin Shahidi. Design and application of an assessment protocol for electromagnetic tracking systems. *Medical Physics*, 32(7Part1):2371–2379, jun 2005.

[25] Alfred M. Franz, Tamas Haidegger, Wolfgang Birkfellner, Kevin Cleary, Terry M. Peters, and Lena Maier-Hein. Electromagnetic tracking in medicine—a review of technology, validation, and applications. *IEEE Transactions on Medical Imaging*, 33(8):1702–1725, aug 2014.

[26] Janusz Skowronek. Current status of brachytherapy in cancer treatment – short overview. *Journal of Contemporary Brachytherapy*, 9(6):581–589, 2017.

[27] T. Langø, G. A. Tangen, R. Mårvik, B. Ystgaard, Y. Yavuz, J. H. Kaspersen, O. V. Solberg, and T. A.N. Hernes. Navigation in laparoscopy - Prototype research platform for improved image-guided surgery. *Minimally Invasive Therapy and Allied Technologies*, 17(1):17–33, 2008.

[28] Bradford J. Wood, Hui Zhang, Amir Durrani, Neil Glossop, Sohan Ranjan, David Lindisch, Eliott Levy, Filip Banovac, Joern Borgert, Sascha Krueger, Jochen Kruecker, Anand Viswanathan, and Kevin Cleary. Navigation with electromagnetic tracking for interventional radiology procedures: A feasibility study. *Journal of Vascular and Interventional Radiology*, 16(4):493–505, 2005.

[29] Liat Appelbaum, Jacob Sosna, Yizhak Nissenbaum, Alexander Benshtein, and S. Nahum Goldberg. Electromagnetic navigation system for CT-guided biopsy of small lesions. *American Journal of Roentgenology*, 196(5):1194–1200, 2011.

[30] Stephen B. Solomon, Carolyn Magee, David E. Acker, and Anthony C. Venbrux. TIPS placement in swine, guided by electromagnetic real-time needle tip localization displayed on previously acquired 3-D CT. *CardioVascular and Interventional Radiology*, 22(5):411–414, 1999.

[31] Stephen B. Solomon, Timm Dickfeld, and Hugh Calkins. Real-time cardiac catheter navigation on three-dimensional CT images. *Journal of Interventional Cardiac Electrophysiology*, 8(1):27–36, 2003.

[32] A. De Lambert, S. Esneault, A. Lucas, P. Haigron, Ph Cinquin, and J. L. Magne. Electromagnetic tracking for registration and navigation in endovascular aneurysm repair: A phantom study. *European Journal of Vascular and Endovascular Surgery*, 43(6):684–689, 2012.

[33] Alfred Franz, Keno März, Alexander Seitel, Hannes Kenngott, Martin Wagner, A Preukschas, Hans-Peter Meinzer, Ivo Wolf, and Lena Maier-Hein. Combined modality for ultrasound imaging and electromagnetic tracking. *Biomedizinische Technik. Biomedical engineering*, 58, 09 2013.

[34] Mark Hastenteufel, Marcus Vetter, Hans-Peter Meinzer, and Ivo Wolf. Effect of 3d ultrasound probes on the accuracy of electromagnetic tracking systems. *Ultrasound in Medicine & Biology*, 32(9):1359–1368, sep 2006.

[35] Nora T. Tgavalekos, Peter Traneus Anderson, Dun Alex Li, and Jonathan David Schiff. System and method for tracking an ultrasound catheter, May 7 2009. US Patent 2009/0118620 A1.

[36] S. Condino, V. Ferrari, C. Freschi, A. Alberti, R. Berchiolli, F. Mosca, and M. Ferrari. Electromagnetic navigation platform for endovascular surgery: how to develop sensorized catheters and guidewires. *The International Journal of Medical Robotics*

and Computer Assisted Surgery, 8(3):300–310, feb 2012.

[37] S. Condino, E.M. Calabrò, A. Alberti, S. Parrini, R. Cioni, R.N. Berchiolli, M. Gesi, V. Ferrari, and M. Ferrari. Simultaneous tracking of catheters and guidewires: Comparison to standard fluoroscopic guidance for arterial cannulation. *European Journal of Vascular and Endovascular Surgery*, 47(1):53–60, jan 2014.

[38] N. Rosche and W. Stehr. Evaluation of a magnetic tracking and electrocardiogram-based tip confirmation system for peripherally inserted central catheters in pediatric patients. *Journal of Infusion Nursing*, 41(5):301–308, 2018. Cited By :3.

[39] D.N. Stephens, J. Cannata, Ruibin Liu, Jian Zhong Zhao, K.K. Shung, Hien Nguyen, R. Chia, A. Dentinger, D. Wildes, K.E. Thomenius, A. Mahajan, K. Shivkumar, Kang Kim, M. O'Donnell, A. Nikoozadeh, O. Oralkan, P.T. Khuri-Yakub, and D.J. Sahn. Multifunctional catheters combining intracardiac ultrasound imaging and electrophysiology sensing. *IEEE Transactions on Ultrasonics, Ferroelectrics and Frequency Control*, 55(7):1570–1581, jul 2008.

[40] N. Malliet, J. G. Andrade, P. Khairy, H. K. Nguyen Thanh, S. Venier, M. Dubuc, K. Dyrda, P. Guerra, B. Mondésert, L. Rivard, R. Tadros, M. Talajic, B. Thibault, D. Roy, and L. Macle. Impact of a novel catheter tracking system on radiation exposure during the procedural phases of atrial fibrillation and flutter ablation. *PACE - Pacing and Clinical Electrophysiology*, 38(7):784–790, 2015. Cited By :15.

[41] S. Kircher, S. Rolf, G. Hindricks, and P. Sommer. Ablation of typical atrial flutter using a novel non-fluoroscopic electromagnetic catheter tracking system. *Interventional Cardiology (London)*, 6(2):149–158, 2014. Cited By :2.

[42] G. Hindricks. Catheter ablation of atrial fibrillation using a new non-fluoroscopic sensor-guided 3d navigation tool. *journal of arrhythmia*, 27(4):257, 2011.

[43] L. Sacolick, N. Patel, J. Tang, E. Levy, and K. Cleary. Electromagnetically tracked placement of a peripherally inserted central catheter. In *Proceedings of SPIE - The International Society for Optical Engineering*, volume 5367, pages 724–728, 2004. Cited By :4.

[44] Claire Jones, Stephen A. Badger, Christopher S. Boyd, and Chee V. Soong. The impact of radiation dose exposure during endovascular aneurysm repair on patient safety. *Journal of Vascular Surgery*, 52(2):298–302, aug 2010.

[45] Stewart R. Walsh, Tjun Tang, Michael E. Gaunt, and Jonathan R. Boyle. Contrast-induced nephropathy. *Journal of Endovascular Therapy*, 14(1):92–100, feb 2007.

[46] Paul M. Loschak, Laura J. Brattain, and Robert D. Howe. Automated pointing of cardiac imaging catheters. In *2013 IEEE International Conference on Robotics and Automation*. IEEE, may 2013.

[47] Laura J. Brattain, Paul M. Loschak, Cory M. Tschabrunn, Elad Anter, and Robert D. Howe. Instrument tracking and visualization for ultrasound catheter guided procedures. In *Augmented Environments for Computer-Assisted Interventions*, pages 41–50. Springer International Publishing, 2014.

[48] Liu Da, Dapeng Zhang, and Tianmiao Wang. Overview of the vascular interventional robot. *The International Journal of Medical Robotics and Computer Assisted Surgery*, 4(4):289–294, sep 2008.

[49] Cai Meng, Jun Zhang, Da Liu, Bo Liu, and Fugen Zhou. A remote-controlled vascular interventional robot: system structure and image guidance. *The International Journal of Medical Robotics and Computer Assisted Surgery*, 9(2):230–239, mar 2013.

[50] Adeline Schwein, Benjamin Kramer, Ponraj Chinnadurai, Neha Virmani, Sean Walker, Marcia O'Malley, Alan B. Lumsden, and Jean Bismuth. Electromagnetic tracking of flexible robotic catheters enables "assisted navigation" and brings automation to endovascular navigation in an in vitro study. *Journal of Vascular Surgery*, 67(4):1274–1281, apr 2018.

[51] Jun Zhou, Evelyn Sebastian, Victor Mangona, and Di Yan. Real-time catheter tracking for high-dose-rate prostate brachytherapy using an electromagnetic 3d-guidance device: A preliminary performance study. *Medical Physics*, 40(2):021716, jan 2013.

[52] Natasja N. Y. Janssen, Harry Brastianos, Aquila Akingbade, Tim Olding, Thomas Vaughan, Tamas Ungi, Andras Lasso, Chandra Joshi, Martin Korzeniowski, Conrad Falkson, and Gabor Fichtinger. Electromagnetic (EM) catheter path tracking in ultrasound-guided brachytherapy of the breast. *International Journal of Computer Assisted Radiology and Surgery*, 15(10):1645–1652, jul 2020.

[53] Elodie Lugez, Hossein Sadjadi, Chandra P. Joshi, Selim G. Akl, and Gabor Fichtinger. Improved electromagnetic tracking for catheter path reconstruction with application in high-dose-rate brachytherapy. *International Journal of Computer Assisted Radiology and Surgery*, 12(4):681–689, feb 2017.

[54] Thomas A. Vaughan, Harry Brastianos, Tamas Ungi, Andras Lasso, Conrad Falkson, and Gabor Fichtinger. Needle navigation and catheter reconstruction for breast brachytherapy using open source software. *Acta Polytechnica Hungarica*, 16(8), sep 2019.

[55] Tamas Ungi, Gabrielle Gauvin, Andras Lasso, Caitlin T. Yeo, Padina Pezeshki, Thomas Vaughan, Kaci Carter, John Rudan, C. Jay Engel, and Gabor Fichtinger. Navigated breast tumor excision using electromagnetically tracked ultrasound and surgical instruments. *IEEE Transactions on Biomedical Engineering*, 63(3):600–606, mar 2016.

[56] Po-Wei Hsu, Richard W. Prager, Andrew H. Gee, and Graham M. Treece. Freehand 3d ultrasound calibration: A review. In *Advanced Imaging in Biology and Medicine*, pages 47–84. Springer Berlin Heidelberg, 2007.

[57] R.W. Prager, R.N. Rohling, A.H. Gee, and L. Berman. Rapid calibration for 3-d freehand ultrasound. *Ultrasound in Medicine & Biology*, 24(6):855–869, jul 1998.

[58] Po-Wei Hsu, Graham M. Treece, Richard W. Prager, Neil E. Houghton, and Andrew H. Gee. Comparison of freehand 3-d ultrasound calibration techniques using a stylus. *Ultrasound in Medicine & Biology*, 34(10):1610–1621, oct 2008.

[59] Paul R. Detmer, Gerard Bashein, Timothy Hodges, Kirk W. Beach, Eric P. Filer, David H. Burns, and D.Eugene Strandness. 3d ultrasonic image feature localization based on magnetic scanhead tracking: In vitro calibration and validation. *Ultrasound in Medicine & Biology*, 20(9):923–936, jan 1994.

[60] C.D. Barry, C.P. Allott, Nigel John, P.M. Mellor, P.A. Arundel, D.S. Thomson, and John Waterton. Three-dimensional freehand ultrasound: Image reconstruction and volume analysis. *Ultrasound in medicine & biology*, 23:1209–24, 02 1997.

[61] Q.H. Huang, Y.P. Zheng, M.H. Lu, and Z.R. Chi. Development of a portable 3d ultrasound imaging system for musculoskeletal tissues. *Ultrasonics*, 43(3):153–163, jan 2005.

[62] A. Krupa. Automatic calibration of a robotized 3d ultrasound imaging system by visual servoing. In *Proceedings 2006 IEEE International Conference on Robotics and Automation, 2006. ICRA 2006.* IEEE, 2006.

[63] Andrei State, David Chen, Chris Tector, Andrew Brandt, Hong Chen, Ryutarou Ohbuchi, Michael Bajura, and Henry Fuchs. Case study: Observing a volume rendered fetus within a pregnant patient. volume 18, pages 364–368, 01 1994.

[64] D.C. Barratt, G.P. Penney, C.S.K. Chan, M. Slomczykowski, T.J. Carter, P.J. Edwards, and D.J. Hawkes. Self-calibrating 3d-ultrasound-based bone registration for minimally invasive orthopedic surgery. *IEEE Transactions on Medical Imaging*, 25(3):312–323, mar 2006.

[65] Olivier Péria, Laurent Chevalier, Anne François-Joubert, Jean-Pierre Caravel, Sylvie Dalsoglio, Stéphane Lavallée, and Philippe Cinquin. Using a 3d position sensor for registration of SPECT and US images of the kidney. In *Lecture Notes in Computer Science*, pages 23–29. Springer-Verlag, 1995.

[66] Alexander Hartov, Symma D. Eisner, W. Roberts, Keith D. Paulsen, Leah A. Platenik, and Michael I. Miga and. Error analysis for a free-hand three-dimensional ultrasound system for neuronavigation. *Neurosurgical Focus*, 6(3):E7, mar 1999.

[67] Devin V. Amin, Takeo Kanade, Branislav Jaramaz, Anthony M. DiGioia, Con-

stantinos Nikou, Richard S. LaBarca, and James E. Moody. Calibration method for determining the physical location of the ultrasound image plane. In *Medical Image Computing and Computer-Assisted Intervention – MICCAI 2001*, pages 940–947. Springer Berlin Heidelberg, 2001.

[68] Anand Viswanathan, Emad M. Boctor, Russell H. Taylor, Gregory Hager, and Gabor Fichtinger. Immediate ultrasound calibration with three poses and minimal image processing. In *Medical Image Computing and Computer-Assisted Intervention – MICCAI 2004*, pages 446–454. Springer Berlin Heidelberg, 2004.

[69] Diane M. Muratore and Robert L. Galloway. Beam calibration without a phantom for creating a 3-d freehand ultrasound system. *Ultrasound in Medicine & Biology*, 27(11):1557–1566, nov 2001.

[70] Jonathan Carr. *Surface reconstruction in 3D medical imaging*. PhD thesis, University of Canterbury. Electrical Engineering, 1996.

[71] Thomas Langø. *Ultrasound Guided Surgery: Image Processing and Navigation*. PhD thesis, Fakultet for informasjonsteknologi og elektroteknikk (Uspesifisert), 2000.

[72] J Varandas, P Baptista, J Santos, R Martins, and J Dias. VOLUS—a visualization system for 3d ultrasound data. *Ultrasonics*, 42(1-9):689–694, apr 2004.

[73] Aziah Ali and Rajasvaran Logeswaran. A visual probe localization and calibration system for cost-effective computer-aided 3d ultrasound. *Computers in Biology and Medicine*, 37(8):1141–1147, aug 2007.

[74] Emad M. Boctor, Ameet Jain, Michael A. Choti, Russell H. Taylor, and Gabor Fichtinger. Rapid calibration method for registration and 3d tracking of ultrasound images using spatial localizer. In William F. Walker and Michael F. Insana, editors, *Medical Imaging 2003: Ultrasonic Imaging and Signal Processing*. SPIE, may 2003.

[75] Y. Sato, M. Nakamoto, Y. Tamaki, T. Sasama, I. Sakita, Y. Nakajima, M. Monden, and S. Tamura. Image guidance of breast cancer surgery using 3-d ultrasound images and augmented reality visualization. *IEEE Transactions on Medical Imaging*, 17(5):681–693, 1998.

[76] Roch M. Comeau, Aaron Fenster, and Terence M. Peters. Integrated MR and ultrasound imaging for improved image guidance in neurosurgery. In Kenneth M. Hanson, editor, *Medical Imaging 1998: Image Processing*. SPIE, jun 1998.

[77] Roch M. Comeau, Abbas F. Sadikot, Aaron Fenster, and Terry M. Peters. Intraoperative ultrasound for guidance and tissue shift correction in image-guided neurosurgery. *Medical Physics*, 27(4):787–800, apr 2000.

[78] Niko Pagoulatos, David R. Haynor, and Yongmin Kim. A fast calibration method for 3-d tracking of ultrasound images using a spatial localizer. *Ultrasound in Medicine*

& Biology, 27(9):1219–1229, sep 2001.

[79] Frank Lindseth, Jon Bang, and Thomas Langø. A robust and automatic method for evaluating accuracy in 3-d ultrasound-based navigation. *Ultrasound in Medicine & Biology*, 29(10):1439–1452, oct 2003.

[80] Frank Lindseth, Geir Arne Tangen, Thomas Langø, and Jon Bang. Probe calibration for freehand 3-d ultrasound. *Ultrasound in Medicine & Biology*, 29(11):1607–1623, nov 2003.

[81] Po-Wei Hsu, Richard W. Prager, Andrew H. Gee, and Graham M. Treece. Real-time freehand 3d ultrasound calibration. In Stanislav Y. Emelianov and Stephen A. McAleavey, editors, *Medical Imaging 2007: Ultrasonic Imaging and Signal Processing*. SPIE, mar 2007.

[82] Robert Kreher, Thomas Groscheck, Kristjan Qarri, Bernhard Preim, Alexander Schmeisser, Thomas Rauwolf, Rüdiger Christian Braun-Dullaeus, and Sandy Engelhardt. A novel calibration phantom for combining echocardiography with electromagnetic tracking. *Current Directions in Biomedical Engineering*, 6(1), sep 2020.

[83] Andrew H. Gee, Neil E. Houghton, Graham M. Treece, and Richard W. Prager. A mechanical instrument for 3D ultrasound probe calibration. *Ultrasound in Medicine & Biology*, 31(4):505–518, apr 2005.

[84] J. M. Blackall, D. Rueckert, C. R. Maurer, G. P. Penney, D. L. G. Hill, and D. J. Hawkes. An image registration approach to automated calibration for freehand 3d ultrasound. In *Medical Image Computing and Computer-Assisted Intervention – MICCAI 2000*, pages 462–471. Springer Berlin Heidelberg, 2000.

[85] Oskar Škrinjar. Point-based registration with known correspondence: Closed form optimal solutions and properties. In *Biomedical Image Registration*, pages 315–321. Springer Berlin Heidelberg, 2006.

[86] Jay B. West and J. Michael Fitzpatrick. Point-based rigid registration: clinical validation of theory. In Kenneth M. Hanson, editor, *Medical Imaging 2000: Image Processing*, volume 3979, pages 353 – 359. International Society for Optics and Photonics, SPIE, 2000.

[87] Jay B. West, J. Michael Fitzpatrick, Steven A. Toms, Jr. Maurer, Calvin R., and Robert J. Maciunas. Fiducial Point Placement and the Accuracy of Point-based, Rigid Body Registration. *Neurosurgery*, 48(4):810–817, 04 2001.

[88] Nestor Andres Parra. *Rigid and Non-rigid Point-based Medical Image Registration*. PhD thesis, FIU Electronic Theses and Dissertations, 2009.

[89] C.R. Maurer, J.M. Fitzpatrick, M.Y. Wang, R.L. Galloway, R.J. Maciunas, and G.S.

Allen. Registration of head volume images using implantable fiducial markers. *IEEE Transactions on Medical Imaging*, 16(4):447–462, 1997.

[90] Hao Zhu, Bin Guo, Ke Zou, Yongfu Li, Ka-Veng Yuen, Lyudmila Mihaylova, and Henry Leung. A review of point set registration: From pairwise registration to groupwise registration. *Sensors*, 19(5):1191, mar 2019.

[91] Yu Zhang and Yong Wang. Method and apparatus for real time spatial compound imaging, April 17 2012. US Patent 8,157,737.

[92] D.F. Leotta and R.W. Martin. Three-dimensional spatial compounding of ultrasound scans with incidence angle weighting. In *1999 IEEE Ultrasonics Symposium. Proceedings. International Symposium (Cat. No.99CH37027)*. IEEE.

[93] P. Soler, O. Gerard, P. Allain, E. Saloux, E. Angelini, and I. Bloch. Comparison of fusion techniques for 3d + t echocardiography acquisitions from different acoustic windows. In *Computers in Cardiology, 2005*. IEEE, 2005.

[94] Kashif Rajpoot, J. Alison Noble, Vicente Grau, Cezary Szmigielski, and Harald Becher. Multiview RT3d echocardiography image fusion. In *Functional Imaging and Modeling of the Heart*, pages 134–143. Springer Berlin Heidelberg, 2009.

[95] Cheng Yao, John Simpson, Tobias Schaeffter, and Graeme Penney. Multi-view 3d echocardiography compounding based on feature consistency. *Physics in medicine and biology*, 56:6109–28, 09 2011.

[96] Vicente Grau, Harald Becher, and J. Alison Noble. Registration of multiview real-time 3-d echocardiographic sequences. *IEEE Transactions on Medical Imaging*, 26(9):1154–1165, sep 2007.

[97] H. Hu, C. Ye, X. Wang, and N. Xu. Multi-angle spatial compound imaging in ultrasonic immersion testing using a single transducer. *Journal of Instrumentation*, 13(07):P07004–P07004, jul 2018.

[98] Patrick Carnahan, John T. Moore, Daniel Bainbridge, Elvis C. S. Chen, and Terry M. Peters. Multi-view 3d echocardiography volume compounding for mitral valve procedure planning. In Baowei Fei and Cristian A. Linte, editors, *Medical Imaging 2020: Image-Guided Procedures, Robotic Interventions, and Modeling*. SPIE, mar 2020.

[99] Patrick Carnahan, John T. Moore, Daniel Bainbridge, Gavin Wheeler, Shujie Deng, Kuberan Pushparajah, Elvis C. S. Chen, John M. Simpson, and Terry M. Peters. Applications of VR medical image visualization to chordal length measurements for cardiac procedures. In Baowei Fei and Cristian A. Linte, editors, *Medical Imaging 2020: Image-Guided Procedures, Robotic Interventions, and Modeling*. SPIE, mar 2020.

[100] Jochen F Krücker, Charles R Meyer, Gerald L LeCarpentier, J.Brian Fowlkes, and Paul L Carson. 3d spatial compounding of ultrasound images using image-based nonrigid registration. *Ultrasound in Medicine & Biology*, 26(9):1475–1488, nov 2000.

[101] J.F. Krucker, G.L. LeCarpentier, J.B. Fowlkes, and P.L. Carson. Rapid elastic image registration for 3-d ultrasound. *IEEE Transactions on Medical Imaging*, 21(11):1384–1394, nov 2002.

[102] Stefan R. Kirsch. Accuracy assessment of the electromagnetic tracking system aurora. *NDI Europe Gmbh*, October 2005.

[103] Junichi Tokuda, Gregory S. Fischer, Xenophon Papademetris, Ziv Yaniv, Luis Ibanez, Patrick Cheng, Haiying Liu, Jack Blevins, Jumpei Arata, Alexandra J. Golby, Tina Kapur, Steve Pieper, Everette C. Burdette, Gabor Fichtinger, Clare M. Tempany, and Nobuhiko Hata. OpenIGTLink: an open network protocol for image-guided therapy environment. *The International Journal of Medical Robotics and Computer Assisted Surgery*, 5(4):423–434, dec 2009.

[104] Tamas Ungi, Andras Lasso, and Gabor Fichtinger. Open-source platforms for navigated image-guided interventions. *Medical Image Analysis*, 33:181–186, oct 2016.

[105] ISO (the International Organization for Standardization). Guide to the calibration of test equipment, 2013.

[106] Andriy Fedorov, Reinhard Beichel, Jayashree Kalpathy-Cramer, Julien Finet, Jean-Christophe Fillion-Robin, Sonia Pujol, Christian Bauer, Dominique Jennings, Fiona Fennessy, Milan Sonka, John Buatti, Stephen Aylward, James V. Miller, Steve Pieper, and Ron Kikinis. 3d slicer as an image computing platform for the quantitative imaging network. *Magnetic Resonance Imaging*, 30(9):1323–1341, nov 2012.

[107] Laura J. Brattain, Paul M. Loschak, Cory M. Tschabrunn, Elad Anter, and Robert D. Howe. Instrument tracking and visualization for ultrasound catheter guided procedures. In *Augmented Environments for Computer-Assisted Interventions*, pages 41–50. Springer International Publishing, 2014.

[108] J. Ashburner and K.J. Friston. Spatial transformation of images. In R.S.J. Frackowiak, K.J. Friston, C. Frith, R. Dolan, and J.C. Mazziotta, editors, *Human Brain Function*, pages 43–58. Academic Press USA, 1997.

[109] Euan Ashley and Josef Niebauer, editors. *Cardiology Explained.* Remedica, 2004.

[110] Ultrasound schools info. History of ultrasound, January 2009. `https://www.ultrasoundschoolsinfo.com/history/`.

[111] J Hummel, M Figl, W Birkfellner, M R Bax, R Shahidi, C R Maurer, and H Bergmann. Evaluation of a new electromagnetic tracking system using a standardized assessment protocol. *Physics in Medicine and Biology*, 51(10):N205–N210, apr 2006.

A. Calibration Metrics and Figures

A.1. Calibration Graphs and Figures

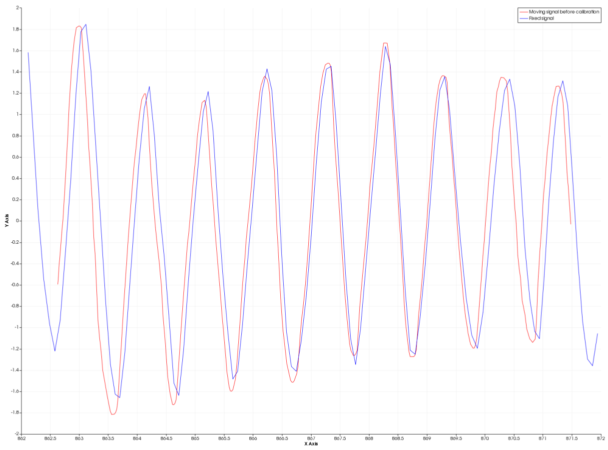

Figure A.1.: Offset between tracked data stream and video data stream before calibration.

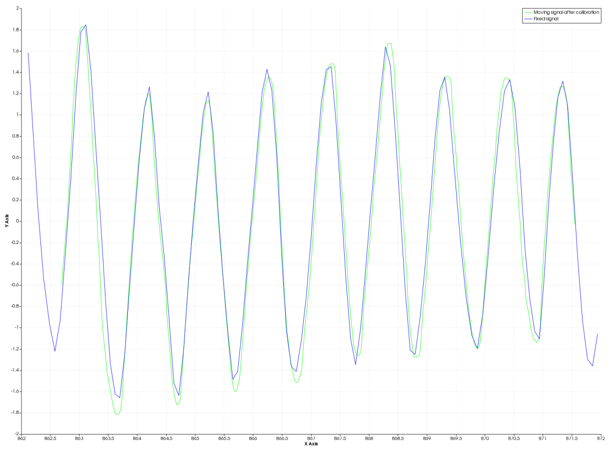

Figure A.2.: Offset between tracked data stream and video data stream after calibration.

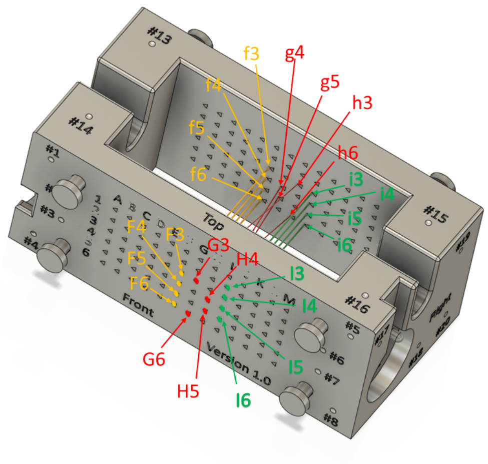

Figure A.3.: Novel Calibration phantom with coordinates of the fiducial wires. Different colors are used for easier annotation.

```xml
<Geometry>
    <!-- Pattern for Calibration Phantom-->
    <Pattern Type="NWire">
        <Wire Name="7:F3_f3" EndPointFront="25.0 0.0 15.0" EndPointBack="25.0 40.0 15.0" />
        <Wire Name="8:G3_h3" EndPointFront="30.0 0.0 15.0" EndPointBack="35.0 40.0 15.0" />
        <Wire Name="9:I3_i3" EndPointFront="40.0 0.0 15.0" EndPointBack="40.0 40.0 15.0" />
    </Pattern>
    <Pattern Type="NWire">
        <Wire Name="7:F4_f4" EndPointFront="25.0 0.0 10.0" EndPointBack="25.0 40.0 10.0" />
        <Wire Name="8:H4_g4" EndPointFront="35.0 0.0 10.0" EndPointBack="30.0 40.0 10.0" />
        <Wire Name="9:I4_i4" EndPointFront="40.0 0.0 10.0" EndPointBack="40.0 40.0 10.0" />
    </Pattern>
    <Pattern Type="NWire">
        <Wire Name="7:F5_f5" EndPointFront="25.0 0.0 5.0" EndPointBack="25.0 40.0 5.0" />
        <Wire Name="8:H5_g5" EndPointFront="35.0 0.0 5.0" EndPointBack="30.0 40.0 5.0" />
        <Wire Name="9:I5_i5" EndPointFront="40.0 0.0 5.0" EndPointBack="40.0 40.0 5.0" />
    </Pattern>
    <Pattern Type="NWire">
        <Wire Name="7:F6_f6" EndPointFront="25.0 0.0 0.0" EndPointBack="25.0 40.0 0.0" />
        <Wire Name="8:G6_h6" EndPointFront="30.0 0.0 0.0" EndPointBack="35.0 40.0 0.0" />
        <Wire Name="9:I6_i6" EndPointFront="40.0 0.0 0.0" EndPointBack="40.0 40.0 0.0" />
    </Pattern>
```

Figure A.4.: Pattern of the fiducial lines in the configuration file.

```xml
<Landmarks>
    <!-- Front -->
    <Landmark Name="#1"  Position="-22.5   -9.5   30.0" />
    <!--<Landmark Name="#2"  Position="-15.0   -9.5  17.5" />
    <Landmark Name="#3"  Position="-15.0   -9.5   7.5" />
    <Landmark Name="#4"  Position="-22.5   -9.5   -5.0" />
    <Landmark Name="#5"  Position=" 82.5   -9.5   30.0" />
    <Landmark Name="#6"  Position=" 75.0   -9.5  17.5" />
    <Landmark Name="#7"  Position=" 75.0   -9.5   7.5" />-->
    <Landmark Name="#8"  Position=" 82.5   -9.5   -5.0" />
    <!-- Left -->
    <Landmark Name="#9"  Position="-29.5  40.0   27.5" />
    <!--<Landmark Name="#10" Position="-29.5  42.5   -5.0" />
    <Landmark Name="#11" Position="-29.5   0.0   27.5"  /> -->
    <Landmark Name="#12" Position="-29.5  22.5   -5.0" />
    <!-- Top -->
    <Landmark Name="#13" Position="-20.0  40.0   37.0" />
    <!--<Landmark Name="#14" Position="-20.0   5.0   37.0" />
    <Landmark Name="#15" Position=" 80.0  35.0   37.0" />-->
    <Landmark Name="#16" Position=" 80.0   0.0   37.0" />
    <!-- Right -->
    <Landmark Name="#17" Position=" 89.5   -5.0  27.5" />
    <!--<Landmark Name="#18" Position=" 89.5  25.0  -2.5" />
    <Landmark Name="#19" Position=" 89.5  40.0  27.5" />-->
    <Landmark Name="#20" Position=" 89.5  40.0  -2.5 " />
    <!-- Back -->
    <Landmark Name="#21" Position=" 82.5  49.5   30.0" />
    <!--<Landmark Name="#22" Position=" 75.0  49.5  17.5" />
    <Landmark Name="#23" Position=" 75.0  49.5  7.5" />
    <Landmark Name="#24" Position=" 82.5  49.5   -5.0" />
    <Landmark Name="#25" Position="-22.5  49.5  30.0" />
    <Landmark Name="#26" Position="-15.0  49.5  17.5" />
    <Landmark Name="#27" Position="-15.0  49.5   7.5" />-->
    <Landmark Name="#28" Position="-22.5  49.5   -5.0" />
</Landmarks>
```

Figure A.5.: Landmark coordinates of the calibration phantom in the configuration file.

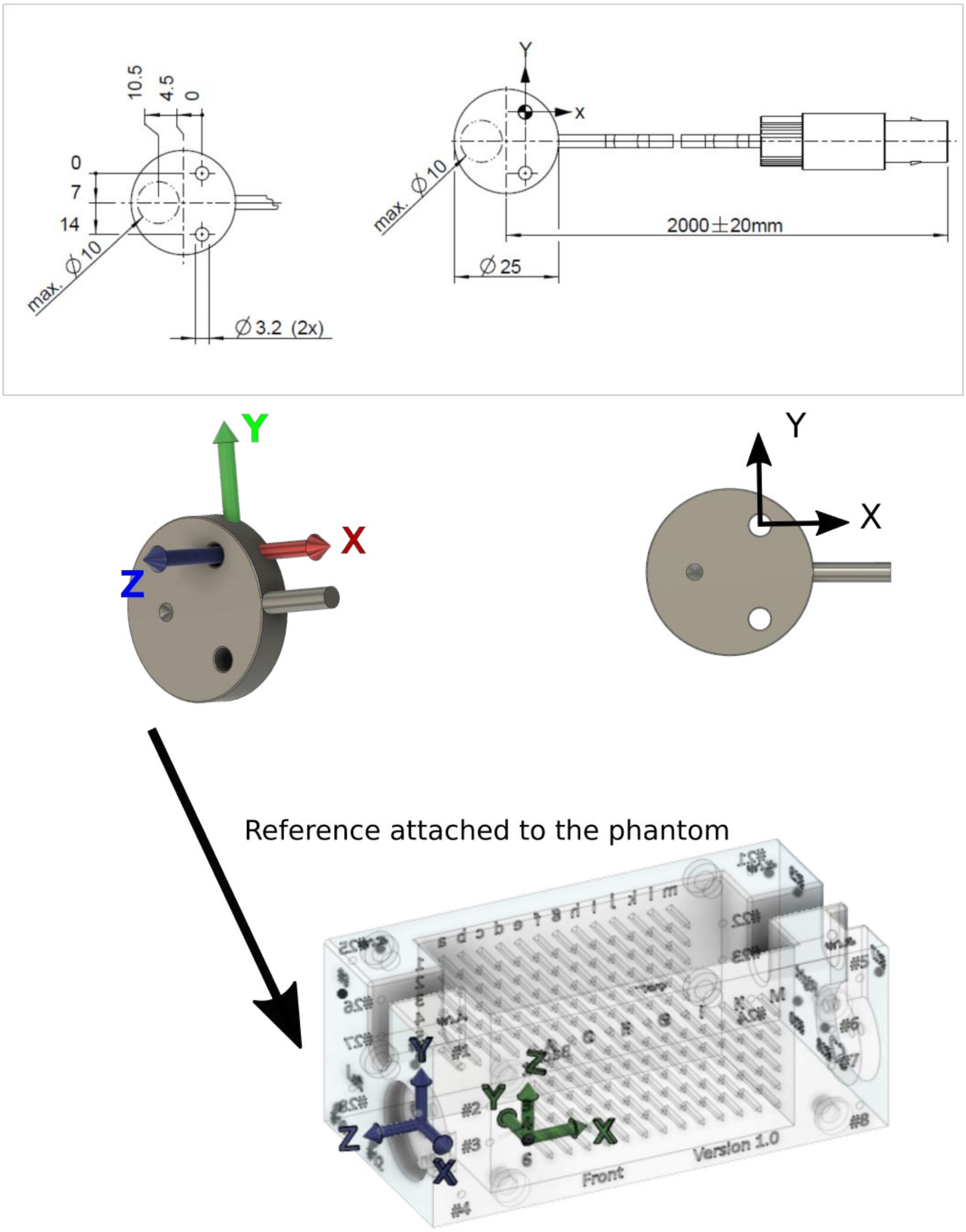

Figure A.6.: Reference sensor axis directions

A.2. Configuration File

```
<PlusConfiguration version="2.1" PlusRevision="Plus-2.6.0.
    ce2dc94c - Win64">
  <DataCollection StartupDelaySec="1">
```

```
    <DeviceSet Name="fCal: Calibrated Probe using (Stylus + fCal Phantom + L742 US Probe)_SPV1_ECG" Description="Replays a recorded sequence of imaging the bottom of a water tank. Image and tracking data is provided by separate devices." />
    <!--Aurora Tracker-->
    <Device
      Id="TrackerDevice"
      Type="AuroraTracker"
      SerialPort="5"
      LocalTimeOffsetSec="0.0569698"
      BaudRate="0"
      MeasurementVolumeNumber="0">
      <DataSources>
        <DataSource Type="Tool" Id="Reference" PortName="0" BufferSize="150"/>
        </DataSource>
        <DataSource Type="Tool" Id="Stylus" PortName="1" BufferSize="150"/>
        <DataSource Type="Tool" Id="Probe" PortName="2" BufferSize="150"/>
        </DataSource>
      </DataSources>
      <OutputChannels>
        <OutputChannel Id="TrackerStream">
          <DataSource Id="Reference" />
          <DataSource Id="Stylus" />
          <DataSource Id="Probe" />
        </OutputChannel>
      </OutputChannels>
    </Device>
    <!--Frambrabber-->
    <Device
      Id="VideoDevice"
      Type="MmfVideo"
      FrameSize="1368 768"
      VideoFormat="YUY2"
      CaptureDeviceId="0"
      AcquisitionRate="60">
```

```
      <DataSources>
        <DataSource
          Type="Video"
          Id="Video"
          PortUsImageOrientation="UF"
          ImageType="BRIGHTNESS"
          ClipRectangleOrigin="311 29 0"
          ClipRectangleSize="674 530 1"
          BufferSize="150" />
      </DataSources>
      <OutputChannels>
        <OutputChannel Id="VideoStream" VideoDataSourceId="Video" />
      </OutputChannels>
    </Device>
    <!--ECG with USB (Bautrate USB: 115200, RS232: 9600)-->
    <Device
      Id="SerialDevice"
      Type="GenericSerialDevice"
      AcquisitionRate="100"
      SerialPort="3"
      BaudRate="115200"
      MaximumReplyDelaySec="10"
      MaximumReplyDurationSec="30">
      <DataSources>
        <DataSource Id="SerialData" Type="FieldData" />
      </DataSources>
      <OutputChannels>
        <OutputChannel Id="FieldChannel">
          <DataSource Id="SerialData" />
        </OutputChannel>
      </OutputChannels>
    <!-- Mixer -->
    </Device>
    <Device Id="TrackedVideoDevice" Type="VirtualMixer">
      <InputChannels>
        <InputChannel Id="VideoStream" />
        <InputChannel Id="TrackerStream" />
      </InputChannels>
```

```
      <OutputChannels>
        <OutputChannel Id="TrackedVideoStream" />
      </OutputChannels>
    </Device>
    <!-- Data capture for storage-->
    <Device
      Id="TrackedVideoCap"
      Type="VirtualCapture"
      EnableFileCompression="FALSE"
      EnableCaptureOnStart="FALSE"
      RequestedFrameRate="60">
      <InputChannels>
        <InputChannel Id="TrackedVideoStream" />
      </InputChannels>
    </Device>
    <!-- Data capture for storage-->
    <Device
      Id="EcgCap"
      Type="VirtualCapture"
      EnableFileCompression="FALSE"
      EnableCaptureOnStart="FALSE"
      RequestedFrameRate="60">
      <InputChannels>
        <InputChannel Id="FieldChannel" />
      </InputChannels>
    </Device>
    <!-- Volume reconstruction device-->
    <Device
      Id="VolumeReconstructorDevice"
      Type="VirtualVolumeReconstructor"
      OutputVolDeviceName="RecVol_Reference"
      EnableReconstruction="FALSE"
      ImageCoordinateFrame="Image"
      ReferenceCoordinateFrame="Reference">
      <InputChannels>
        <InputChannel Id="TrackedVideoStream" />
      </InputChannels>
      <VolumeReconstruction
      ImageCoordinateFrame="Image"
```

```
      ReferenceCoordinateFrame="Reference"
      OutputSpacing="1 1 1"
      ClipRectangleOrigin="-1 -1"
      ClipRectangleSize="-1 -1"
      FanAnglesDeg="-51 51"
      FanOriginPixel="342 0"
      FanRadiusStartPixel="20"
      FanRadiusStopPixel="530"
      Interpolation="NEAREST_NEIGHBOR"
      Optimization="FULL"
      CompoundingMode="LATEST"
      FillHoles="OFF"
      NumberOfThreads="1" />
    </Device>
  </DataCollection>

  <!-- OpenIhtLink-->
  <PlusOpenIGTLinkServer MaxNumberOfIgtlMessagesToSend="1"
     MaxTimeSpentWithProcessingMs="50" ListeningPort="18944"
     SendValidTransformsOnly="true" OutputChannelId="
     TrackedVideoStream" >
    <DefaultClientInfo>
      <MessageTypes>
        <Message Type="IMAGE" />
        <Message Type="TRANSFORM" />
      </MessageTypes>
      <ImageNames>
        <Image Name="Image" EmbeddedTransformToFrame="
           Reference" />
      </ImageNames>
      <TransformNames>
        <Transform Name="ProbeToReference" />
      </TransformNames>
    </DefaultClientInfo>
  </PlusOpenIGTLinkServer>

  <CoordinateDefinitions>
    <Transform From="Image" To="Probe"
      Matrix="
```

```
        -0.0415197  -0.0108441  -0.0646728  21.8842
        -0.0609096  0.00114308  0.0463284   3.34098
        -0.0152433  0.0841377   -0.00896475 1.90352
        0   0   0   1"
      Error="2.04098" Date="091819_190802" />
    <Transform From="Image" To="TransducerOriginPixel"
      Matrix="
        1   0   0   -410
        0   1   0   5
        0   0   1   0
        0   0   0   1"
      Date="2011.12.06 17:57:00" />
    <Transform From="Phantom" To="Reference"
      Matrix="
        0   -1  0   0
        0   0   1   -14
        -1  0   0   -25
        0   0   0   1"
      Date="082219_123643" />
    <Transform From="StylusTip" To="Stylus"
      Matrix="
        1   0   0   0
        0   1   0   0
        0   0   1   0
        0   0   0   1"
      Date="2019.09.04 23:39:22" />
    <Transform From="TransducerOriginPixel" To="TransducerOrigin"
      Matrix="
        0.0724492   0   0   0
        0   0.0872662   0   0
        0   0   0.0800578   0
        0   0   0   1"
      Date="091819_190802" />
  </CoordinateDefinitions>
  <Rendering WorldCoordinateFrame="Reference" DisplayedImageOrientation="MFA">
    <DisplayableObject Type="Model" ObjectCoordinateFrame="Reference" Id="Volume" />
```

```
    <DisplayableObject Type="Image" ObjectCoordinateFrame="
       Image" Id="LiveImage" />
    <DisplayableObject Type="Model" ObjectCoordinateFrame="
       Stylus" Id="StylusModel" File="Stylus_Example.stl" />
    <DisplayableObject
      Type="Model"
      ObjectCoordinateFrame="Phantom"
      Id="PhantomModel"
      File="fCal_ICE.stl"
      Opacity="0.4"
      ModelToObjectTransform="
        1   0   0   -30
        0   1   0   -10
        0   0   1   -12.5
        0   0   0   1" />
    <DisplayableObject
      Type="Model"
      ObjectCoordinateFrame="TransducerOrigin"
      Id="ProbeModel"
      File="Probe_L14-5_38.stl"
      Opacity="0.6"
      ModelToObjectTransform="
        -1  0   0   29.7
        0   -1  0   1.5
        0   0   1   -14
        0   0   0   1" />
  </Rendering>
  <Segmentation
    ApproximateSpacingMmPerPixel="0.078"
    MorphologicalOpeningCircleRadiusMm="0.17"
    MorphologicalOpeningBarSizeMm="2"
    ClipRectangleOrigin="30 40"
    ClipRectangleSize="396 367"
    MaxLinePairDistanceErrorPercent="10"
    AngleToleranceDegrees="10"
    MaxAngleDifferenceDegrees="10"
    MinThetaDegrees="-70"
    MaxThetaDegrees="70"
    MaxLineShiftMm="10"
```

```
    ThresholdImagePercent="10"
    CollinearPointsMaxDistanceFromLineMm="0.6"
    UseOriginalImageIntensityForDotIntensityScore="0" />
  <PhantomDefinition>
    <Description Name="fCAL" Type="Multi-N" Version="2.0"
       WiringVersion="2.0" Institution="Phantom for NDI
       Aurora Reference Sensor" />
    <Geometry>
      <Pattern Type="NWire">
        <Wire Name="7:F3_f3" EndPointFront="25.0 0.0 15.0"
           EndPointBack="25.0 40.0 15.0" />
        <Wire Name="8:G3_h3" EndPointFront="30.0 0.0 15.0"
           EndPointBack="35.0 40.0 15.0" />
        <Wire Name="9:I3_i3" EndPointFront="40.0 0.0 15.0"
           EndPointBack="40.0 40.0 15.0" />
      </Pattern>
      <Pattern Type="NWire">
        <Wire Name="7:F4_f4" EndPointFront="25.0 0.0 10.0"
           EndPointBack="25.0 40.0 10.0" />
        <Wire Name="8:H4_g4" EndPointFront="35.0 0.0 10.0"
           EndPointBack="30.0 40.0 10.0" />
        <Wire Name="9:I4_i4" EndPointFront="40.0 0.0 10.0"
           EndPointBack="40.0 40.0 10.0" />
      </Pattern>
      <Pattern Type="NWire">
        <Wire Name="7:F5_f5" EndPointFront="25.0 0.0 5.0"
           EndPointBack="25.0 40.0 5.0" />
        <Wire Name="8:H5_g5" EndPointFront="35.0 0.0 5.0"
           EndPointBack="30.0 40.0 5.0" />
        <Wire Name="9:I5_i5" EndPointFront="40.0 0.0 5.0"
           EndPointBack="40.0 40.0 5.0" />
      </Pattern>
      <Pattern Type="NWire">
        <Wire Name="7:F6_f6" EndPointFront="25.0 0.0 0.0"
           EndPointBack="25.0 40.0 0.0" />
        <Wire Name="8:G6_h6" EndPointFront="30.0 0.0 0.0"
           EndPointBack="35.0 40.0 0.0" />
        <Wire Name="9:I6_i6" EndPointFront="40.0 0.0 0.0"
           EndPointBack="40.0 40.0 0.0" />
```

```
        </Pattern>
        <Landmarks>
          <Landmark Name="#1" Position="-22.5   -9.5   30.0" />
          <Landmark Name="#8" Position=" 82.5   -9.5   -5.0" />
          <Landmark Name="#9" Position="-29.5  40.0   27.5" />
          <Landmark Name="#12" Position="-29.5  22.5   -5.0" />
          <Landmark Name="#13" Position="-20.0  40.0   37.0" />
          <Landmark Name="#16" Position=" 80.0   0.0   37.0" />
          <Landmark Name="#17" Position=" 89.5   -5.0  27.5" />
          <Landmark Name="#20" Position=" 89.5  40.0  -2.5 " />
          <Landmark Name="#21" Position=" 82.5  49.5   30.0" />
          <Landmark Name="#28" Position="-22.5  49.5   -5.0" />
        </Landmarks>
      </Geometry>
    </PhantomDefinition>
    <fCal
      PhantomModelId="PhantomModel"
      ReconstructedVolumeId="Volume"
      TransducerModelId="ProbeModel"
      StylusModelId="StylusModel"
      ImageDisplayableObjectId="LiveImage"
      NumberOfCalibrationImagesToAcquire="200"
      NumberOfValidationImagesToAcquire="200"
      NumberOfStylusCalibrationPointsToAcquire="200"
      RecordingIntervalMs="100"
      MaxTimeSpentWithProcessingMs="70"
      ImageCoordinateFrame="Image"
      ProbeCoordinateFrame="Probe"
      ReferenceCoordinateFrame="Reference"
      TransducerOriginCoordinateFrame="TransducerOrigin"
      TransducerOriginPixelCoordinateFrame="
         TransducerOriginPixel"
      TemporalCalibrationDurationSec="10"
      FixedChannelId="VideoStream"
      FixedSourceId="Video"
      MovingChannelId="TrackerStream"
      MovingSourceId="ProbeToTracker"
      DefaultSelectedChannelId="TrackedVideoStream"
      FreeHandStartupDelaySec="3" />
```

```
    <vtkPlusPivotCalibrationAlgo ObjectMarkerCoordinateFrame="Stylus" ReferenceCoordinateFrame="Reference" ObjectPivotPointCoordinateFrame="StylusTip" />
    <vtkPlusPhantomLandmarkRegistrationAlgo PhantomCoordinateFrame="Phantom" ReferenceCoordinateFrame="Reference" StylusTipCoordinateFrame="StylusTip" DetectionTimeSec="2.0" StylusTipMaximumDisplacementThresholdMm="1" />
    <vtkPhantomLinearObjectRegistrationAlgo PhantomCoordinateFrame="Phantom" ReferenceCoordinateFrame="Reference" StylusTipCoordinateFrame="StylusTip" />
    <vtkTemporalCalibrationAlgo ClipRectangleOrigin="-1 -1" ClipRectangleSize="-1 -1" SetMaximumMovingLagSec="0.5" />
    <vtkPlusProbeCalibrationAlgo ImageCoordinateFrame="Image" ProbeCoordinateFrame="Probe" PhantomCoordinateFrame="Phantom" ReferenceCoordinateFrame="Reference" />
</PlusConfiguration>
```

A.3. Calibration Metrics

Table A.1.: Temporal calibration offset values at 2, 4, 6, 8, 10 cm imaging depth over 10 trials.

	Imaging Depth (cm)				
Trial	2	4	6	8	10
1	165	174	193	187	203
2	166	174	167	200	295
3	130	173	173	190	331
4	154	182	162	190	332
5	155	167	162	189	303
6	154	167	162	192	327
7	173	179	190	183	336
8	164	179	173	186	335
9	161	175	163	182	336
10	165	174	163	185	350

Table A.2.: Coordinate systems used in fCal (dimensions are in mm) [5].

Reference frame name	Origin	Axes directions
Tracker	Origin of the tracking system	As defined by the tracking system manufacturer
Stylus	Origin of the marker attached to the Stylus tool	Defined by the tracking system / marker manufacturer
StylusTip	Tip of the stylus tool	X axis: aligned with the Stylus coordinate system's X axis Y axis: chosen to be the cross product of the Z and X axes Z axis: the axis that points from the Stylus coordinate system origin towards StylusTip coordinate system origin
Reference	Origin of the marker that is attached to the calibration phantom	Defined by the manufacturer (Fig. A.6)
Phantom	Novel Calibration Phantom [82]: inner side of A6 hole	X axis: from column A to B direction Y axis: towards the back side of the phantom Z axis: from row 6 to row 1 direction see Fig. A.6
Probe	Origin of the marker attached to the probe	Defined by the manufacturer of the marker
Image	Position of the pixel that is in the origin of the MF oriented image	X axis: towards the marked side of the transducer Y axis: towards the direction that points away (far) from the transducer Z axis: cross product of X and Y
Transducer	Center of the transducer crystal array	X axis: towards the marked side of the transducer Y axis: towards the direction that points away (far) from the transducer Z axis: cross product of X and Y
TransducerOrigin	Position of the pixel that is in the middle of the first line of the MF oriented image. In PLUS it's only used for approximate visualization of the transducer 3D model	X axis: towards the marked side of the transducer Y axis: towards the direction that points away (far) from the transducer Z axis: cross product of X and Y
TransducerOriginPixel	Position of the pixel that is in the middle of the first line of the MF oriented image. In PLUS it's only used for approximate visualization of the transducer 3D model	X axis: towards the marked side of the transducer Y axis: towards the direction that points away (far) from the transducer Z axis: cross product of X and Y

B. Metrics from Experiments

B.1. Landmark Distances

B.1.1. Heart Data

Table B.1.: Distances in millimeter between seven landmarks of the heart model. First four rows with tracker as reference coordinate system, fifth and sixth with 6-DOF sensor as reference system, last two rows from the VM using Autodesk Fusion 360 and 3D Slicer.

Distances	Tracker as Reference 1	Tracker as Reference 2	Tracker as Reference 3	Tracker as Reference 4	6-DOF setup 1	6-DOF setup 2	VM Fusion 360	VM 3D Slicer
1-2	87.01	71.74	72.51	72.38	72.63	72.66	70.98	70.19
1-3	52.17	53.45	53.54	52.90	53.04	52.79	53.27	53.28
1-4	84.91	85.98	84.02	84.23	83.54	84.17	83.61	83.86
1-5	36.55	36.57	35.76	35.74	35.40	35.15	36.51	37.07
1-6	70.42	70.62	79.52	79.22	79.89	80.11	78.05	77.44
1-7	43.04	43.43	82.78	83.07	82.74	82.92	82.35	81.06
2-3	36.85	35.25	35.80	35.68	35.34	36.11	36.11	34.88
2-4	52.25	53.74	56.89	56.62	56.15	56.51	56.56	55.47
2-5	77.72	77.95	79.61	79.41	79.82	79.37	79.12	78.55
2-6	75.36	46.99	58.24	58.49	59.19	58.62	57.61	57.70
2-7	81.51	59.81	91.40	91.88	91.99	91.47	91.12	90.27
3-4	53.72	52.91	52.93	54.06	54.29	54.25	53.21	52.61
3-5	53.71	53.39	54.74	54.71	55.12	54.38	54.66	54.78
3-6	57.88	56.81	79.56	79.57	80.11	80.22	79.94	79.10
3-7	54.06	53.71	93.60	94.42	94.56	94.21	94.03	92.71
4-5	66.54	67.24	64.89	65.22	64.78	65.39	64.92	65.47
4-6	36.19	36.35	76.70	76.71	76.06	76.69	76.22	75.15
4-7	54.20	54.41	68.56	68.98	67.91	68.51	68.08	68.10
5-6	63.15	63.25	88.29	88.14	88.57	88.70	88.26	87.78
5-7	36.86	36.77	70.28	70.60	70.20	70.67	70.22	69.03
6-7	32.22	32.18	58.16	58.49	58.73	58.44	58.77	57.72

Data from "Tracker as Reference 1" and "Tracker as Reference 2" columns are collected months apart from the rest of the data. Therefore, the distances differ greatly from the rest of other data which are collected within the time-span of 3 weeks. That being said, the data from first two columns are similar between them, but different from the rest. Therefore, there can be no comparison with the rest of the data, because the setup is not the same and the distances between points might have different meaning.

Table B.2.: Distances for each run, tracker as RCS setup 1.

1st Point	2nd Point							
1	1	0.00	0.62	2.22	0.86	1.18	0.62	0.00
1	2	73.58	73.50	73.34	73.00	73.44	73.20	73.11
1	3	54.21	53.71	53.44	53.18	53.70	53.99	53.50
1	4	83.86	83.50	84.43	83.46	84.66	83.89	83.53
1	5	35.36	35.22	35.71	34.62	35.41	35.82	35.68
1	6	80.28	80.97	80.40	80.29	80.30	79.96	80.66
1	7	82.64	83.00	82.96	82.85	83.03	82.76	83.13
2	1	73.58	73.20	71.68	73.30	72.45	73.50	73.11
2	2	0.00	0.44	0.35	0.95	0.44	0.44	0.00
2	3	35.37	35.90	34.64	36.19	35.54	35.56	36.08
2	4	55.94	56.08	56.13	55.77	57.11	56.26	56.40
2	5	79.93	79.28	79.99	79.12	79.81	80.02	79.37
2	6	59.20	59.29	59.19	59.15	59.26	58.96	59.05
2	7	91.49	92.24	92.14	92.04	92.55	91.49	92.24
3	1	54.21	53.99	53.03	53.62	53.17	53.71	53.50
3	2	35.37	35.56	35.37	34.44	35.23	35.90	36.08
3	3	0.00	0.85	1.30	1.18	0.54	0.85	0.00
3	4	54.46	53.86	54.36	53.93	55.35	54.11	53.50
3	5	55.81	55.41	55.91	55.42	55.82	54.99	54.60
3	6	80.35	80.62	80.36	80.27	80.34	80.36	80.63
3	7	94.64	95.14	95.07	94.95	95.27	94.15	94.64
4	1	83.86	83.89	82.88	83.26	83.20	83.50	83.53
4	2	55.94	56.26	55.98	55.77	55.52	56.08	56.40
4	3	54.46	54.11	54.35	54.49	54.41	53.86	53.50
4	4	0.00	1.27	1.28	0.68	1.24	1.27	0.00
4	5	65.12	64.48	64.90	64.71	64.91	64.53	63.90
4	6	75.64	75.30	75.43	75.35	75.37	76.49	76.17
4	7	67.25	67.49	67.44	67.35	67.53	67.95	68.18
5	1	35.36	35.82	36.16	34.66	35.56	35.22	35.68
5	2	79.93	80.02	79.77	79.30	79.63	79.28	79.37
5	3	55.81	54.99	55.48	54.69	55.31	55.41	54.60
5	4	65.12	64.53	65.58	64.68	65.49	64.48	63.90
5	5	0.00	0.86	0.39	1.33	0.36	0.86	0.00
5	6	89.03	89.39	89.02	88.90	88.89	88.21	88.57
5	7	70.70	70.72	70.71	70.59	70.54	69.99	70.02
6	1	80.28	79.96	78.34	80.44	79.61	80.97	80.66
6	2	59.20	58.96	58.92	59.74	59.05	59.29	59.05
6	3	80.35	80.36	79.14	80.37	80.13	80.62	80.63
6	4	75.64	76.49	76.72	75.86	76.69	75.30	76.17
6	5	89.03	88.21	89.04	87.75	88.75	89.39	88.57
6	6	0.00	1.00	0.34	0.37	0.42	1.00	0.00
6	7	58.08	59.08	58.96	58.92	59.63	57.87	58.87
7	1	82.64	82.76	81.88	82.55	82.59	83.00	83.13
7	2	91.49	91.49	91.28	91.60	91.12	92.24	92.24
7	3	94.64	94.15	93.77	94.15	94.27	95.14	94.64
7	4	67.25	67.95	68.48	67.52	67.57	67.49	68.18
7	5	70.70	69.99	70.51	69.73	70.34	70.72	70.02
7	6	58.08	57.87	57.89	57.81	57.71	59.08	58.87
7	7	0.00	1.00	0.89	0.85	1.57	1.00	0.00

1.74	1.26	0.82	2.22	1.74	0.00	2.53	1.38	0.86
72.96	72.62	73.06	71.68	71.59	71.44	71.11	71.54	73.30
53.22	52.97	53.48	53.03	52.55	52.23	52.03	52.52	53.62
84.46	83.48	84.69	82.88	82.55	83.46	82.49	83.71	83.26
36.18	35.08	35.88	36.16	35.98	36.50	35.37	36.20	34.66
80.09	79.98	79.99	78.34	79.03	78.46	78.36	78.36	80.44
83.09	82.98	83.16	81.88	82.27	82.22	82.11	82.31	82.55
71.59	73.22	72.36	73.34	72.96	71.44	73.06	72.21	73.00
0.29	1.19	0.76	0.35	0.29	0.00	1.04	0.52	0.95
34.81	36.37	35.72	35.37	35.89	34.63	36.18	35.53	34.44
56.45	56.09	57.43	55.98	56.13	56.18	55.82	57.16	55.77
80.08	79.20	79.90	79.77	79.12	79.83	78.96	79.65	79.30
58.95	58.91	59.02	58.92	59.02	58.92	58.88	58.98	59.74
92.14	92.04	92.56	91.28	92.03	91.93	91.83	92.34	91.60
52.55	53.12	52.68	53.44	53.22	52.23	52.87	52.40	53.18
35.89	34.97	35.75	34.64	34.81	34.63	33.71	34.49	36.19
1.56	0.60	0.56	1.30	1.56	0.00	1.60	1.10	1.18
54.01	53.58	54.99	54.35	53.78	54.29	53.84	55.26	54.49
55.10	54.62	55.01	55.48	55.08	55.59	55.07	55.49	54.69
80.36	80.28	80.35	79.14	79.42	79.15	79.07	79.14	80.37
94.57	94.45	94.76	93.77	94.27	94.20	94.08	94.40	94.15
82.55	82.90	82.84	84.43	84.46	83.46	83.83	83.76	83.46
56.13	55.89	55.66	56.13	56.45	56.18	55.95	55.71	55.77
53.78	53.89	53.81	54.36	54.01	54.29	54.41	54.32	53.93
1.05	0.70	1.51	1.28	1.05	0.00	1.15	1.31	0.68
64.31	64.13	64.33	65.58	64.94	65.35	65.18	65.37	64.68
76.29	76.21	76.23	76.72	76.38	76.51	76.43	76.46	75.86
68.13	68.04	68.21	68.48	68.72	68.67	68.58	68.76	67.52
35.98	34.53	35.41	35.71	36.18	36.50	35.02	35.92	34.62
79.12	78.66	78.98	79.99	80.08	79.83	79.36	79.69	79.12
55.08	54.30	54.92	55.91	55.10	55.59	54.80	55.42	55.42
64.94	64.04	64.86	64.90	64.31	65.35	64.46	65.26	64.71
0.86	0.73	0.58	0.39	0.86	0.00	1.45	0.36	1.33
88.19	88.08	88.06	89.04	89.40	89.03	88.91	88.90	87.75
70.00	69.89	69.84	70.51	70.52	70.51	70.40	70.34	69.73
79.03	81.13	80.30	80.40	80.09	78.46	80.56	79.73	80.29
59.02	59.84	59.13	59.19	58.95	58.92	59.73	59.04	59.15
79.42	80.65	80.41	80.36	80.36	79.15	80.38	80.14	80.27
76.38	75.54	76.35	75.43	76.29	76.51	75.66	76.47	75.35
89.40	88.11	89.11	89.02	88.19	89.03	87.74	88.74	88.90
0.70	0.77	0.78	0.34	0.70	0.00	0.12	0.20	0.37
58.75	58.71	59.41	57.89	58.89	58.78	58.73	59.44	57.81
82.27	82.92	82.96	82.96	83.09	82.22	82.87	82.91	82.85
92.03	92.34	91.87	92.14	92.14	91.93	92.24	91.77	92.04
94.27	94.64	94.77	95.07	94.57	94.20	94.57	94.70	94.95
68.72	67.76	67.79	67.44	68.13	68.67	67.71	67.74	67.35
70.52	69.76	70.36	70.71	70.00	70.51	69.75	70.35	70.59
58.89	58.81	58.71	58.96	58.75	58.78	58.69	58.60	58.92
0.12	0.20	0.59	0.89	0.12	0.00	0.12	0.69	0.85

1.26	2.53	0.00	1.28	1.18	0.82	1.38	1.28	0.00
73.22	73.06	72.70	73.15	72.45	72.36	72.21	71.86	72.30
53.12	52.87	52.59	53.11	53.17	52.68	52.40	52.16	52.66
82.90	83.83	82.86	84.06	83.20	82.84	83.76	82.79	84.01
34.53	35.02	33.93	34.72	35.56	35.41	35.92	34.81	35.62
81.13	80.56	80.46	80.46	79.61	80.30	79.73	79.63	79.64
82.92	82.87	82.76	82.94	82.59	82.96	82.91	82.80	82.99
72.62	71.11	72.70	71.86	73.44	73.06	71.54	73.15	72.30
1.19	1.04	0.00	0.99	0.44	0.76	0.52	0.99	0.00
34.97	33.71	35.26	34.61	35.23	35.75	34.49	36.04	35.40
55.89	55.95	55.59	56.93	55.52	55.66	55.71	55.35	56.69
78.66	79.36	78.50	79.19	79.63	78.98	79.69	78.82	79.51
59.84	59.73	59.69	59.80	59.05	59.13	59.04	59.00	59.10
92.34	92.24	92.14	92.65	91.12	91.87	91.77	91.67	92.18
52.97	52.03	52.59	52.16	53.70	53.48	52.52	53.11	52.66
36.37	36.18	35.26	36.04	35.54	35.72	35.53	34.61	35.40
0.60	1.60	0.00	0.73	0.54	0.56	1.10	0.73	0.00
53.89	54.41	53.96	55.38	54.41	53.81	54.32	53.88	55.30
54.30	54.80	54.31	54.71	55.31	54.92	55.42	54.92	55.33
80.65	80.38	80.30	80.36	80.13	80.41	80.14	80.06	80.13
94.64	94.57	94.45	94.76	94.27	94.77	94.70	94.58	94.89
83.48	82.49	82.86	82.79	84.66	84.69	83.71	84.06	84.01
56.09	55.82	55.59	55.35	57.11	57.43	57.16	56.93	56.69
53.58	53.84	53.96	53.88	55.35	54.99	55.26	55.38	55.30
0.70	1.15	0.00	1.48	1.24	1.51	1.31	1.48	0.00
64.04	64.46	64.27	64.47	65.49	64.86	65.26	65.09	65.28
75.54	75.66	75.58	75.60	76.69	76.35	76.47	76.40	76.42
67.76	67.71	67.62	67.80	67.57	67.79	67.74	67.65	67.82
35.08	35.37	33.93	34.81	35.41	35.88	36.20	34.72	35.62
79.20	78.96	78.50	78.82	79.81	79.90	79.65	79.19	79.51
54.62	55.07	54.31	54.92	55.82	55.01	55.49	54.71	55.33
64.13	65.18	64.27	65.09	64.91	64.33	65.37	64.47	65.28
0.73	1.45	0.00	1.09	0.36	0.58	0.36	1.09	0.00
88.11	87.74	87.62	87.61	88.75	89.11	88.74	88.62	88.61
69.76	69.75	69.63	69.59	70.34	70.36	70.35	70.23	70.18
79.98	78.36	80.46	79.63	80.30	79.99	78.36	80.46	79.64
58.91	58.88	59.69	59.00	59.26	59.02	58.98	59.80	59.10
80.28	79.07	80.30	80.06	80.34	80.35	79.14	80.36	80.13
76.21	76.43	75.58	76.40	75.37	76.23	76.46	75.60	76.42
88.08	88.91	87.62	88.62	88.89	88.06	88.90	87.61	88.61
0.77	0.12	0.00	0.13	0.42	0.78	0.20	0.13	0.00
58.81	58.69	58.65	59.35	57.71	58.71	58.60	58.55	59.26
82.98	82.11	82.76	82.80	83.03	83.16	82.31	82.94	82.99
92.04	91.83	92.14	91.67	92.55	92.56	92.34	92.65	92.18
94.45	94.08	94.45	94.58	95.27	94.76	94.40	94.76	94.89
68.04	68.58	67.62	67.65	67.53	68.21	68.76	67.80	67.82
69.89	70.40	69.63	70.23	70.54	69.84	70.34	69.59	70.18
58.71	58.73	58.65	58.55	59.63	59.41	59.44	59.35	59.26
0.20	0.12	0.00	0.72	1.57	0.59	0.69	0.72	0.00

B.1.2. Cubic Phantom Data

Table B.3.: Distances in millimeter between eight landmarks of the cubic phantom. First three rows with the tracker as reference coordinate system, fourth row with the 6-DOF sensor as reference system, last row shows distances from the virtual model.

Distances	Tracker as Reference 1	Tracker as Reference 2	Tracker as Reference 3	6-DOF as Reference	VM Fusion 360
1-2	24.89	25.73	25.01	24.69	25.00
1-3	35.25	36.58	34.81	35.21	35.36
1-4	24.78	24.98	23.78	24.99	25.00
1-5	35.94	36.10	35.94	35.92	35.36
1-6	61.78	61.90	62.04	61.58	61.24
1-7	75.77	76.12	74.72	75.05	75.00
1-8	56.54	57.02	55.81	56.21	55.90
2-3	25.20	25.98	24.43	24.84	25.00
2-4	35.14	35.95	34.23	34.87	35.36
2-5	43.84	44.09	43.69	43.49	43.30
2-6	44.11	43.66	44.23	44.04	43.30
2-7	62.39	62.12	61.07	61.33	61.24
2-8	56.54	62.40	61.01	61.03	61.24
3-4	24.67	25.91	24.42	24.59	25.00
3-5	35.17	35.33	35.20	34.96	35.36
3-6	35.96	35.10	35.90	35.78	35.36
3-7	44.33	43.44	43.56	43.66	43.30
3-8	43.90	43.61	43.27	43.08	43.30
4-5	24.82	25.22	25.12	24.67	25.00
4-6	56.14	56.57	55.96	55.78	55.90
4-7	61.82	62.58	61.09	61.21	61.24
4-8	36.15	36.57	36.11	35.66	35.36
5-6	50.27	49.86	50.19	49.71	50.00
5-7	55.77	55.75	55.00	55.23	55.90
5-8	24.50	24.95	24.19	24.14	25.00
6-7	25.31	24.98	23.85	24.08	25.00
6-8	56.36	55.99	55.39	54.93	55.90
7-8	50.20	50.10	49.21	49.33	50.00

C. Protocol for experiment 3

Tracking Accuracy assessment protocol under the influence of ICE catheter probe using 2*5DOF and 1*6DOF electromagnetic sensors

1. Theory Background

This document comprises the step-by-step procedure for the tracking accuracy assessment of the AURORA V3 tracking system using electromagnetic sensors attached to the ICE catheter transducer. The experiment involves the tracking system, ICE catheter, a baseplate with 36 equally distanced holes in a rectangular pattern and 16 holes in a circle pattern, 2*5DOF EM sensors, and 1*6DOF EM sensor. This experiment aims to find the influence of the proximity EM sensors on the tracking accuracy. It is not in the scope of this experiment to define the region of the measurement volume with the best accuracy neither the error distribution.

The accuracy is comprised by **trueness** and **precision**. Trueness relates to systematic error, while precision to random error. Both errors contribute to the system's accuracy. With the increasing number of samples, it is possible to reduce the contribution of random error (variation of the pose when the sensor is held unmoved). However, trueness and precision are not good representatives of the accuracy for the purpose of our experiment. They comprise accuracy over the entire volume of a tracking system ([view article online]) [1]. The accuracy measurements will be conducted according *Hummel et al.* [1][2].

2. Experiment

The experiment will be carried on only with the probe on. Relative positional/orientational errors are found by the difference between the known distances/rotations between the 3D printed model locations and the mean observed positions/rotations. The Influence of the sensor was tested on the previous experiments. Metrics to be evaluated: mean, standard deviation, minimum, maximum, RMS error of the pose ate each location.

2.1 Materials used

Base plate & sensor mount

3D printed base plate (A) with a rectangle pattern of 6x6 holes. Distance between holes is 20 mm. Circular pattern with radius 20 mm. The plate is marked with x and y axis for better orientation. In B) it is shown the sensor mount. The pins fit in the holes. The angular distance between holes is 22.5 degree. The ICE catheter is fixed where the red arrow points. It is also possible to attach a 6DOF sensor together with the ICE catheter.

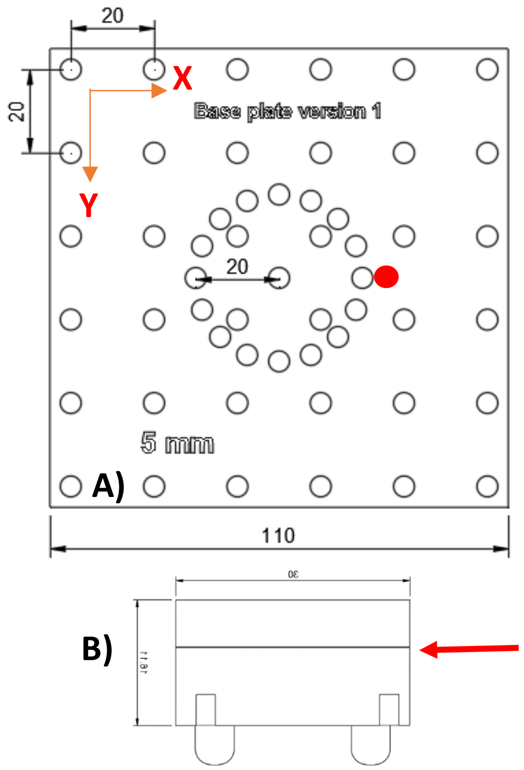

Mounting Frame

C)

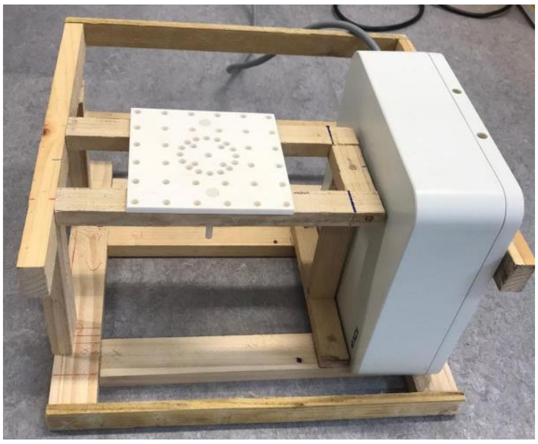

D)

The frame is constructed by wooden structures, to avoid any distortion in the magnetic field. The base plate is fixed with plastic screws on the top of the frame. The Field generator can be positioned and fixed underneath the baseplate and on the sides, according to three rotation axes of the coordinate system of the field generator.

ICE catheter

2*5DOF sensors

E)

At the tip of the catheter are attached rigidly two 5DOF sensors. The catheter is mounted in the sensor mount B).

2.2 Procedure of the Experiment

The axes of the field generator will be marked accordingly on the surface of the field generator. Ten seconds of raw data will be recorded for each position and orientation. The data for the positioning will be recorded only for one position of the field generator. The data for the orientation will be recorded for all three positions of the field generator (one for each axis).

2.2.1. Position of the Field Generator: under the base plate, Z-axis

1. Fix the ICE catheter rigidity in the sensor mount
2. Move along x-axis on the base plate, repeat the process for each row
3. Move along the circular pattern on the base plate, starting from the red spot, clockwise
4. Record 10s of data for each location

2.2.2. Position of the Field Generator: on the side of the base plate, X-axis

5. Move along the circular pattern on the base plate, starting from the red spot, clockwise
6. Record 10s of data for each location

2.2.2. Position of the Field Generator: on the side of the base plate, X-axis

7. Move along the circular pattern on the base plate, starting from the red spot, clockwise
8. Record 10s of data for each location

3. Computations

3.1 Jitter error

The jitter error will be evaluated by statistical analysis of 10 sec continuous raw position and orientation data. The aim is to determine the variation of the error within the scanning volume, which is similar in scale to the heart volume. The position and orientation data will be averaged over 10s stream, to reduce random error. The Jitter error will be calculated according to Eq. 1.

$$E_{RMS} = \sqrt{\frac{\sum_{i=1}^{N}(p_{r_i} - p_{o_i})^2}{N}} \quad (1)$$

Where:

p_{r_i} : $the\ reference\ position\ from\ the\ model$
p_{o_i} : $the\ observerd\ position$
N : $number\ of\ samples\ for\ 10\ second\ stream\ of\ data$

3.2 Position error based on distances

Error (mm)			
Mean jitter	SD	Minimum	Maximum
-	-	-	-

Mean: Mean of the Jitter error for each position
SD: Standard Deviation
Minimum: Minimum value of deviation from the reference position
Maximum: Maximum value of deviation from the reference position

3.2 Orientational error based on angular differences

	Error (mm)			
	Mean jitter	SD	Minimum	Maximum
x-axis				
y-axis				
z-axis				

Remarks – update (21.09.2020)

For each point 10 seconds of data will be recorded with Tracker's application, approximately 400 entries of coordinates. Distances will be calculated between points, on the x-axis direction and y-axis direction. That brings us to 2*5*6 distances.

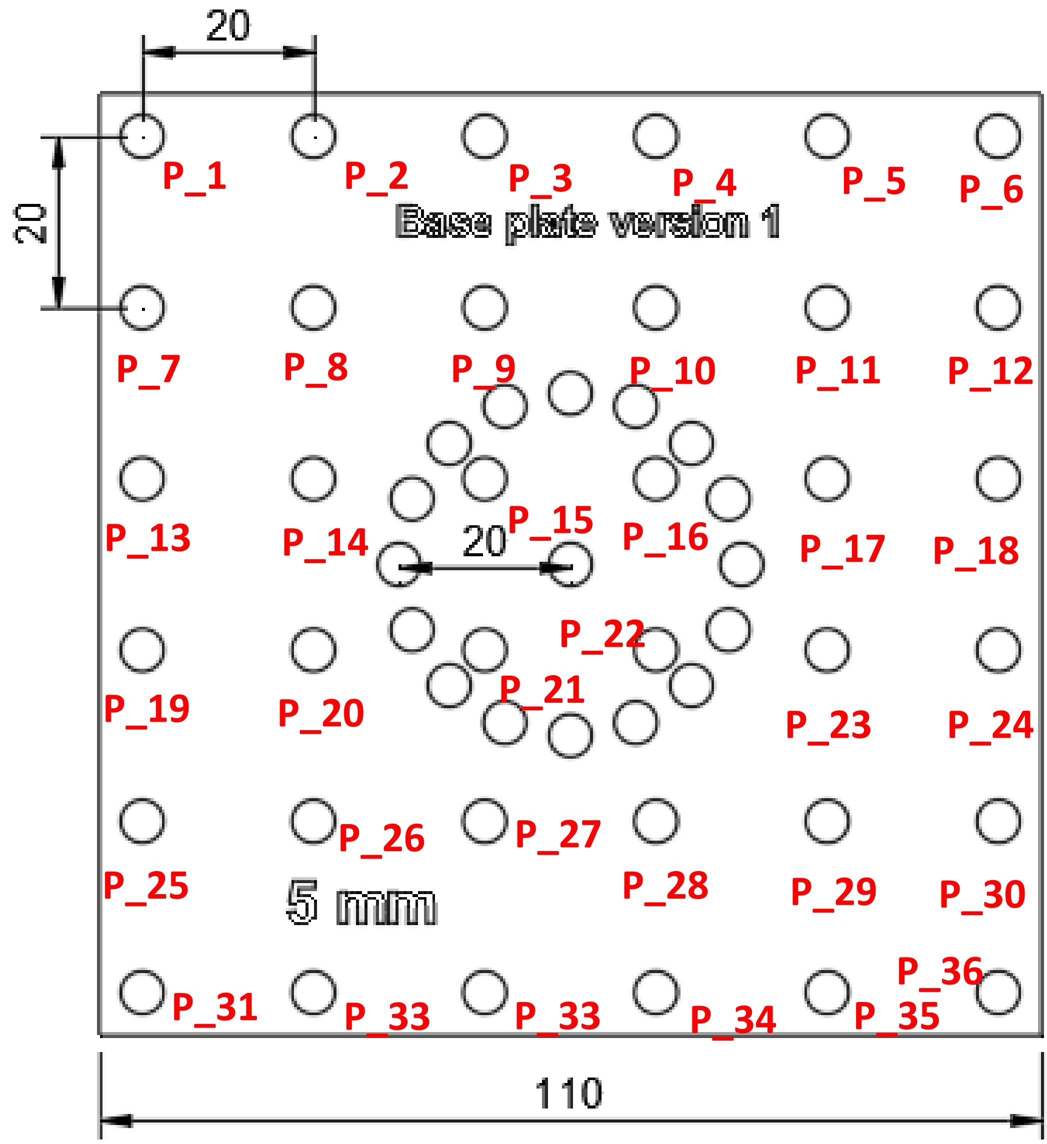

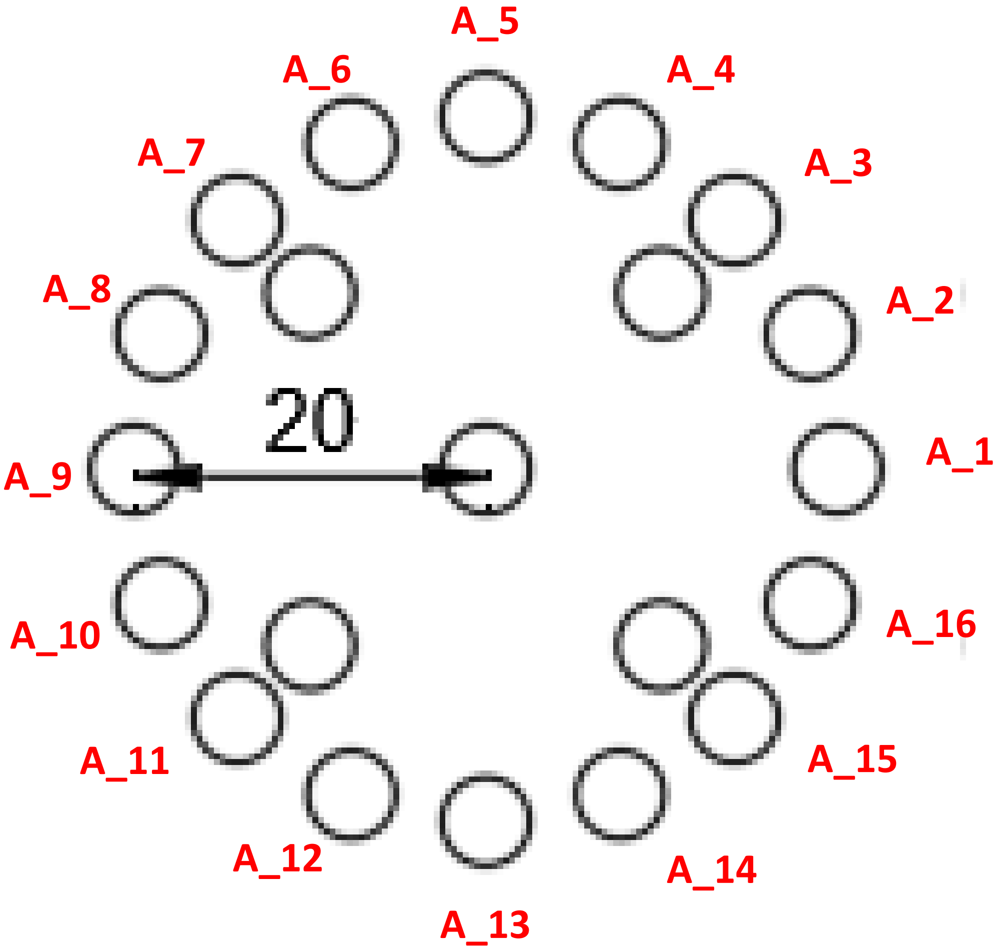

The recorded data according positional accuracy will be inserted in **Table 1**, and the recorded data for the angular accuracy will be inserted in **Table 2**.

Table 1: Computation for positional accuracy

Distances	Transducer ON	Transducer OFF
P_1_2		
P_2_3		
P_3_4		
P_4_5		
P_5_6		
P_7_8		
P_8_9		
P_9_10		
P_10_11		
P_11_12		
P_13_14		
P_14_15		
P_15_16		
P_16_17		
P_17_18		
P_19_20		
P_20_21		
P_21_22		
P_22_23		
P_23_24		
P_25_26		
P_26_27		
P_27_28		
P_28_29		
P_29_30		
P_31_32		
P_32_33		
P_33_34		
P_34_35		
P_35_36		
P_1_7		
P_7_13		
P_13_19		
P_19_25		
P_25_31		
P_2_8		
P_8_14		
P_14_20		
P_20_26		
P_26_32		
P_3_9		
P_9_15		

P_15_21		
P_21_27		
P_27_33		
P_4_10		
P_10_16		
P_16_22		
P_22_28		
P_28_34		
P_5_11		
P_11_17		
P_17_23		
P_23_29		
P_29_33		
P_6_12		
P_12_18		
P_18_24		
P_24_30		
P_30_36		

Table 2: Computation for angular accuracy

Angle	Transducer ON			Transducer OFF		
	x	y	z	x	y	z
A_1_2						
A_2_3						
A_3_4						
A_4_5						
A_5_6						
A_6_7						
A_7_8						
A_8_9						
A_9_10						
A_10_11						
A_11_12						
A_12_13						
A_12_14						
A_14_15						
A_15_16						
A_16_1						

References

[1] D D Frantz et al 2003 Phys. Med. Biol. 48 2241.

[2] Johann B Hummel, Michael R. Bax, Michael L. Figl, Yan Kang, Calvin Maurer, Wolfgang W. Birkfellner, Helmar Bergmann, and Ramin Shahidi. Design and application of an assessment protocol for electromagnetic tracking systems. Medical Physics, 32(7Part1):2371–2379, jun 2005.

[3] J Hummel, M Figl, W Birkfellner, M R Bax, R Shahidi, C R Maurer, and H Bergmann.Evaluation of a new electromagnetic tracking system using a standardized assessmentprotocol.Physics in Medicine and Biology, 51(10):N205–N210, apr 2006.